McMaster University

FINAL REPORT

(1984-86)

A STUDY OF THE EFFECT OF SURFACE MODIFICATION ON ALLOY OXIDATION BEHAVIOR

Submitted by:

Professors W.W. Smeltzer and D.A. Thompson
Institute for Materials Research
McMaster University
Hamilton, Ontario, L8S 4M1

Submitted to:

Scientific Authority:
Supply and Services Canada
c/o H. Hindam

D.S.S. File Number: 06ST.23440-3-9108

Contract Serial Number: OST83-00152

199 pp

December 31, 1986

W.W. Smeltzer

MICROMEDIA

A STUDY OF THE EFFECT OF SURFACE MODIFICATION ON

ALLOY OXIDATION BEHAVIOR

SUMMARY

This final report contains two major sections and an appendix encompassing the following research:

I. Ion-Beam Modification of Fe-Al Alloys for Oxidation Resistance.

II. The Effect of Ion Implantation of Aluminum upon Oxidation of Fe-6 a% Al Alloy at 1173K.

Appendix 1. Oxidation of Fe-Al Alloys in Oxygen at 1273 and 1373K.

Section I presents initially the purpose, theory and literature review for this experimental program on ion-beam modification of Fe-Al alloys for oxidation resistance. This is followed by presenting the experimental and analytical techniques, experimental results, discussion and conclusion. In this part of the work: Fe and Fe-2,3,4,5 and 10 a% Al alloys were implanted with doses of $7x10^{15}$ to $7x10^{17}$ Al^+ ions/cm^2 at 100 kV; 100nm layers of Al evaporated onto Fe samples were ion-beam mixed with $7x10^{16}$ Al^+ ions/cm^2 at 100 kV and, finally, these specimens were oxidized at 1173K in oxygen at 26.7kPa. All ion-beam modified specimens oxidized at 873K exhibited lower weight-gain kinetics than controls, with the ion-beam mixed specimen much lower possibly due to formation of γ-Al_2O_3. At 1173K, oxidation of pure Fe was not changed by ion-beam implantation or mixing of Al. Oxidation kinetics of Fe-2,3 and 4 a% Al alloy were marginally improved although no change could be seen in the oxide morphology, which consisted of spinel precipitates underneath a continuous layer of hematite and magnetite. On the Fe-5 a% Al alloy, ion beam implantation produced heavily noduled duplex hematite/alumina films with irreproducible but

generally low reaction kinetics. No improvement was detected for the Fe-10 a% Al alloy, due to the irreproducibility and very slow growth rates of noduled films formed on both implanted and unimplanted samples.

Section II described a detailed investigation on the effect of ion implantation of Al upon oxidation of an Fe-6 a% Al alloy at 1173K. This work was carried out as it appeared possible that Al ion implantation could possibly lead to complete formation of a protective alumina film on an alloy of this minimum Al content. Fe-6 a% Al alloy samples were implanted with doses of $5x10^{16}$ to $2x10^{17}$ Al^+ ions/cm^2 at 100kV, and subsequently oxidized in oxygen at 27kPa. No effect on oxidation was observed if the implant dose was less than $1x10^{17}Al^+$ ions/cm^2. Implanting of doses of $1x10^{17}Al^+$ ions/cm^2 or higher, effected a change in the oxide morphology from a duplex hematite/alumina scale to an alumina-enriched film with a dispersion of hematite nodules. Oxygen uptake by the high-dose samples was due principally to nodule formation and weight gains after 45h were lower by 50 to 70% when compared to the unimplanted material. The presence of these nodules acted as an upper limit on the benefits provided by implantation of aluminum. Nodule formation was shown to be characteristic of the oxidation properties of the alloy material, not an extraneous feature introduced by the implantation process itself. Surface preparation prior to implantation held little effect on oxidation: high-dose electropolished samples behaved similarly to mechanically polished samples when implanted to comparable doses.

In Appendix 1, a summary is presented of investigations carried out on the oxidation properties of seven Fe-Al alloys containing from 5 to 15 a% Al in 1 atm of oxygen at 1273 and 1373K. The oxidation kinetics can be represented by two parabolic reaction rate constants for early and long exposure periods, the rate constant at long exposures being at least 10^3

smaller than that at early stage exposures. The scale morphologies at these two higher temperatures were similar to those at 973K, oxidation resistance increasing as the morphologies changed from precipitates/ magnetite/hematite; alumina/magnetite/hematite; alumina/hematite/nodules; alumina/hematite nodules, to alumina films with increasing alloy aluminum content. Alloys containing 12 to 16 a% Al only formed the most highly protective alumina films, the alloy composition apparently being more significant than temperature in the range 1173-1373K.

RESEARCH PLAN

The plan of this work was to investigate the effectiveness of increasing the oxidation resistance of Fe-Al alloys of low Al contents at the high temperature of 1173K (the uppermost limit for application of stainless steels) by increasing the Al content in the near surface region of the alloy to support alumina film growth by Al^+ ion-beam implantation and mixing techniques. Al^+ ion beam implantation did exert a beneficial role but its effect was not sufficient to enable the development of a ductile oxidation-resistant material.

The first section of the report is essentially the M. Eng. thesis (1986) carried out by Roderick Beauprie. Doris Stevanovic, research engineer, carried out almost all the RBS measurements and ion-beam mixing experiments; Brett McClelland carried out the Al implantations. Ross Underhill, research associate and Frank Szostak, technician, provided interpretation of SAM results.

The detailed investigation described in Section II on the effect of ion implantation of aluminum upon oxidation of Fe-6 a% Al alloy at 1173K was carried out by Peter Smith, postdoctoral fellow, Roderick Beauprie and Doris Stevanovic.

Oxidation investigation on Fe-Al alloys (3 to 16 a%) at the high temperatures of 1273K and 1373K and summarized in Appendix 1 were carried out by Hafiz Ahmed and Prakash Patnaik as part of their postdoctoral research fellowship studies.

ETUDE DE L'EFFET DE LA MODIFICATION DE LA SURFACE DES ALLIAGES SUR L'OXYDATION

SOMMAIRE

Ce rapport final contient deux sections majeures et un appendice traîtant le projet de recherche suivant:

I. Modification des alliages Fe-Al par bombardement ionique pour améliorer leur résistance à l'oxydation

II. Effet de l'implantation de $l'Al^+$ sur l'oxydation du Fe-6a% Al à 1173 K.

Appendice 1. Oxydation des alliages Fe-Al dans l'oxygène à 1273 et 1373 K.

La section I présente le but, la théorie et une revue de la littérature. Les techniques analytiques, les résultats expérimentaux, la discussion de ces résultats et la conclusion sont ensuite présentés. Dans cette partie du travail, Fe, Fe-2, 3, 4, 5 et 10a% Al ont été implantés avec des doses de 7×10^{15} à 7×10^{17} Al^+/cm^2 à 100 kV; des couches d'Al de 100 nm d'épaisseur déposées par évaporation sur des échantillons de Fe sont bombardés avec un faisceau d'Al^+ à 7×10^{16} ions/cm^2 et 100 kV et finalement ces échantillons ont été oxydés à 1173 K dans l'oxygène à 26.7 kPa. Le gain en poids de tous les échantillons modifiés par les traîtements ioniques et qui ont été oxydés à 873 K est inférieur à celui des échantillons non-traîtés du probablement à la formation de γ-Al_2O_3. A 1173 K, l'oxydation de Fe n'a pas été altérée par ces traîtements. L'oxydation du Fe-2, 3 et 4a% Al a été légèrement améliorée bien que la constitution de l'écaille (précipités

de $FeAl_2O_4$ sous une couche de Fe_2O_3/Fe_3O_4) demeura la même. L'implantation des ions d'Al^+ dans Fe-5a% Al produit des films de Fe_2O_3/Al_2O_3 contenant des nodules et elle est accompagnée d'une cinétique irreproductible bien que le gain de poids est généralement plus faible. On n'a pas noté d'amélioration dans le cas du Fe-10a% Al.

La Section II présente une étude détaillée de l'effet de l'implantation de l'Al sur l'oxydation du Fe-6Al à 1173 K. Cette étude a été entreprise parce qu'il paraissait que l'implantation de l'Al dans cet alliage pourrait conduire à la formation d'une couche protectrice d'Al_2O_3. L'alliage a été implanté avec des doses de 5×10^{16} à 2×10^{17} Al^+/cm^2. L'implantation de plus de 10^{17} Al^+/cm^2 modifia la morphologie du film double (Fe_2O_3/Al_2O_3) à un film riche en Al_2O_3 contenant des nodules de Fe_2O_3. Après 45h, le gain de poids était inférieur de 50% à 70% à celui des échantillons non-implantés. La formation des nodules est une propriété intrinsèque de l'alliage qui n'est pas causée par le traitement ionique. Elle ne dépend pas de la préparation de la surface (abrasion mécanique ou electropolissage).

Dans l'Appendice 1, on présente un résumé de l'étude sur les propriétés d'oxydation des alliages Fe-Al contenant de 5 à 15a% Al dans l'oxygène à 1273 et 1373 K.

SECTION I

ION BEAM MODIFICATION OF Fe-Al ALLOYS FOR OXIDATION RESISTANCE

TABLE OF CONTENTS

			Page
1.	INTRODUCTION		
2.	THEORY		
	2.1	Oxidation criteria for alloy evaluation.	2
	2.2	Diffusion and thermodynamic data.	4
	2.3	Diffusion paths.	13
	2.4	Theoretical predictions of Fe-Al oxidation.	16
	2.5	Previous studies of Fe-Al oxidation.	18
	2.6	Principles of Ion Implantation.	25
	2.7	Ion-Beam mixing theory.	29
	2.8	Previous studies of Ion-Beam mixing of Fe-Al.	34
	2.9	Previous studies of oxidation of implanted Fe.	41
3.	EXPERIMENTAL		
	3.1	Sample preparation.	46
	3.2	Implantation.	50
	3.3	Thin film preparation and mixing.	55
	3.4	Oxidation.	57
4.	ANALYSIS		
	4.1	Energy-dispersive X-Ray analysis.	63
	4.2	Rutherford Back-scattering (RBS).	63
	4.3	Auger electron spectroscopy (AES).	64
	4.4	Optical microscopy.	65
	4.5	Electron microscopy.	65
	4.6	X-Ray diffraction (XRD).	66
5.	RESULTS AND DISCUSSION		
	5.1	Ion beam mixing experiments.	67
	5.2	Oxidation experiments.	71
6.	CONCLUSIONS AND SUGGESTIONS FOR FURTHER WORK		

LIST OF FIGURES

Figure 1.	Fe and O diffusion in Fe and Fe oxides.
Figure 2.	Chemical diffusion coefficients in Fe-Al alloys.
Figure 3.	Fe-Al phase diagram.
Figure 4.	Al activity in Fe-Al alloys.
Figure 5.	Semi-log plot of Al activity in Fe-Al alloys.
Figure 6.	Fe-O phase diagram.
Figure 7.	Phase relations in the system Fe-Al-O at 1273 K.
Figure 8.	Fe-Al-O equilibrium oxygen pressures at 1173 K.
Figure 9.	Example of diffusion path.
Figure 10.	Diffusion path representation of supersaturation.
Figure 11.	Diffusion path representation of internal oxidation.
Figure 12.	Model for oxidation of Fe-3.8 a% Al alloy at 1073 K.
Figure 13.	Diffusion paths at 1173 K.
Figure 14.	Model for nodule formation at 1073 K.
Figure 15.	Evolution of depth profile of 100 kV Al implanted into pure iron with three different doses.
Figure 16.	Schematic of the sputtering and atomic mixing processes using energetic ion beams.
Figure 17.	Schematic of the implantation and damage processes using energetic ion beams.
Figure 18.	Schematic of a displacement spike.
Figure 19.	Speed of mixing for two Sb layers in Al.
Figure 20.	Speed of mixing in Al and Al_2O_3 at two different temperatures.
Figure 21.	Mixing of a bilayer of final composition Fe-40a% Al.

LIST OF FIGURES (continued)

Figure 22.	Mixing of a multilayer for a final composition Fe-58a% Al.
Figure 23.	RBS spectra before and after 1 x 10^{16} Xe/cm^2 at 77 K.
Figure 24.	RBS spectra for various doses of 550 kV Xe at 298 K.
Figure 25.	RBS spectra for various irradiations of mixed ion pulsed beam.
Figure 26.	RBS spectra for two pulsed beams of various composition.
Figure 27.	Gravimetric curves (parabolic plot) for oxidation at 810 K of iron specimens implanted at different doses.
Figure 28.	Gravimetric curves (normal plot) for oxidation at different temperatures of iron specimens implanted with 1 x 10^{17} Al/cm^2.
Figure 29.	Schematic evolution of the oxidized layer during oxidation at 810 K.
Figure 30.	The oxidation of various steels implanted with Al at several different doses.
Figure 31.	The oxidation of a Fe-14.5%Cr-8.25%Al steel at 1373 K.
Figure 32.	(a) S.E.M. micrograph of Fe-5a% Al sample (b) EDAX results from scan of same sample.
Figure 33.	Whickham engineering ion implantation accelerator.
Figure 34.	SAM profile after implantation of 7 x 10^{17} Al/cm^2, converted to a%.
Figure 35.	Hydrogen reduction chamber.
Figure 36.	SAM profile of 100 nm of Al on Fe, surface prepared by six periods of 300 s and five periods of 600 s of hydrogen reduction.
Figure 37.	SAM profile of 100 nm of Al on Fe, surface prepared by three periods of 900 s of hydrogen reduction at 773 K.
Figure 38.	SAM profile of 100 nm of Al on Fe, surface prepared by 3 periods of 900 s at 823 K.
Figure 39.	SAM profile of sample of Figure 38 after mixing.
Figure 40.	SAM profile of sample of Figure 38, after opposite side has been reduced.

LIST OF FIGURES (continued)

Figure 41. Oxidation apparatus.

Figure 42. Configurations of evaporated films for ion-beam mixing experiments.

Figure 43. Typical RBS spectra.

Figure 44. SAM profile of unmixed evaporated films.

Figure 45. SAM profile of mixed evaporated films.

Figure 46. Weight gain of samples oxidized at 873 K, 13.4 kPa.

Figure 47. Weight gain of samples oxidized at 873 K, 13.4 kPa.

Figure 48. Metallographic cross-section of pure iron sample with mixed 100 nm Al film, oxidized at 873 K, 13.4 kPa.

Figure 49. Metallographic cross-section of pure iron sample, implanted, oxidized at 873 K, 13.4 kPa.

Figure 50. Weight gain kinetics for pure iron samples oxidized at 1173 K and 26.7 kPa.

Figure 51. Weight-gain kinetics for pure iron samples oxidized at 1173 K and 26.7 kPa.

Figure 52. Metallographic cross-section of scale from Fe-2a% Al alloy implanted with $1 \times 10^{17}/cm^2$ after 8.65×10^4 s at 1173 K and 101.3 kPa.

Figure 53. Metallographic cross-section of Fe-2a% Al alloy, unimplanted.

Figure 54. Metallographic cross section of Fe-2a% Al alloy with $1 \times 10^{17}/cm^2$ after 2.5×10^4 s at 1173 K and 26.7 kPa.

Figure 55. Weight gain kinetics for Fe-2a% Al samples oxidized at 1173 K and 26.7 kPa.

Figure 56. Weight-gain kinetics for Fe-2a% Al samples oxidized at 1173 K and 26.7 kPa.

Figure 57. Metallographic cross-section of Fe-3.1a% Al alloy, unimplanted.

Figure 58. S.E.M. view of Fe-3.1a% Al alloy implanted.

LIST OF FIGURES (continued)

Figure 59. Weight-gain kinetics of Fe-3.1a% Al samples oxidized at 1173 K and 26.7 kPa.

Figure 60. Weight-gain kinetics of Fe-3.1a% Al samples oxidized at 1173 K and 26.7 kPa.

Figure 61. Metallographic cross-section of unimplanted Fe-4.1a% Al sample oxidized at 1173K and 26.7 kPa.

Figure 62. Metallographic cross-section of unimplanted Fe-4.1a% Al sample oxidized at 1173K and 101 kPa.

Figure 63. Metallographic cross-section of Fe-4.1a% Al sample, implanted.

Figure 64. Metallographic cross-section of Fe-4.1a% Al sample, implanted.

Figure 65. S.E.M. view of internal precipitates after etching.

Figure 66. S.E.M. image of tips of internal precipitates of Figure 65.

Figure 67. Weight-gain kinetics of Fe-4.1a% Al samples oxidized at 1173 K and 26.7 kPa.

Figure 68. Weight-gain kinetics of Fe-4.1a% Al samples oxidized at 1173 K and 26.7 kPa.

Figure 69. Metallographic cross-section of Fe-5a% Al sample, unimplanted.

Figure 70. S.E.M. image of nodule on the surface of Fe-5a% Al alloy.

Figure 71. S.E.M. image of nodule distribution of Fe-5a% Al sample.

Figure 72. S.E.M. image of scale-nodule relationship on the same sample as Figure 71.

Figure 73. Weight-gain kinetics of Fe-5a% Al samples oxidized at 1173 K and 26.7 kPa.

Figure 74. Weight-gain kinetics for Fe-5a% Al samples oxidized at 1173 K and 26.7 kPa.

Figure 75. Long-term weight-gain kinetics for Fe-5a% Al samples oxidized at 1173 K and 26.7 kPa.

Figure 76. S.E.M. image of scale/nodule relationship on Fe-9.8a% Al sample implanted.

LIST OF FIGURES (continued)

Figure 77. S.E.M. image of the same sample as Figure 77, scale morphology.

Figure 78. Weight-gain kinetics for Fe-9.8a% Al samples oxidized at 1173 K and 26.7 kPa.

Figure 79. Summary of oxidation results.

Figure 80. Schematic illustration of proposed model for oxidation following Al implantation.

NOMENCLATURE

A	area of oxidation specimen
a_i	activity of species i
a	scattering length
a_o	Bohr length
C	mixed volume fraction
$\overline{D}$	chemical diffusion coefficient
$D_{Al}^{\alpha_{Fe}}$	diffusion constant for Al in Fe
$D_O^{\alpha_{Fe}}$	diffusion constant for O in Fe
e	charge on electron
E	energy of a colliding particle
$F(x)$	distribution of ions in solid
ΔG_F	Gibb's free energy of formation
ΔG_r	Gibb's free energy of reaction
h	Planck's constant
K_P	parabolic rate constant
M	molar mass
M_i	mass of a body in a collision
N_{IE}	Al content for transition to external oxidation
N_{MIN}	minimum Al content for Al_2O_3 formation
N_s	mole fraction of oxygen in alloy
N	atomic number density
$N(E)$	number of auger electrons at energy
p	impact parameter
r	separation of ion and target atom
R_p	mean ion range = $\langle x \rangle$
S	sputtering yield
t	time
t_{12}	transition time
T	temperature
T	transferred energy

NOMENCLATURE (continued)

T_{max}	maximum transferred energy
u	reciprocal seperation
u_o	reciprocal minimum seperation
u_n	nth moment of particle distribution
ΔW	weight gain during oxidation
x	penetration into solid
v	ion velocity
v	Bohr velocity
V(r)	potential between ion and target atom
$\overline{V}$	molar volume of substance
Z	valence or atomic number
Φ_{crit}	critical volume fraction
Φ_c	critical fluence for complete mixing
v	stoichiometric constant
$\chi(r/a)$	Thomas-Fermi screening function
θ_{com}	angle of deflection in centre of mass system
σ_n	cross section for nuclear collision
σ^2	variance of marker signal
Ω	resistivity of evaporated film
λ	wavelength

CHAPTER 1

INTRODUCTION

The most commercially-important family of oxidation-resistant alloys is the Fe-Cr family, i.e., the "stainless" steels. The oxidation resistance of stainless steels is due to the formation of a surface Cr_2O_3 film which is an excellent ionic diffusion barrier. Unfortunately, volatile oxides of Cr form above 1173 K or in the presence of high flow rates of oxygen (1), limiting the application of Fe-Cr alloys to lower temperatures. To benefit from increased thermodynamic efficiency at higher temperatures or to enable operation in high flow rates of oxygen it is necessary to find a more oxidation-resistant material.

The superior oxidation resistance of Fe-Al alloys has long been known (2), but the extreme brittleness brought on by Al addition to Fe (3) has prevented their wide-spread industrial use. To obtain the oxidation resistance of a high-Al alloy with the ductility of pure Fe, aluminizing methods such as flame-spraying, pack-diffusing, hot-dipping and vapour deposition are in use (4). Both adhesion and completeness of coverage can be a problem with these techniques, and they always have the undesirable effect of changing tolerances and dimensions. Ion-beam processing has been found to change surface properties such as wear, hardness and microhardness (5). Both chemical and electrochemical properties (6) have also been altered. Improvement of high-temperature oxidation resistance by such techniques has not been fully investigated, probably because the thickness of scale produced by high-temperature oxidation is much greater than the depth modified by ion-beam techniques.

The aim of this work is to investigate the effectiveness of ion-beam techniques in enhancing the oxidation resistance of low-Al Fe alloys at 1173 K, with the eventual aim of finding a ductile, oxidation-resistant material.

CHAPTER 2

THEORY

2.1 Oxidation criteria for alloy evaluation

A protective alloy is one whose products of reaction with oxygen result in long-term inhibition of further reaction with the alloy. This implies that the oxide layer formed must be mechanically adherent, even during thermal shock or cycling. It must also be free of large defects such as pores, cracks or pits, and it must have a low enough level of ionic defects to act as a barrier to ionic diffusion. Reaction with trace elements or oxygen must not result in deterioration of the barrier oxide, and a low vapour pressure is desirable.

To meet such exact requirements, very specific properties are required of the alloying element. Its free energy of oxide formation should be much lower than that of the matrix, to allow exclusive formation of an oxide film even with small concentrations of the alloying element in the alloy. The diffusion coefficient of the alloying element in the alloy should be fast enough that the scale is maintained by transport from the bulk of the alloy. Low oxygen solubility and mobility in the alloy are required to prevent internal oxidation.

The above requirements mean that Al, Cr and Si are the alloying elements most often used for oxidation protection in binary combinations, although many others can be used in more complex alloys (7). Cost, availability and mechanical properties at elevated temperatures mean that the most common matrices to be protected are Fe, Co and Ni (8). In terms of tonnage, Fe is by far the most important.

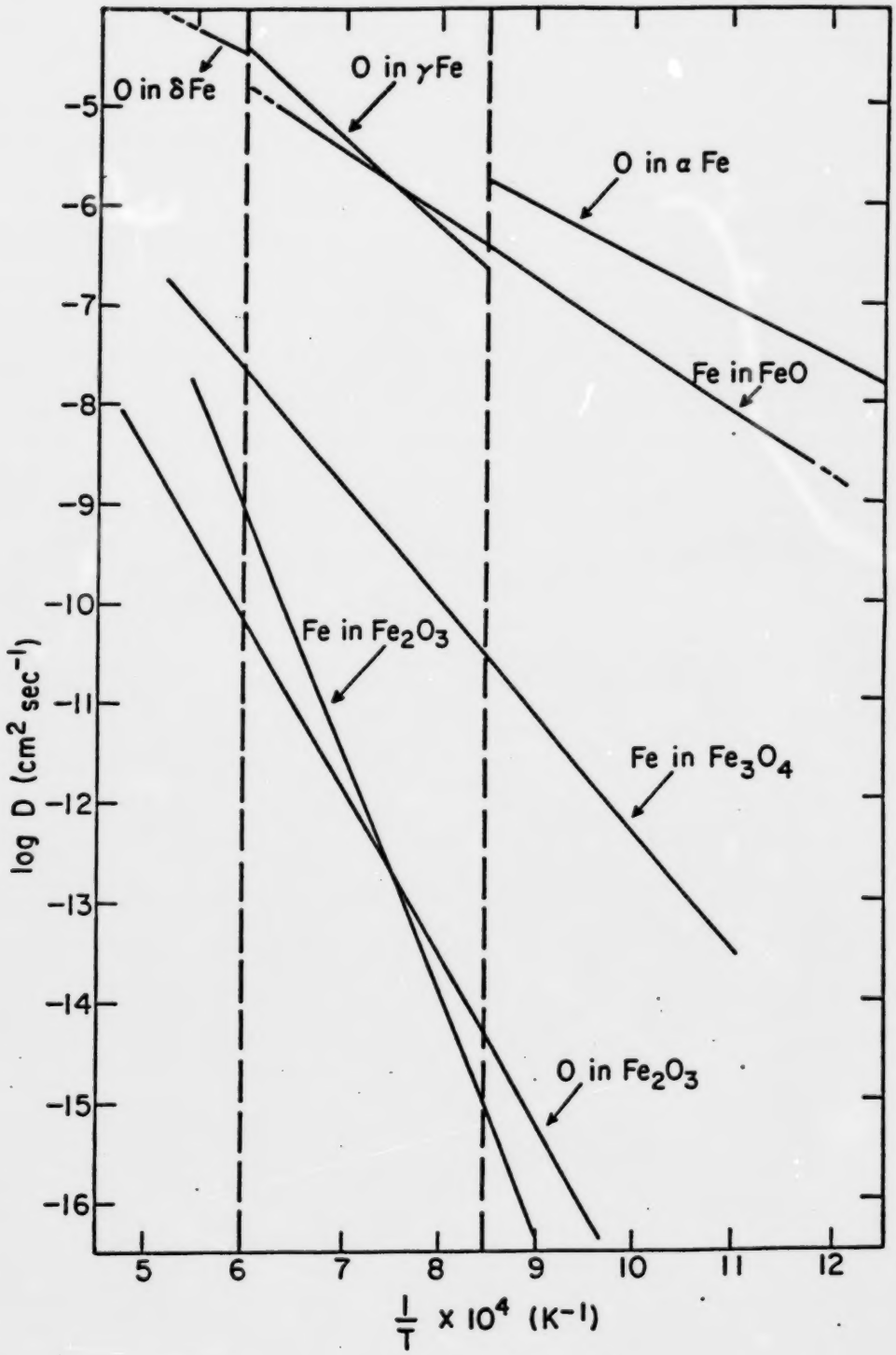

Figure 1. **Fe and O diffusion in Fe and Fe oxides (9).**

2.2 Diffusion and thermodynamic data

(i) Diffusion data.

Figure 1 (9) shows Arrhenius plots for the diffusion of Fe in its three oxides and for O in Fe and Fe_2O_3. Note how much faster diffusion is in the highly-defective FeO, compared to the values for Fe_2O_3 and Fe_3O_4. At 1173 K, Fe_3O_4 and FeO grow by outward Fe diffusion, while the comparable rates of O and Fe diffusion in Fe_2O_3 mean that it will grow by both inward O and outward Fe diffusion. The chemical diffusion coefficient, D, for Fe-Al alloys at temperatures between 1073 K and 1273 K is given in Figure 2 (10). The effect of the order-disorder transition at about Fe-25a% Al is clearly demonstrated. Diffusion coefficients at 1173 K are given in Table 1. Note the enormously slower rates of diffusion in α-alumina compared to alloy diffusion, a result of the very small concentration of defects in α-alumina. Diffusion coefficients for spinel and for γ-alumina are not available, but are assumed to be intermediate between alloy and α-alumina values.

TABLE 1 - Diffusion data for α-Al_2O_3 and α-Fe.

System	Species	D (m^2/s)	Source
α-Al_2O_3	Fe	5.70×10^{-20}	(11)
α-Al_2O_3	Fe	8.53×10^{-17}	(12)
α-Al_2O_3	Fe (mean)	9.15×10^{-16}	(13)
α-Al_2O_3	Fe (G.B.)	1.22×10^{-14}	(13)
α-Al_2O_3	Fe (lattice)	8.49×10^{-17}	(13)
α-Al_2O_3	chemical	1.00×10^{-23}	(14)
α-Fe	Fe	4.15×10^{-15}	(15)
α-Fe	Fe	4.15×10^{-15}	(16)
α-Fe	Fe	4.4×10^{-14}	(17)
α-Fe	Fe	4.4×10^{-14}	(17)
α-Fe	Al	8.6×10^{-14}	(17)
α-Fe	Al	9.7×10^{-14}	(17)

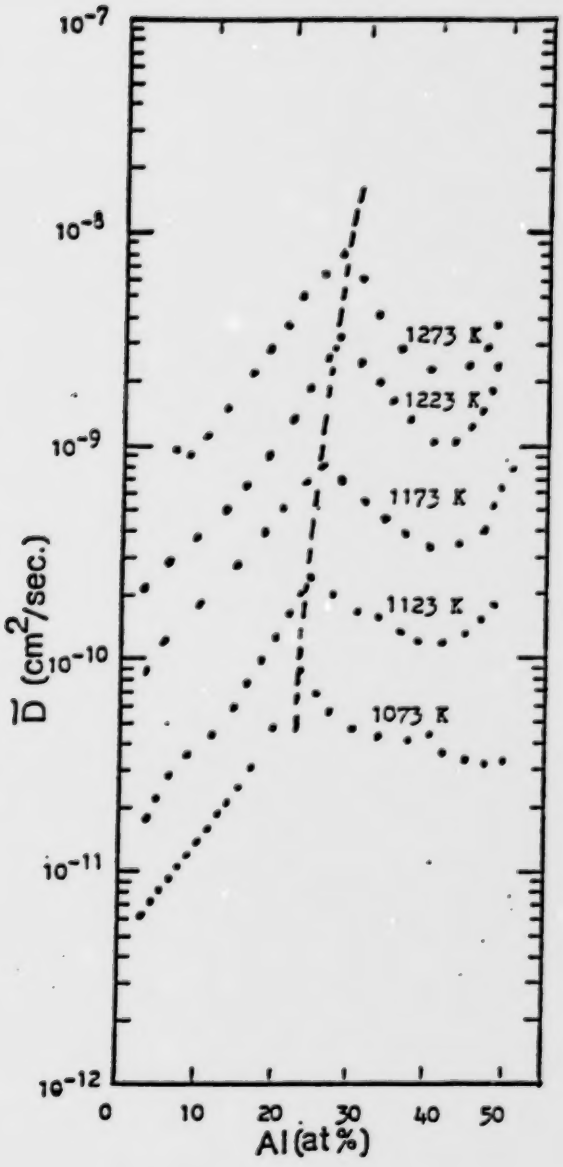

Figure 2. **Chemical diffusion coefficients in Fe-Al alloys (10).**

(ii) Thermodynamic values for the Fe-Al system.

The alloys investigated, Fe-2 to 9.8a% Al, are all α-Fe (BCC) both at room temperature and at the temperatures of this investigation. Only the Fe-2a% Al alloy is capable of transforming to γ-Fe (FCC), and only if heated to 1423 K. The Curie temperature for transformation to a non-magnetic condition is 1042 K for pure Fe, decreasing to perhaps 1023 K for Fe-9.8a% Al (Figure 3). Several intermetallics exist (Fe_3Al, $FeAl_3$) but should not be present in the alloys investigated.

The activities of aluminum in Fe-Al alloy given in Figure 4 were determined from the thermodynamic measurements of Radcliffe et al (18). The results of a second determination by Smeltzer and Elrefaie (19) are presented in Figure 5. Both sources show the activity of Al to be much less than the ideal solution value.

(iii) Thermodynamic values for the Al-O system.

Two forms of Al_2O_3 exist, γ and α-Al_2O_3. α-Al_2O_3 is a rhombohedral crystal, with a very low level of ionic defects and extremely low diffusion rates. γ-Al_2O_3 has a higher level of defects and microscopic crystals of spinel structure (20). Table 2 presents free energy of formation data for the two forms.

TABLE 2 - Free energies of formation for the Al-O system at 1173 K.

Oxide	ΔG_f (kJ/mole)	Reference
γ-Al_2O_3	-1306	(21)
α-Al_2O_3	-1320	(21)
α-Al_2O_3	-1309	(19)

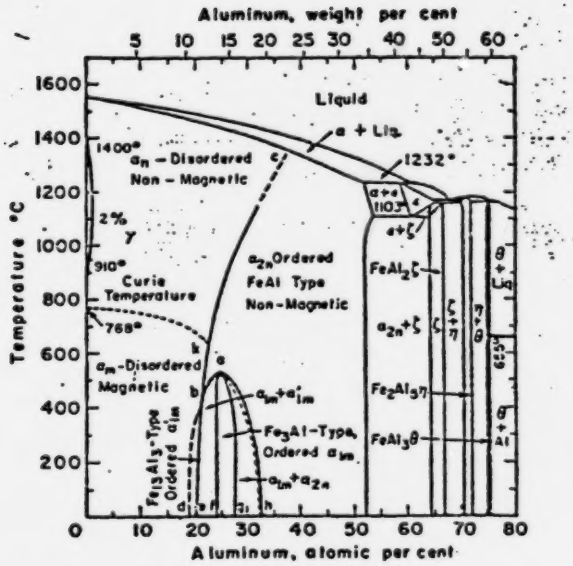

Figure 3. Fe-Al phase diagram (18).

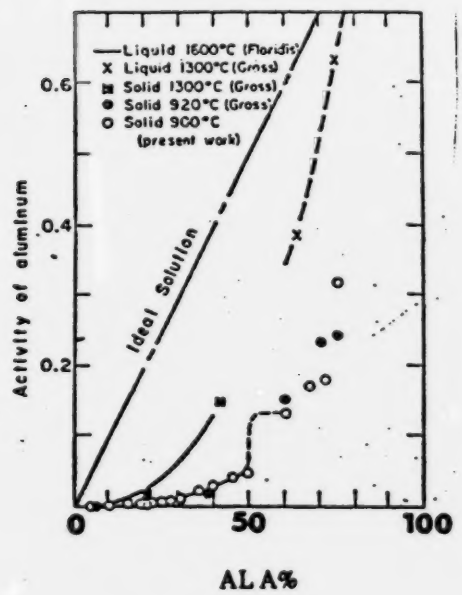

Figure 4. Al activity in Fe-Al (18).

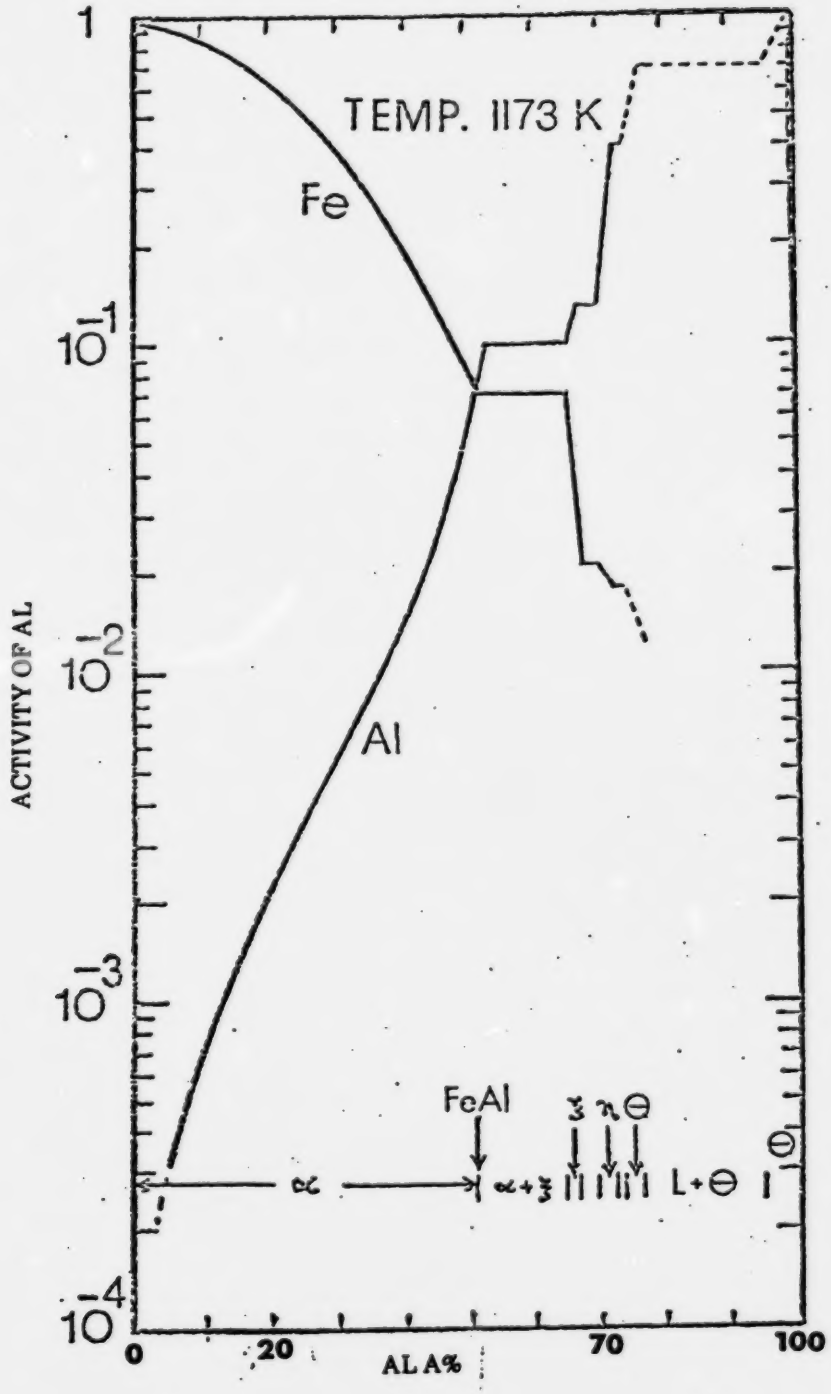

Figure 5. Semi-log plot of Al activity in Fe-Al (19).

iv) Thermodynamic values for the Fe-O system.

The sequence of phases for the Fe-O system is shown on Figure 6 (22), and free energy data for the three oxides are given in Table 3.

TABLE 3 - Free energies of formation for the Fe-O system at 1173 K.

Oxide	ΔG_f (kJ/mole)	Reference
Fe_2O_3	–531.0	(21)
Fe_2O_3	–461.0	(23)
Fe_3O_4	–732.1	(24)
Fe_3O_4	–755.1	(21)
FeO	–199.2	(21)
FeO	–187.8	(25)
Fe O Wustite	–191.4	(21)

v) Thermodynamic values for the Fe-Al-O system.

Most early work on the phase equilibria of Fe-Al-O was motivated by a desire to characterise reduction processes in steel-making, or the reactions between refractory linings and molten steel. Atlas and Sumida (26) and Elrefaie and Smeltzer (19) have established Fe-Al-O phase relations between 1073 and 1523 K. Atlas and Sumida's investigation did not extend to 1173 K, but their results for 1273 K are shown in Figure 7 and Elrefaie and Smeltzer's at 1173 K are shown in Figure 8. With these data, diffusion paths can be plotted and experimentally-observed morphologies can be interpreted. Both works suggest that the only phase in equilibrium with Fe-Al alloys is alumina, even in the case of alloys only slightly enriched in aluminum.

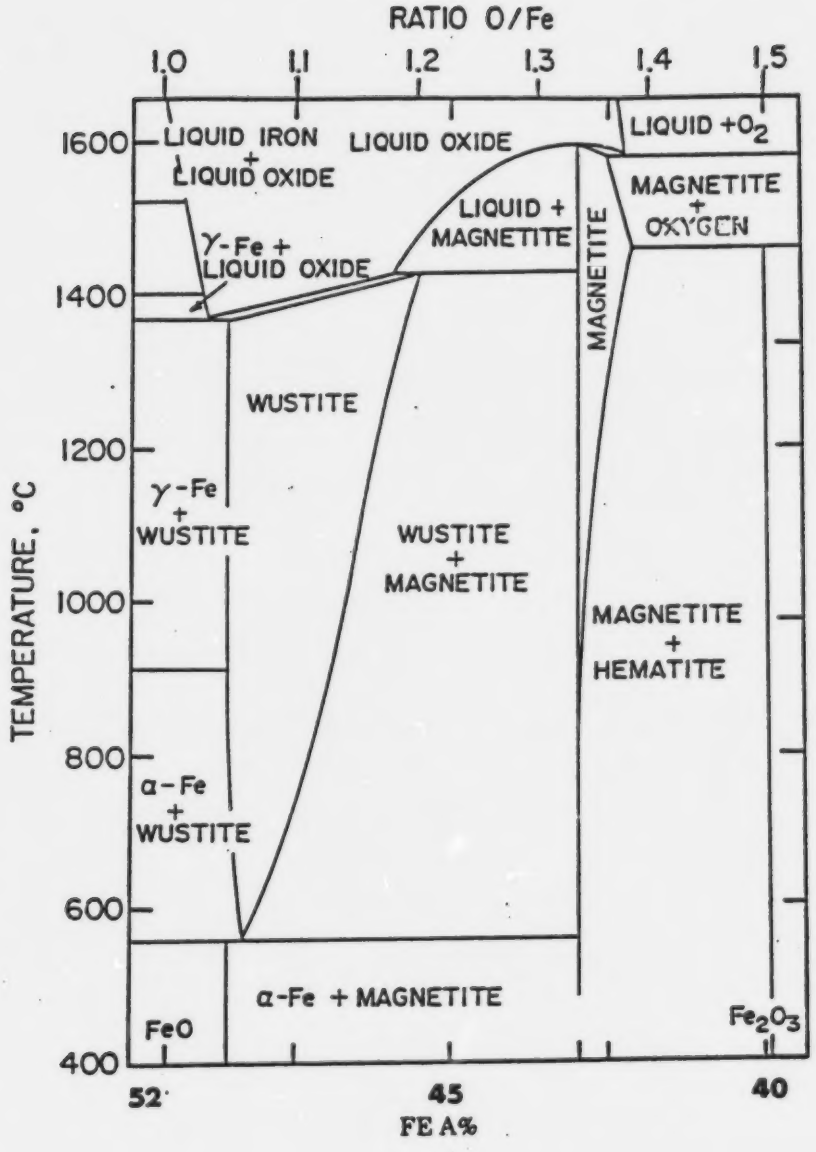

Figure 6. Fe-O phase diagram (19).

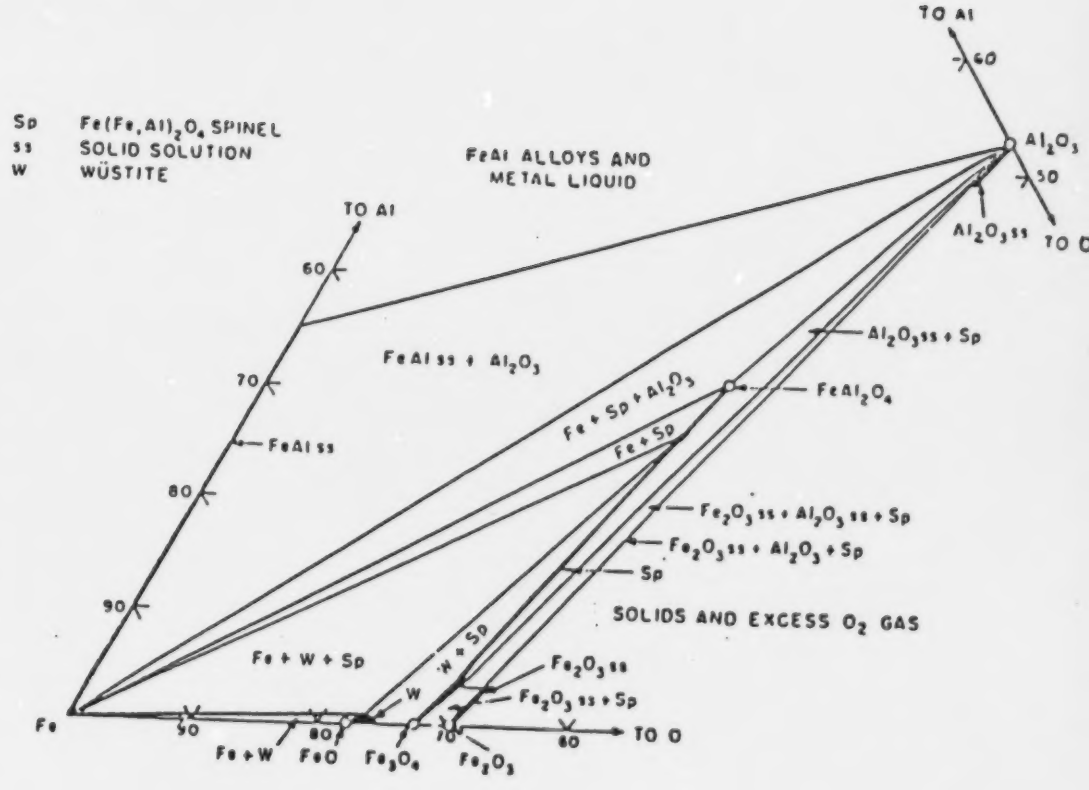

Figure 7. **Phase relations in the system Fe-Al-O at 1273 K (26).**

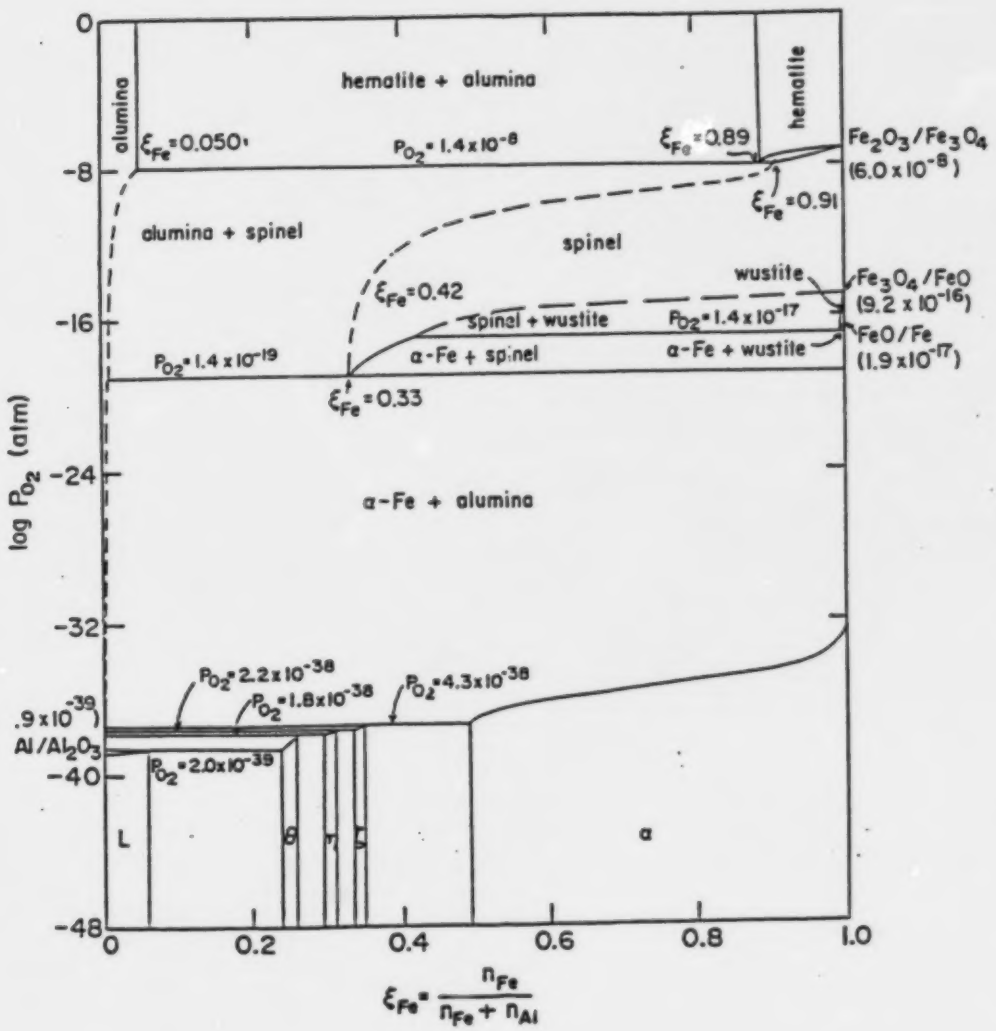

Figure 8. **Fe-Al-O equilibrium oxygen pressures at 1173 K (19).**

Wustite, the most undesirable oxide because of its high degree of non-stoichiometry, is never in equilibrium with alumina. At 1173 K, hercynite and magnetite are completely miscible, and only one phase appears in that region.

Free energies for the reaction:

$$2Fe + O_2 + 2Al_2O_3 \rightleftharpoons 2FeAl_2O_4$$

are presented in Table 4. The value attributed to Elrefaie and Smeltzer was calculated from the pressure of coexistence quoted by these authors.

TABLE 4 - Free energies of reaction for Spinel/Alumina/Alloy co-existence at 1173 K.

ΔG_r (kJ/mole)	References
–509	(27)
–424	(28)
–422.7	(29)
–423.9	(19)

2.3 Diffusion paths (30)

A relationship between the two components of a binary alloy and oxygen can be found by solution of the corresponding transport equations. For parabolic oxidation, the solution is independent of both depth and time, and can be plotted on a ternary isotherm such as Figure 9. If reliable transport and thermodynamic data are available, equilibrium phase relations can be predicted by this method.

The prediction of internal oxidation or precipitation is particularily interesting: should, as in Figure 10, the predicted diffusion path between bulk alloy and alloy/scale interface be entirely in the one-phase region, no internal precipitation will occur. If the diffusion path moves through the two-phase (alloy -oxide) region, as in Figure 11, the

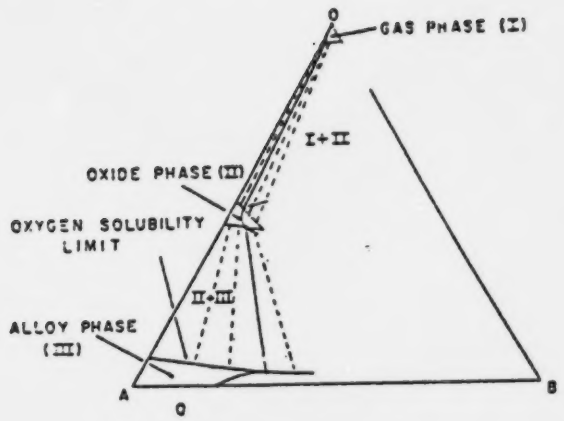

Figure 9. Example of diffusion path (30).

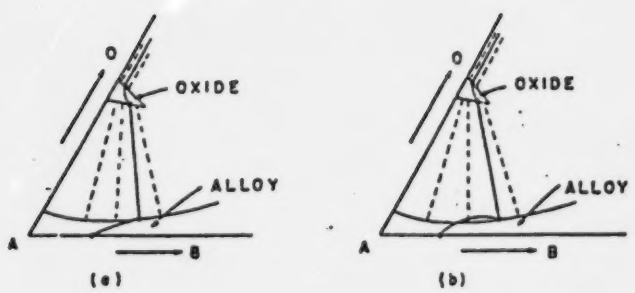

Figure 10. **(a) "Virtual" diffusion path which does not involve a supersaturation region in the alloy. (b) "Virtual" diffusion path which does involve a supersaturation region in the alloy (24).**

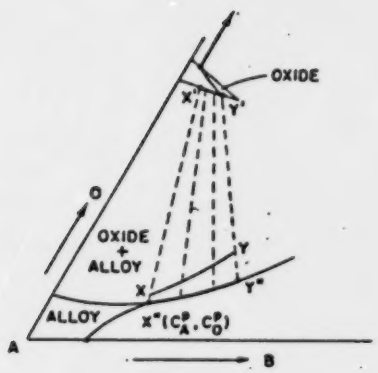

Figure 11. A situation which involves a zone of internal oxidation in the alloy. The variations in the composition of internal oxide and the alloy matrix are given by X'Y' and X"Y" respectively. The line XY represents the mean composition of the subscale region (24).

calculated profile no longer holds and oxide will precipitate below the alloy-oxide interface. The variation in precipitate and alloy composition can also be estimated if tie-lines in the two-phase region are available.

2.4 Theoretical predictions of Fe-Al oxidation.

A first step in predicting the amount of Al to be added to Fe for exclusive formation of an alumina film is examination of the ternary coexistence of $FeAl_2O_4$, alloy and Al_2O_3. The free energy for this coexistence at 1173 K was stated as -423.9 kJ in section 2.2. This is related to product and reactant activities in equation (1):

$$-423.9 = \Delta G = -RT \ln \frac{(a_{Al})^2 (a_{spinel})^3}{(a_{Fe})^3 (a_{Al_2O_3})^4} \tag{1}$$

in which oxide activities can be set to unity, thereby reducing equation (1) to :

$$\frac{(a_{Al})^2}{(a_{Fe})^3} = \exp(423.9/RT) = 10^{-18.8} \tag{2}$$

Aluminum activities in dilute Fe-Al alloys were seen to be very low in Figures 4 and 5 so to a very good approximation:

$$a_{Al} = 10^{-9.4} \tag{3}$$

Even though the Al activity at low concentrations is far below ideality, it appears that a miniscule amount of Al will serve to stabilize alumina. The weakness of this treatment, as with any equilibrium calculation, is that kinetics, nucleation and all other rate considerations are neglected. Even if the predicted equilibrium is accessible, it may not be an enduring condition due to flaws or spalling of the surface scale.

A more sophisticated model is due to Wagner (31) who from a diffusional analysis of the support of an alumina film found that the bulk concentration of Al must be at least:

$$N_{MIN} \geq [k_p \pi / D_{Al}^{Fe}]^{1/2} \frac{\overline{V}_{alloy}}{Z_{Al} M_{Al}} \tag{4}$$

in which the following values are used:

$\overline{V}_{alloy}$ = 7.11×10^{-6} $m^3 mole^{-1}$ = molar volume of α - Fe. (32)

Z_{Al} = +3 = valence of Al.

M_{Al} = 16 = mole mass of oxygen.

k_p = 5.2×10^{-3} $g^2/m^4 s$ = parabolic rate constant of Al_2O_3 (33).

D_{Al}^{Fe} = 9.7×10^{-14} m^2/s = diffusion constant of Al in α-Fe (17)

Solution of equation (4) with the above values gives a value for N_{MIN} of 6 a% Al for the sole formation of Al_2O_3, a more realistic value than the result of the first treatment, but still less than the reported value of between 8 and 12 a% Al (33).

A third and final model (34) determines the enrichment required for the transition from internal to external oxidation, N_{IE}. The slowing of diffusion by the blocking effect of internal precipitates is considered to determine this. Complete blocking is accomplished when the volume fraction of precipitates exceeds some critical value, ϕ_c, which cannot be theoretically determined. By assuming that no diffusion takes place through the internal precipitate, and that any net decrease in diffusion is due to this effect, then N_{IE} is given by:

$$N_{IE} = \left[\frac{\phi_c \pi D_o^{Fe} N_s^o \overline{V}_{Fe}}{2v D_{Al}^{Fe} \overline{V}_{AlO_{3/2}}} \right]^{1/2} \quad (5)$$

in which:

ϕ_c = critical volume fraction

D_{Al}^{Fe} = 9.7×10^{-14} m^2/s = diffusion constant of Al in α-Fe (17).

N_s^o = 2-3 ppm = solubility of O in α-Fe at 101 kPa (35). = .5 ppm at 26.7 kPa (mole fraction 5.5×10^{-6})

$\overline{V}_{Fe}$ = 7.11×10^{-6} m^3/mole = molar volume of α-Fe.

v = stoichiometric coefficient for Al O 3/2

D_o^{Fe} = 1.8×10^{-10} m^2/s = diffusion coefficient of O in Fe (9).

$V_{AlO_{3/2}}$ = 12.84 x 10^{-5} m^3/mole = 1/2 molar volume of alumina (36).

implying that:

$$N_{IE} = (.1072)(\phi_c)^{1/2} \quad (6)$$

Should ϕ_c be as low as 10%, then N_{IE} will be 0.034. Ahmed (33) proposes a value of 30% for ϕ_c at 1173 K and 1 atmosphere of oxygen, for which N_{IE} would be .144, good agreement considering the reliability of much of the data required for an assessment of N_{IE}.

2.5 Previous studies of Fe-Al oxidation

Since the mechanical properties of Fe-Al alloys deteriorate with an increase in Al content, much research has been done to find the minimum Al enrichment for the formation of a protective oxide. This section will attempt to present alloy oxidation behaviour from 573 K to over 1300 K, and identify areas where ion-beam modification of the surface may be profitable.

(i) 573 K: Pure Fe below 843 K oxidizes to form a duplex film of hematite and magnetite. Iron oxides are initially suppressed on a Fe-20a% Al alloy (37) which forms a thin film of γ-alumina after 7.2 x 10^3 s exposure to air. Thicker films of Fe_2O_3 and Fe_3O_4 appear above the alumina layer after longer exposures.

(ii) 673 K: A Fe-30a% Al alloy is sufficiently enriched to form a thin γ-alumina layer (38) at this temperature. Although a buried alumina layer may exist on Fe-13.6 and -20a% Al alloys, only the surface layer, Fe_2O_3, has been identified (38) by glancing XRD.

(iii) 773 to 843 K: Alloys of less than Fe-1.4a% Al oxidize with the same morphology as pure Fe, with an outer layer of hematite and an inner layer of magnetite three times thicker. The alloy with the fastest kinetics is the Fe-.18a% Al alloy, due to the doping effect of Al^{3+} ions in the iron oxides. Between Fe-1.4 and 16a% Al, blocking is attributed to a

spinel layer below the hematite and magnetite layers. In the presence of such a blocking layer, the magnetite layer is much thinner, probably due to the reaction:

$$Fe_3O_4 + 2Al \rightleftharpoons FeAl_2O_4 + 2Fe$$

This reaction (39) is driven by the reduced flow of Fe outward through the spinel layer. Amorphous and γ-alumina appear below the iron oxides on a Fe-20a% Al alloy, probably also resulting in the consumption of magnetite (37).

(iv) 843 to 973 K: Oxidation of pure Fe is much faster above 843 K due to the formation of FeO, which appears below the hematite and magnetite layers. As predicted by thermodynamics, wustite has not been observed on an Fe-Al alloy of any Al content.

In this range, the observed morphology is sometimes dependent on the rate of heating (40), leading to some disagreement in the literature as to just what phases form. Essentially, iron oxides, alumina and spinel form in the first seconds of oxidation on any alloy incapable of forming only alumina. Al then diffuses to the surface, spinel is consumed in displacement reactions, and alumina is produced. If the rate of heating is slow, more iron oxides or spinel will be visible. Fast rates of heating, on the other hand, show alumina to be the predominant protective phase.

Depending on heating rate, alloys of composition between Fe-2 and 10a% Al have either a spinel or an alumina layer below a surface hematite layer. Magnetite is sometimes observed between the hematite and Al-rich oxides, if a barrier to outward cation diffusion has not resulted in conversion of magnetite to hematite (39,41). With Fe-22a% Al, iron oxide is no longer present and an undisturbed alumina film appears (42).

(v) 1073 K: The transition from internal to external oxidation at this temperature has been carefully studied by Tomas (40). The greatest enrichment at which internal oxidation was observed was Fe-3.8a% Al, and the sequence of morphologies proposed for it are shown in Figure 12. Note that some "internal" precipitates are actually buried surface

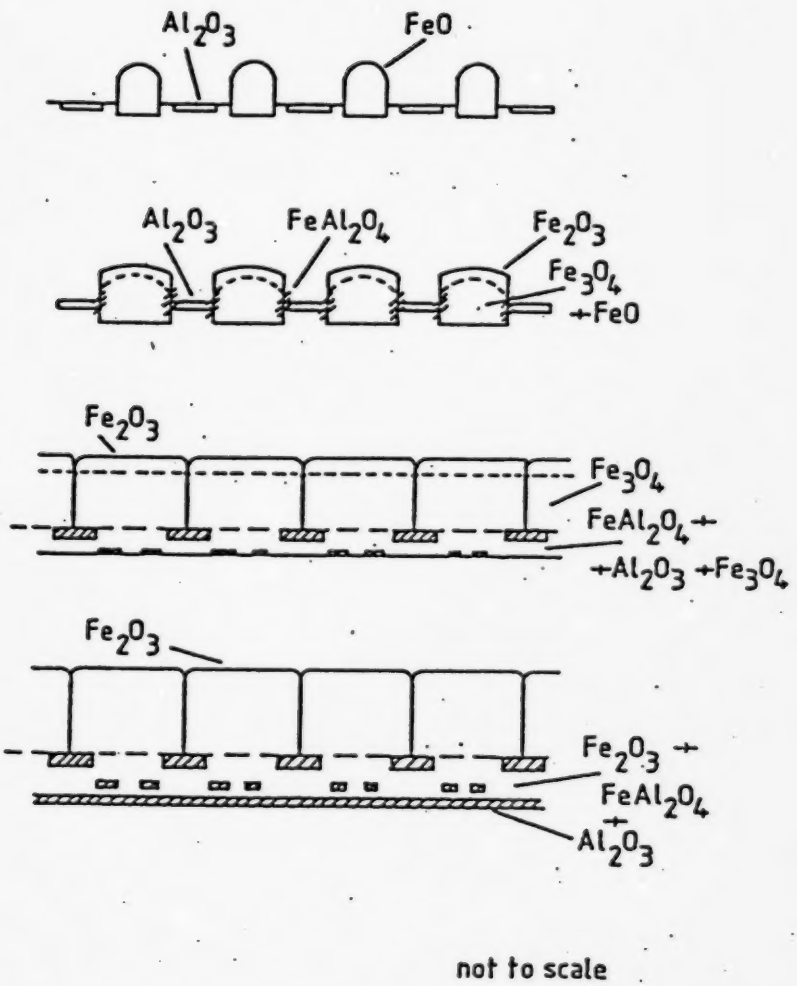

Figure 12. **Schematic representation of oxidation of Fe-3.8a% Al alloy at 1073 K (40).**

layers. Alloys enriched to between 4.8 and 13.3a% Al had varying degrees of nodule growth through an alumina film. Very few nodules appeared on the 13.3a% Al alloy, while the 4.8a% Al alloy was quite overgrown. An enrichment of 14a% Al was required for complete suppression of the nodules.

(vi) 1173 K: A similar investigation was carried out at 1173 K in air, wet oxygen and dry oxygen by Ahmed (33). Lower alloy concentrations (Fe-1.5 and 3a% Al) produced platelets of spinel precipitate below a thick scale of magnetite and hematite. The Fe-5a% Al alloy in its early stages resembled the 1.5 and 3a% Al alloys, but an Al_2O_3 film formed below the internal precipitation zone after 8.6×10^4 s. The blocking effect of this layer resulted in conversion of the internal precipitation zone to a triplex hematite/magnetite/alumina morphology after 5.2×10^6 s.

Some attention was given to the structure and growth of the internal precipitate, which appeared as rods of spinel with alumina at the tips. Oxygen for growth of the rods was proposed to arise from the reaction:

$$Fe_3O_4 \rightleftharpoons 3Fe + 4O$$

which occurs at the scale-alloy interface when thickening of the external scale drops the activity of oxygen below magnetite's dissociation pressure. The oxygen resulting from this dissociation diffuses inwards to react with aluminum at the internal precipitation front, forming Al_2O_3. As the reaction proceeds, the Al_2O_3 reacts with Fe to form the spinel which makes up the bulk of the internal precipitate. Fe-7 and 8a% Al alloys produced thin reddish films of hematite on alumina, with no internal oxide precipitation. An Fe-11.7a% Al alloy produced an undisturbed alumina film. Diffusion paths for these morphologies are plotted on Figure 13.

(vii) 1273 K: The formation of an alumina scale is reported on Fe-7 and 8a% Al alloys at this temperature, while the familiar hematite on alumina structure forms on Fe-5a%

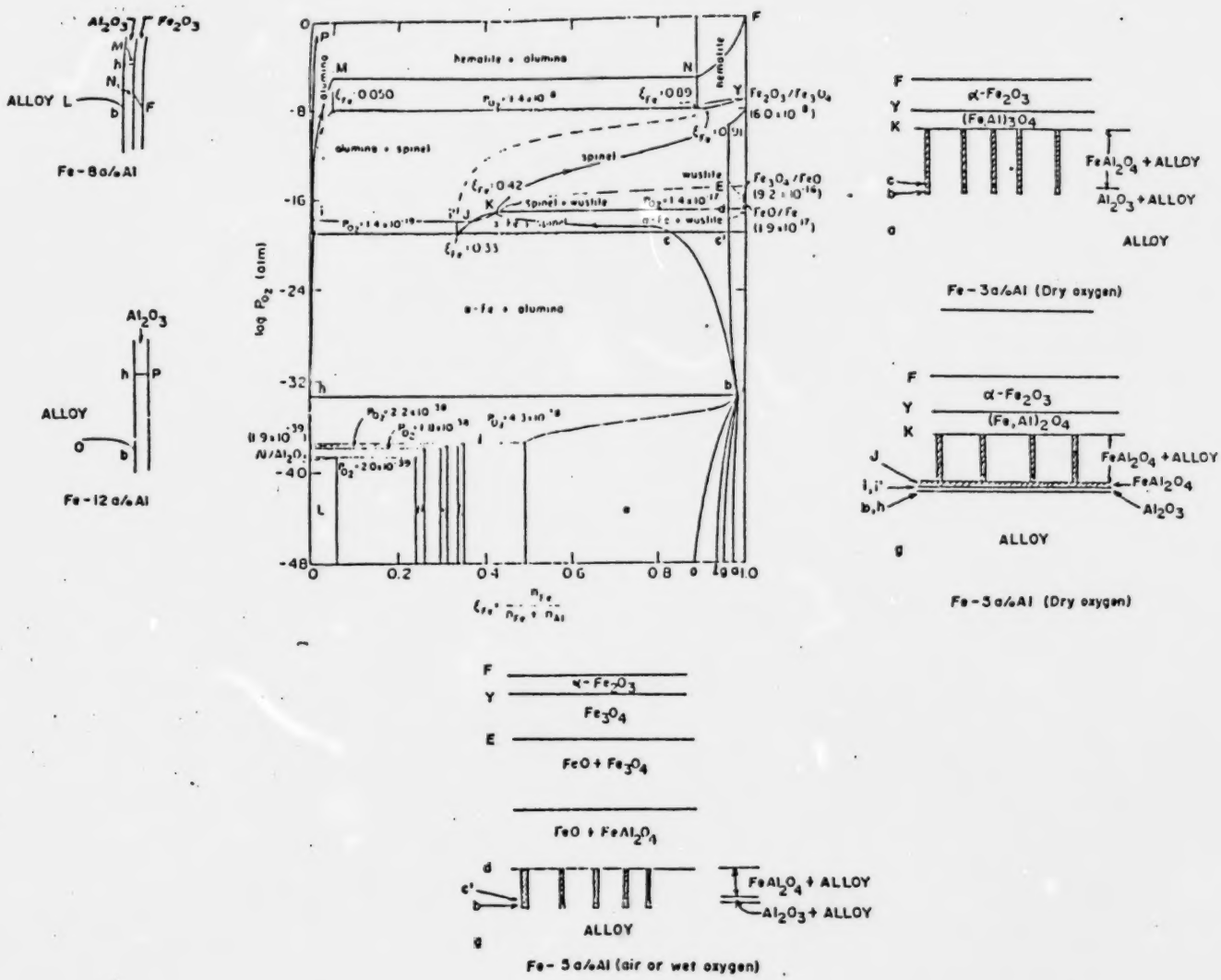

Figure 13. Diffusion paths at 1173 K (19 & 33).

Al (43). Alumina being formed at so low an enrichment may be the result of higher aluminum mobilities at this temperature. Identification of alumina was made by EDAX elemental mapping, however, not a phase-specific method, and a thin layer of hematite on the surface may have been overlooked.

(viii) >1273 K: At 1373 K, alumina was identified on both Fe-8a% and 22a% Al alloys (42). Fe_2O_3 clusters appeared on a Fe- 8a% Al alloy at 1423 K, and massive nodule growth led to the breakdown of parabolic kinetics at 1473 K.

Nodule formation has been seen from 1073 to 1523 K, at times as short as five minutes and on alloys of up to 12a% Al. The weight gain associated with nodules can be much greater than the weight gain of the accompanying alumina film. The most accepted theory of nodule formation prposes that on alloys with just enough Al to form an alumina film, a depleted zone forms below the oxide. If there exists a flaw or crack in the alumina film, the depleted zone will rapidly oxidize with a morphology resembling that of a much less enriched alloy. If the alloy is rich enough in Al, or if diffusion is fast enough, a healing layer of spinel or alumina may form beneath the nodule, leading to bimodal kinetics (39).

Tomas (40) advances a second theory (Figure 14) as a logical extension of the mechanism of Figure 12, implying that no flaw or crack is needed for nodule formation. As nodules appeared at early exposure times in Tomas' work, his model does not require a flaw for nodule growth. The presence of water vapour can speed nodule growth and eliminate the induction period (39), perhaps this is why he observed nodules immediately.

No early exposure mechanisms have been proposed for less-enriched alloys at 1173 K or higher, but the thin films found on alloys of over 7a% Al have been modelled (33). Duplex films formed on such alloys consist of about 100 nm of hematite on 300 nm of alumina. The hematite probably forms by outward Fe diffusion through short-circuit paths in the alumina, which forms immediately. Depletion of Fe below the short- circuit paths results

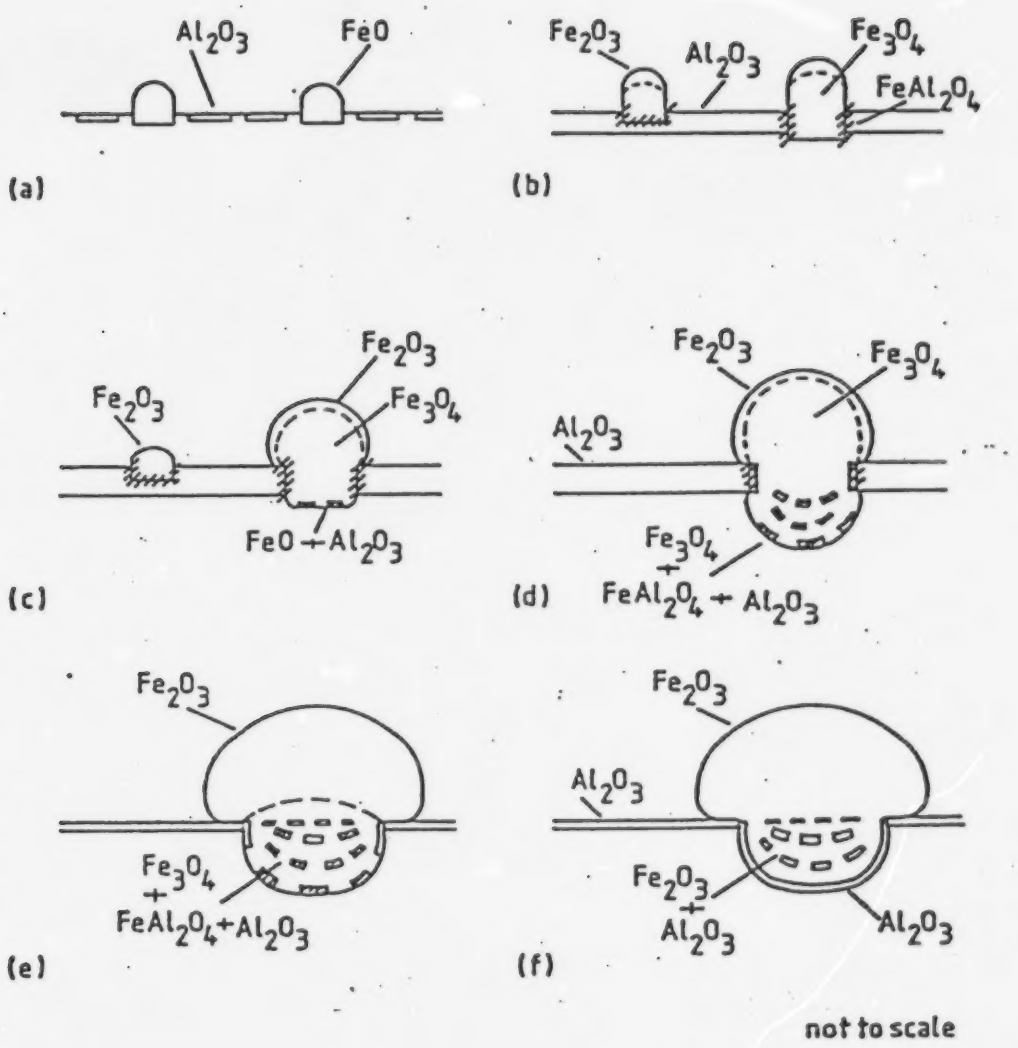

Figure 14. **A diagramatic representation for the progressive formation of iron oxide nodules on binary iron-aluminum alloys containing between 4.8 and 13.3 a% aluminum.**

in alumina formation and lessening of the flux of Fe. If a near-surface enrichment could seal off these paths, initial rates could be reduced and formation of an exterior hematite layer prevented. On the other hand, formation of a highly defective or very fine-grained Al_2O_3 film due to the damage caused by implantation could have the reverse effect.

For the high temperature region (1073-1273 K) of interest, some statements can be made about the potential benefits of ion-beam modification. The alloy enrichment for exclusive alumina formation is probably 12-14a% Al - enough to seriously embrittle the alloy. If the theory advanced in Figure 12 is correct, Al_2O_3 does initially form, but is buried by fast-growing FeO, which also forms. If ion-implantation could enrich the near-surface region enough to suppress initial formation of FeO, perhaps an undisturbed alumina film would result. Nodule growth may also require the initial formation of FeO, so enrichment by ion - beam methods may be able to suppress these as well.

What is known of the oxidation mechanisms and behaviour of Fe-Al alloys at high temperature suggests that ion-beam modification of the near-surface region could have a beneficial effect on oxidation, despite the very small volume enriched.

2.6 Ion-implantation fundamentals

Energetic ions incident on solids lose energy by two distinct mechanisms: electronic and nuclear stopping. These mechanisms are understood well enough to allow prediction of the distribution of ions at rest and of the damage created by the slowing-down process. To make mathematical analysis possible, several assumptions are usual:

i) The solid is assumed to be a random array of atoms, with no crystal structure or defects. This assumption neglects both channeling and focussed collision events, processes which tend to result in deeper penetration by a small fraction of the incident ions.

ii) Collisions are assumed to be elastic and to occur between a stationary atom and a moving projectile. This assumption is not valid at the end of an ion's track, where many low-energy recoils are created in a small volume, and may collide with each other.

iii) Electronic and nuclear stopping are assumed to be independent. In fact, both are dependent on the impact parameter, the undeflected distance of closest approach. The dependence of electronic stopping on the impact parameter is, however, so weak that it can be modelled as a viscous drag force.

iv) The medium is assumed infinite, and all ions are considered to be initiated at a single plane corresponding to the surface. This leads to a small overestimation of the near-surface concentration, as real particles can only be scattered across the surface plane once.

Nuclear stopping.

Nuclear stopping is the result of an ion approaching a nucleus and being deflected with some energy, T, transferred to the nucleus. The deflection is due to the repulsive force between the two positively charged nuclei, screened by the intervening electrons. The angle of deflection in the centre of mass system is related (44) to the interatomic potential and the impact parameter by:

$$\theta_{com} = \pi - 2p \int_{o}^{\mu_o} (1 - \frac{V(\mu)}{E'} - p^2 \mu^2) d\mu \qquad (7)$$

in which:

p = impact parameter

μ_o = reciprocal minimum seperation

μ = reciprocal seperation

$V(\mu)$ = interatomic potential

$$E' = M_2 E_o/(M_2 + M_1)$$

To calculate this integral, the interatomic potential is approximated by the Thomas-Fermi (45) potential:

$$V(\mu) = Z_1 Z_2 e^2 \mu \chi(\mu, a) \tag{8}$$

which is a combination of the effects of coulombic repulsion and χ, screening by electrons. The screening length, a, is calculated (46) from a_o, the Bohr radius for a hydrogen action:

$$a_o = 52.9 \text{ pm} \tag{9}$$

by Lindhard's expression:

$$a = \frac{.8853\, a_o}{(Z_1^{2/3} + Z_2^{2/3})^{1/2}} \tag{10}$$

With the angle of deflection known, the energy transferred to the target atom can be calculated (44) as:

$$T = 4\, M_1 M_2 / (M_1 + M_2)^2 E \sin^2(\theta/2) \tag{11}$$

Any ion-target collision characterised by an impact parameter within dp of p will be deflected within $d\theta$ of θ_{com}. This suggests a cross-section, $d\sigma_n$, representing the area differentially close to a radius of p:

$$d\sigma_n = 2\pi\, p\, dp \tag{12}$$

Equations (7) and (11) allow conversion of the right-hand side of (12) to an expression in terms of T. The rate of loss of energy to nuclear collisions (nuclear stopping) is then:

$$\left[\frac{\partial E}{\partial x}\right]_n = N \int_o^{T_{max}} T \frac{\partial \sigma_n}{\partial T}\, \partial T \tag{13}$$

Electronic stopping.

As mentioned in assumption iii), electronic stopping is modelled as a path-independent force, causing no change in direction. For ions with velocity less than the Bohr velocity, v_o, electronic stopping is nearly proportional to ion velocity (47). Therefore:

$$\left[\frac{\partial E}{\partial x}\right]_{el} \alpha\, E^{1/2} = KE^{1/2} \tag{14}$$

Electronic stopping dominates for high energies and low Z ions, while the contribution of nuclear stopping increases with decrease in energy.

Range distributions.

Moments of the at-rest ion distribution are gained by solution of the Boltzmann transport equation with the assumption of a Gaussian distribution of particles around the mean range (48). The Edgeworth expansion on this Gaussian uses higher moments of the distribution to account for the effect of the ratio of ion mass to target mass. If the ion is a light particle, the distribution will be skewed towards the surface. If it is heavier than the target, the distribution will be skewed inwards. Defining the nth moment of the distribution as:

$$\mu_n = <\Delta X^n> \tag{15}$$

and

$$\xi = (x - <\Delta X>) / <\Delta X^2>^{1/2} \tag{16}$$

then the distribution function, F(x), is:

$$\begin{aligned} f(\xi) = 1 &- (\mu_3/6\,\mu_2^{3/2})(3\,\xi - \xi^3) \\ &+ 1/24\,(\mu_4/\mu_2^2 - 3)(3 - 6\,\xi^2 + \xi^4) \\ &- 1/72\,(\mu_3^2/\mu_2^3)(15 - 45\,\xi^2 + 15\,\xi^4 - \xi^6) \end{aligned} \tag{18}$$

This is a good description of ballistically-determined distributions, but there are certain kinetic effects which should be considered. If the implantation takes place at a high enough temperature, diffusion of the implanted species, aided by the larger than thermal equilibrium number of defects due to radiation damage, will cause a change in the as-implanted profile. Segregation, again possibly aided by radiation damage, may cause preferential concentration of one element at the surface. If the dose is large enough, the

concentration of the implanted element may reach a large atom fraction. In this case, the stopping power may be expected to change and the distribution may approach that of self-implanted projectile element. Also at these large doses, precipitation could result from exceeding the solid solubility of the implanted species in the matrix. The most significant kinetic effect is that of sputtering, which places an upper limit on the enrichment possible with implantation. As projectile ions impinge upon the surface, ejection of material from the first few atomic layers takes place, due to the scattering backwards of projectiles or target atoms. When a target reaches the point where every incident ion results in the ejection of one already-implanted ion, then a steady-state has been reached, and no net increase in the amount of implanted species is possible. The Gaussian profile observed at low doses or in the absence of sputtering evolves into an erfc profile for these high dose situations. To demonstrate the effect of sputtering on the shape of an as-implanted profile, three profiles are given in Figure 15 for self-implanted Al with three different doses.

Three programs were available to predict as-implanted distributions: WINBON (50) was used to calculate moments of distributions by interpolation among the ion combinations tabulated by Winterbon. DISTBN (51) was used to calculate the distribution of ions including the effect of the Edgeworth expansion and sputtering. NUDIST (52) was used to calculate distributions considering the effect of significant concentrations of implanted species in the target. No attempt was made to model segregation or diffusion.

2.7 Ion-beam mixing theory

To create a volume enriched above the sputter limit in some desired element the technique of ion-beam mixing is often used. One or more evaporated films can be intermixed with each other or the substrate by bombardment with energetic ions, often of an inert gas.

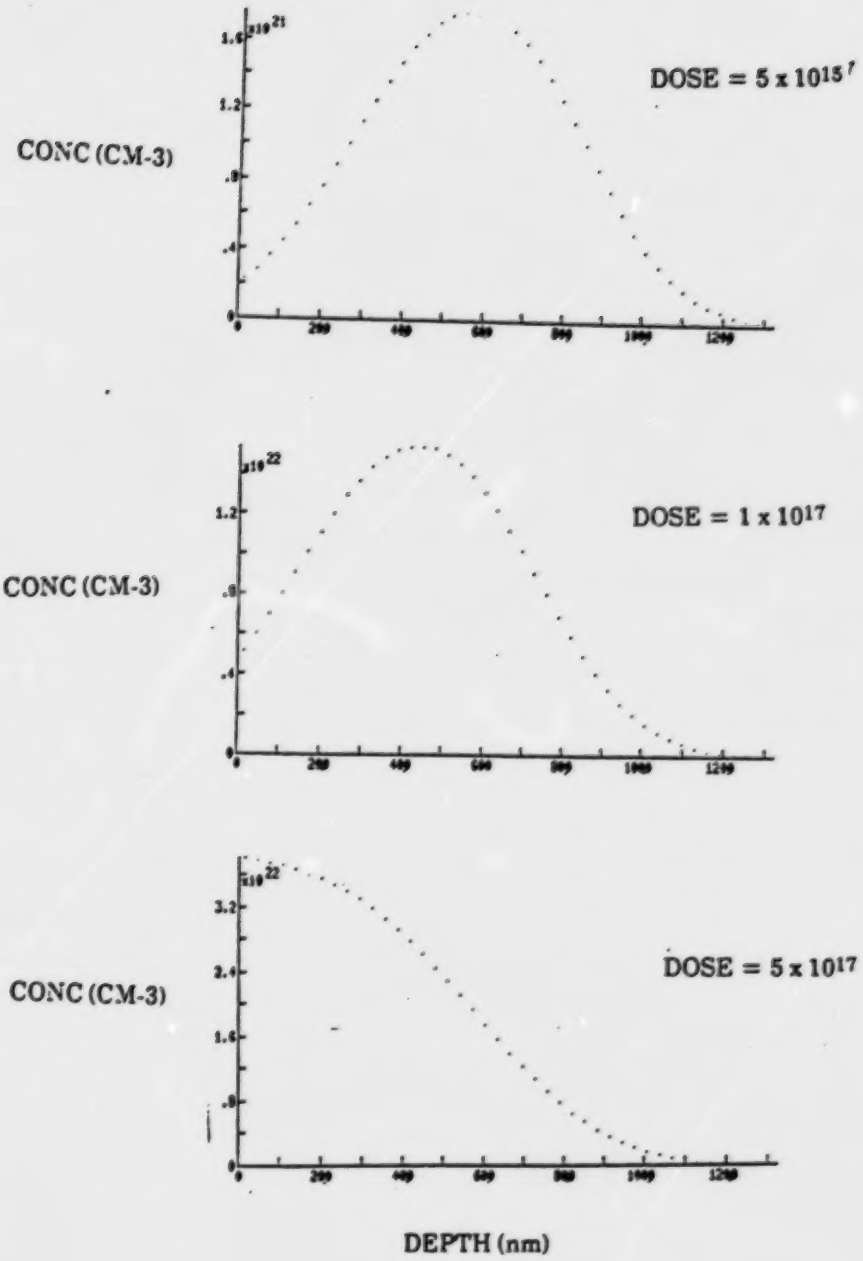

Figure 15. Evolution of depth profile of 100 kV Al implanted into pure Fe with three different doses.

Figure 16 illustrates a typical configuration for a mixing experiment. This section will describe qualitatively the mechanisms of intermixing.

i) Recoil implantation or mixing. Primary knock-ons are generally the most energetic, and may have enough energy to cross the interface between evaporated layer and substrate. The number of such recoils is quite small as the cross-section for nuclear collision is small at high energies. The effect of recoil mixing is to implant a small number of atoms more deeply into the sample than the other contributions.

ii) Cascade mixing. The ion as it slows down will create a large number of primary recoils, as well as large numbers of secondary and higher order recoils. The energy deposited into these recoils creates a "cascade" of moving atoms as depicted (53) in Figure 17. At the end of an ion's track, the cross-section for scattering may get so large that the mean free path between collisions with target atoms can approach the interatomic distance. Some of the assumptions in section 2.6 are no longer valid in such a situation as nearly every atom in a small volume is displaced and collisions occur between recoiling atoms. The end result is a volume such as the one depicted in Figure 17, where an interstitial shell surrounds a void (54). The direction of travel for an ion which creates such a "displacement spike" is nearly random, as after a few collisions the ion may be travelling in any direction. This does not hold for a heavy ion, which is more likely to be travelling in the forward direction because of its large momentum. For light ions, the contribution of "cascade" mixing is modelled by "random flight" calculations (55). The development of concentration profiles can be described using standard diffusion

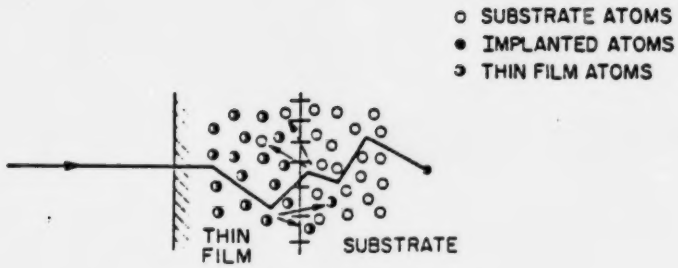

Figure 16. Schematic of the sputtering and atomic mixing processes using energetic ion beams (54).

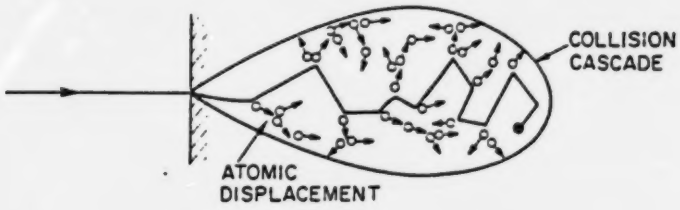

Figure 17. Schematic of the implantation and damage processes using energetic ion beams (54).

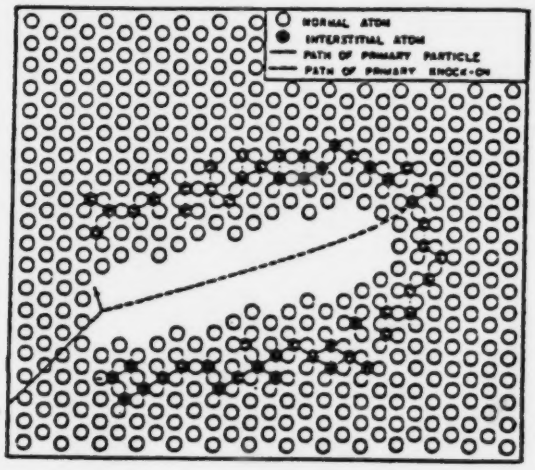

Figure 18. Schematic of a displacement spike (56).

equations and a diffusion coefficient related to the dose and energy of implanted ions.

Scattering cross-sections increase with increasing ion Z, so that a heavy ion may have a great deal of energy when its mean free path approaches the interatomic spacing of the target. "Thermal spike" behaviour is thought to occur (56) when the average energy imparted to atoms in the cascade region or a sub-cascade region exceeeds that required for a phase change such as melting. Thermal spikes are not fully understood or accepted, but could be considered as "freezing in" extensive damage by their extremely fast quenching times, which can be as little as 1×10^{-13} s.

iii) Radiation-enhanced diffusion. Each incident ion can create some thousands of vacancy- interstitial pairs. Steady-state defect concentrations and diffusion rates can exist during bombardment much larger than the thermal equilibrium values (57). The enhanced intermixing which this causes can again be modelled with standard diffusion equations, and diffusion coefficients calculated from knowledge of defect creation and annihilation rates. The coalescense of defects into more stable extended defects can result in quite long-term rises in diffusion rates.

iv) Thermodynamic considerations. Treatment of ion-solid interactions as if atoms were chemically inert often well describes experimental data. The speed and end result of ion-beam mixing are, however, affected by the chemical affinities of evaporated film, substrate and projectile atoms. The disordered zone that exists at the end of an ion or knock-on's track exists only because the extremely fast quench time freezes in this thermodynamically unfavourable situation. Thermodynamics,

particularily that developed to treat meta-stability and unstability, must apply to the relaxation into a final state of these disordered volumes.

While the progress towards stability cannot be followed for individual cascade volumes, phase formation can. Figure 19 shows σ^2, the broadening of two buried marker layers, plotted against fluence. The thinner layers (1 nm thick) broaden with a first order dependence on dose at both room temperature and 77 K. The thicker (23 nm) layers, particularily at room temperature, initially mix faster than the thin layers, quite slowly in the region where a stable phase could exist, and somewhat faster afterwards. Clearly, phase formation has an effect on the progress of mixing.

The equilibrium phase diagram can also yield clues as to the speed and result of mixing, as elements mutually insoluble on an equilibrium phase diagram have been shown to mix more slowly than ballistically similar elements more soluble in each other (59).

2.8 Previous studies of Ion-Beam Mixing of Fe-Al

Barcz and Nicolet (60) used RBS to examine the kinetics of ion-beam mixing between 80 and 300 K for five different thin (1 nm) markers in an Al matrix. The variance of the marker profiles was used as a measure of mixing, as it results from greater dispersion of marker atoms. This kind of configuration allows the measurement of ion-beam mixing produced solely by cascades and radiation-enhanced diffusion. Recoil implantation of the marker is unlikely and "chemical" effects are minimised by the thinness of the marker layer. Figure 20 shows a first-order dependence of mixing on fluence for markers of Pt, Au, W, Fe and Ti in either Al or alumina. This is the dependence expected for isotropic cascade mixing, but the accuracy of the experiment did not allow conclusions to be drawn about the dependence of mixing on marker mass.

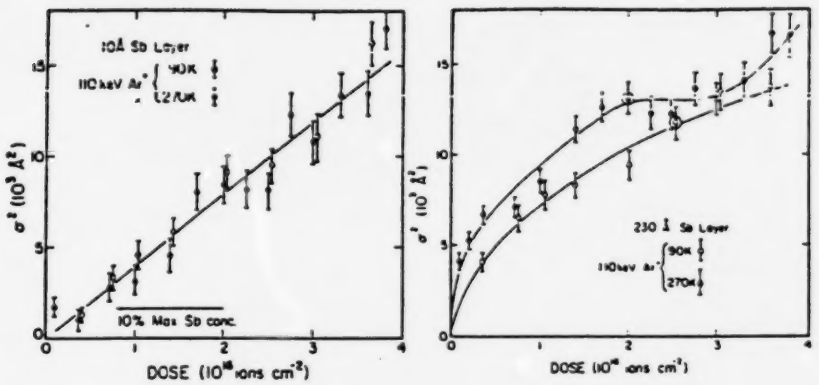

Figure 19. (a) Variance of the irradiation-induced spreading of the 1 nm Sb layer plotted against irradiation dose. The solid line was drawn to fit both 90 K and 270 K data. (b) Variance of the irradiation-induced spreading of 23 nm layer plotted against irradiation dose. The lines were drawn through the data points. The rings indicate the points at which the peak Sb concentration reached 50 a%. (58)

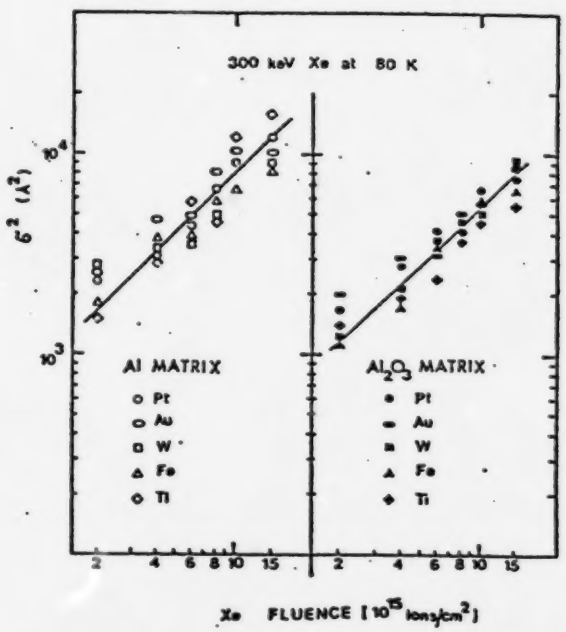

Figure 20. Variance of the marker profiles due to irradiation with 300 kV Xe ions at 80 K plotted against Xe fluence (60).

Jaouen et al (61) investigated two configurations: a single layer of Al over a Fe layer and many alternating layers of Fe and Al. The average composition of a fully mixed bilayer was 40a% Al and the average composition of the fully mixed multi -layer was 58a% Al. Mixing was carried out at 77 K and room temperature, and the total resistivity of the films was used as a measure of mixing. The resisitivity of a film is increased by the presence of a heavily mixed volume, and not at all affected by the creation of slightly mixed volumes by recoil implantation. By assuming that the change in resistivity is due to the formation of a completely mixed volume with a certain resistivity, a "mixed volume fraction", C, could be calculated and fit to the model:

$$C = 1 - \exp(A\,\phi^n) \qquad (19)$$

using the data of Figures 21 and 22. The value of the exponent, n, and the fluence required to bring about complete mixing, Φ_{CRIT}, are listed in Table 5.

TABLE 5. Results of Jaouen et al. (62)

Target	Ion	n		Φ_{CRIT}	
		LN2	RT	LN2	RT
Bilayer	200 keV Xe	.5	.8	2.5×10^{-16}	1.2×10^{-16}
Multilayer	380 keV Xe	.5	.8	1.0×10^{-16}	4.0×10^{-15}

The square-root dependence of C on fluence at 77 K was explained by the authors as being the result of isotropic cascade mixing. Ion-beam mixing at room temperature was faster than could be explained by radiation-enhanced diffusion, suggesting that some "chemical" effect was accelerating the mixing.

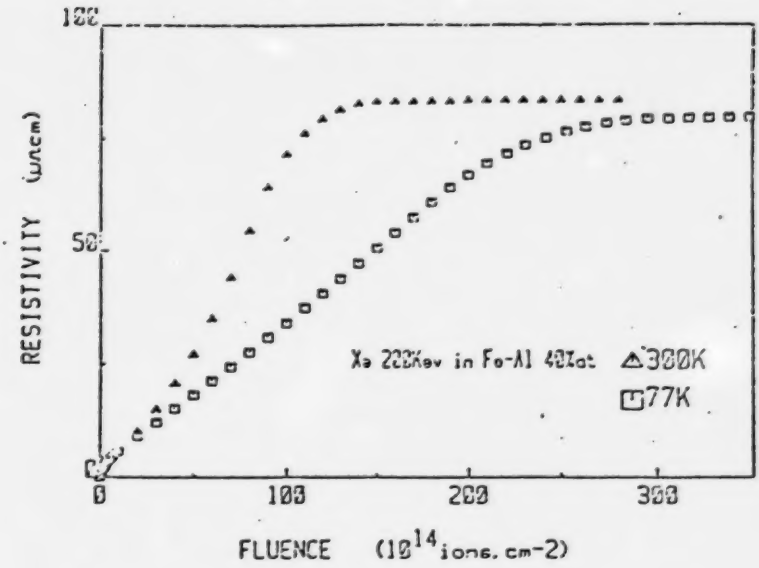

Figure 21. Electrical resistivity at 77 K and 300 K during ion beam mixing of a bilayer for a final composition Fe-40 a% Al (61).

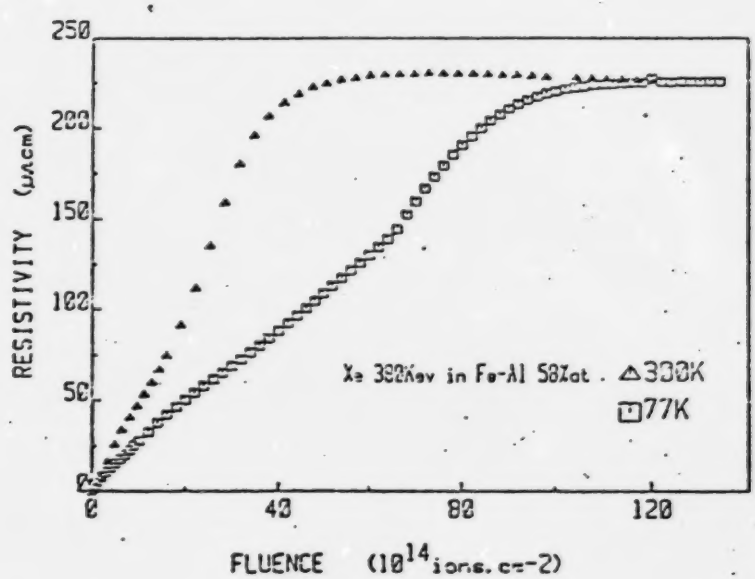

Figure 22. Electrical resistivity increase at 77 K and 300 K during ion mixing of a multilayer for a final composition Fe-58 a% Al (61).

The ion-beam mixing of 100 nm thick bilayers of Al and Fe was studied by Nastassi (62) with RBS and transmission electron diffraction at room and liquid-nitrogen temperatures. Beams of 550 kV Xe were contrasted with pulsed beams of either 280 kV protons or mixed beams of protons, carbon and aluminum at room and liquid nitrogen temperatures. The steady beam had a current of 1 uA/cm^2 while the pulsed beam delivered 16 A/cm^2 during a 100 ns pulse. Xe mixing at 77 K produced little mixing, as shown in Figure 23. Somewhat more mixing was seen when mixing was carried out at room temperature, as shown in Figure 24. The step in the Fe peak of Figure 24 indicates formation of a phase of about 20a% Fe. Neither of Figures 23 or 24 show Fe migration to the surface.

Pulsed-beam irradiations produced fast movement of Fe into the Al layer, as evidenced by Figure 25. The proton beam did not cause as much mixing as the mixed ion beam, even for the same energy input as in Figure 26.

The high-Z Xe beam should produce more cascade mixing by depositing more of its energy into nuclear collisions than either the mixed light ion beam or the proton beam. These last two beams will create many cascades, but will place much of their energy into creation of energetic electrons. The electron -phonon coupling time is longer than the cascade lifetime predicted by these authors, allowing electronic energy to be dispersed over large volumes. In the pulsed beam case, dose rates are so high that the volumes of electron-induced heating overlap and a general temperature rise occurs.

Monte-Carlo heat transfer calculations by these authors show that melting of the surface is possible for the pulsed beams, especially for the less-penetrating mixed beam. Poor heat transfer between the substrate and evaporated films allows long quench times and diffusion of Fe through the Al layer. These data show that mixing by pulsed beams of light ions is more efficient than the cascade mixing of conventionial steady beams.

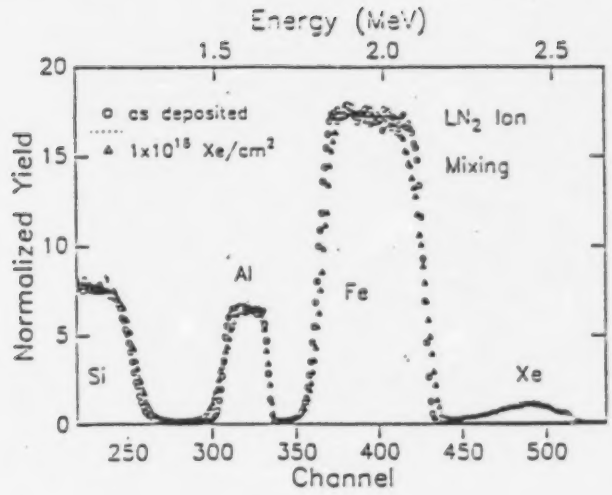

Figure 23. RBS spectra for the mixing of an Fe/Al bilayer at 77 K with $1x10^{16}$ 550 kV Xe/cm^2 (62).

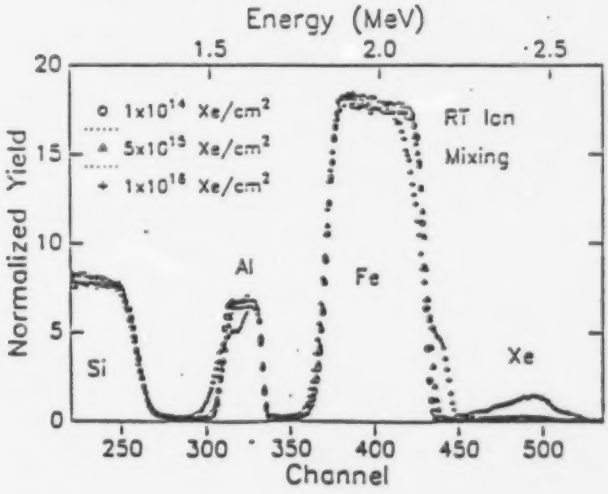

Figure 24. RBS spectra for the mixing of an Fe/Al bilayer at 298 K with various doses of 550 kV Xe (62).

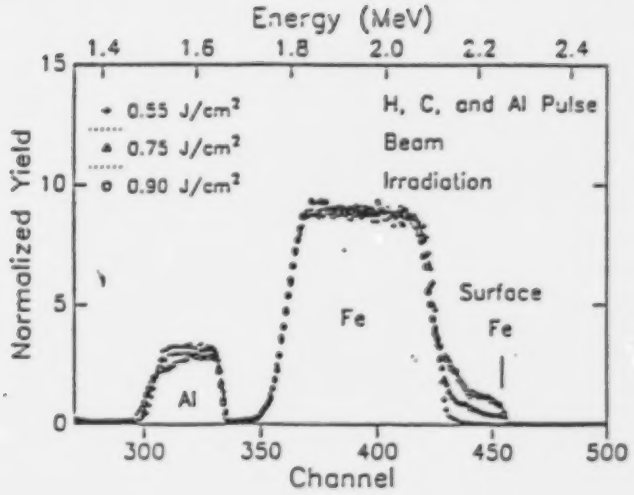

Figure 25. RBS spectra for the mixing of an Fe/Al bilayer with various doses from a pulsed mixed ion beam (62).

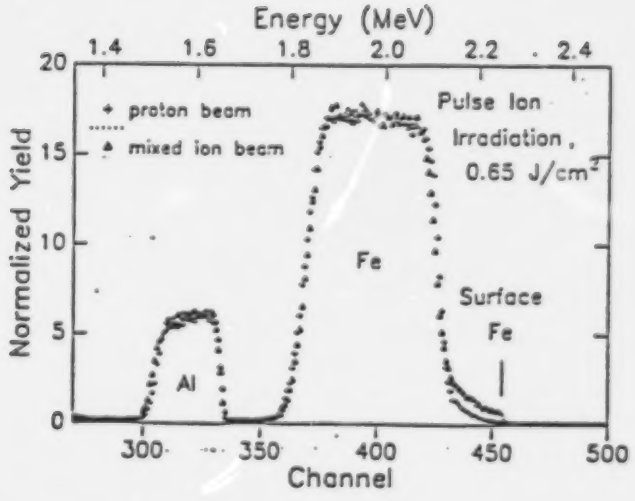

Figure 26. RBS spectra contrasting mixing of Fe/Al bilayer from proton beam and mixed ion beam (62).

2.9 Previous studies in the oxidation of Ion-implanted Fe-Al

Two investigations of Al implantation to improve the oxidation resistance of Fe/Al alloys have been carried out. Pons, Caillet and Galerie (63) investigated the oxidation between 723 K and 1023 K of Al-implanted Fe using glancing XRD and SIMS to follow the process of oxidation and inhibition.

As shown in Figure 28, near-zero rates of weight-gain were observed after an induction period lasting about 1×10^4 s at 1023 K increasing to at least 9×10^4 s at 773 K. Figures 27 and 28 show that a dose of at least 5×10^{16} Al/cm^2 was required for this inhibition, and doses of as much as 1.5×10^{17} Al/cm^2 had no additional benefit. Smaller doses either had no effect or increased the rate of oxidation. At short ($t = 3.5 \times 10^3$ s) oxidation times, Fe_2O_3, Fe_3O_4 and $Fe_2O_3{\cdot}Al_2O_3$ were observed. $Fe_2O_3{\cdot}Al_2O_3$ is thought to be stable at atmospheric pressure only between 1591 and 1768 K (64), with a metastable range perhaps 100 degrees lower (26). Its appearance at 810 K, identified by glancing XRD, is somewhat surprising. Although Fe_2O_3 and Al_2O_3 were observed on the surface after short exposures, the blocking which led to near-zero rates was thought to be caused by formation of hercynite aggregates 1-2 um in diameter. The increased weight gain after small doses was not explained, but could be due either to the Wagner doping effect or to higher diffusion rates in the damaged zone. As a nearly completely blocking hercynite layer is formed after implantation of 5×10^{16} Al/cm^2, any extra implantation and additional hercynite formation can be expected to have little effect, explaining the saturation dose seen in Figure 27. The model for oxidation and inhibition is outlined in Figure 29.

Two general mechanisms of inhibition by implantation have been proposed after an examination of the effects of surface modification by Ni, Bi, B and Al (65). The mechanism seen in the study of Al implantation of Fe is the formation of a blocking double oxide at the scale-alloy interface. This blocking is acheived when the implant species is soluble in the

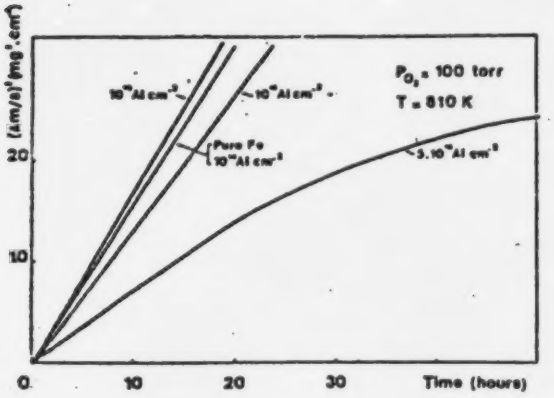

Figure 27. Gravimetric curves (parabolic plot) for oxidation at 810 K of iron specimens implanted at different doses (63).

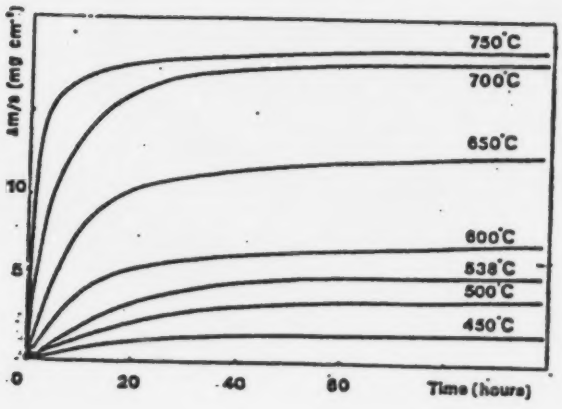

Figure 28. Gravimetric curves (normal plot) for oxidation at different temperatures of iron specimens implanted with 1 x 10^{17} Al/cm^2(63).

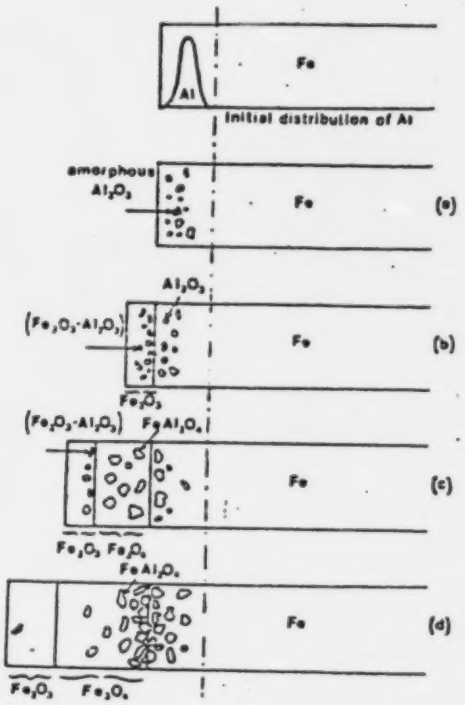

Figure 29. Schematic evolution of the oxidized layer during oxidation at 810 K (63).

matrix and has a greater affinity for oxygen then the host matrix. Implantation of an element insoluble in the matrix can result in blocking of fast-diffusion paths such as grain boundaries, of significant benefit only when the implantation takes place at a temperature at which grain-boundary diffusion predominates.

Bernabai et al (66) investigated implantation of Al into Fe-24.8% Cr-3.1% Al followed by oxidation at 1373 K. A clear dependence of parabolic rate constant on dose is shown in Figure 30, and more alumina in the scale was observed with increased dose. This alloy normally forms a mixture of spinel and alumina when oxidized, so the improvement in kinetics and the increase in the amount of alumina were attributed to the greater availability of aluminum near the surface.

Figure 31 contains the oxidation kinetics of implanted and unimplanted Fe-14.5% Cr-8.2% Al at 1373 K (67), demonstrating no improvement after implantation. This alloy forms alumina immediately and without implantation, so an increase in the amount of aluminium near the surface could not be expected to improve kinetics.

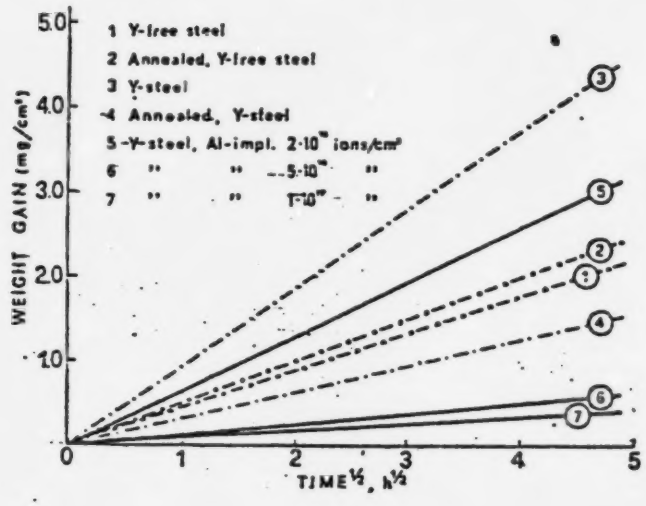

Figure 30. The isothermal oxidation of various steels implanted with Al at several different doses. Oxidation at 1373 K in air plotted as a function of the square root of exposure time (66).

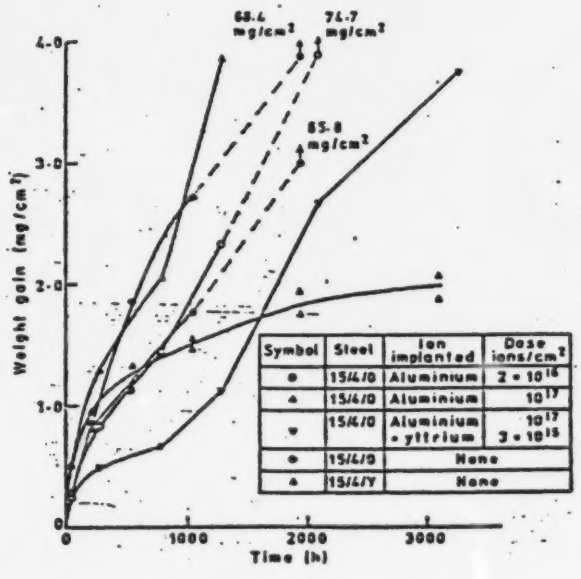
68.4 mg/cm²
74.7 mg/cm²
85.8 mg/cm²
Weight gain (mg/cm²)
Time (h)
Symbol | Steel | Ion implanted | Dose ions/cm²
● | 15/4/0 | Aluminium | 2 • 10¹⁶
▲ | 15/4/0 | Aluminium | 10¹⁷
▼ | 15/4/0 | Aluminium • yttrium | 10¹⁷ 3 • 10¹⁵
● | 15/4/0 | None
▲ | 15/4/Y | None

Figure 31. The effect of surface implantation of Al ions, with and without yttrium ions, upon the variation with time of the extent of oxidation of a Fe-14.5% Cr-8.25 Al stainless steel in air at 1373 K (67).

CHAPTER 3

EXPERIMENTAL TECHNIQUES

3.1 Sample preparation

99.95% electrolytic Fe manufactured by the Research Organic/Inorganic Chemical Company and 99.9995% Al prepared by the A.D. MacKay Corporation were melted under flowing Ar in an electric-arc melting furnace. An assay for the ultra-high purity argon is given in Table 6. Nominal alloy compositions ranged from pure Fe to Fe-10a% Al.

Several cycles of melting and inversion without exposure to air were required to produce a homogenized disk which was then cast into a cylindrical ingot about 10mm in diameter and 55mm in length. This ingot was remelted several times, producing a smooth surface. This rod was next reduced to a diameter of 10mm on a metal lathe, on which it was also polished with SiC papers, finishing with 600 grit paper. Annealing was carried out under a flow of about 7.2×10^{-2} m^3/h of UHP argon for either 7.2×10^4 s at 1173 K or 2.2×10^3 s at 1073 K.

TABLE 6 - Assay for UHP Ar supplied by Canada Liquid Air.

IMPURITY	CONCENTRATION
H_2O	10 PPM <
O_2	10 PPM <
N_2	40 PPM <
H_2	5 PPM <

To better establish any improvement in the kinetics of oxidation on the ion-implanted front and back surfaces, it was decided to minimize oxygen uptake on the edges of

all samples. This was accomplished by dipping the finished rod in molten Al while under Argon in an Arthur D. Little model M.P. crystal growing furnace. An example of the typically rough finish is given in Figure 32(a). In order to establish the exact thickness of the Al-rich layer, EDAX was carried out on the sample of Figure 32(a), the results of which are plotted in Figure 32(b). A layer of Al 100-150 um thick, with some Fe present, has been formed outside a transition layer no more than 100 um thick. There is no sign of deeper penetration of the bar by Al as a result of the dipping process. A smoother more reproducible surface could perhaps be produced by electrochemical deposition of a noble element such as platinum.

Exact alloy compositions could not be reliably established by chemical techniques, but values determined by neutron activation analysis are given in Table 7.

TABLE 7 - Actual alloy compositions.

NOMINAL (a% Al)	EXACT	DEVIATION
2.0	2.14	+7%
3.1	3.26	+5%
4.1	5.46	+33%
5.0	6.62	+32%
9.8	9.90	+1%

Three of the measured compositions are within experimental uncertainty, and the remaining two are 33% high. All determinations are higher than expected, suggesting that not all of the Al layer was removed before analysis.

Disks approximately 1mm thick were cut from the rods using a SiC wheel on a Micro-Mech precision wafer cutting machine. Lubrication and cooling during the cutting was provided by jets of kerosene. Samples were then polished to 600 grit on SiC papers lubricated with water. Final polish was by fabric-covered wheels, impregnated with diamond paste.

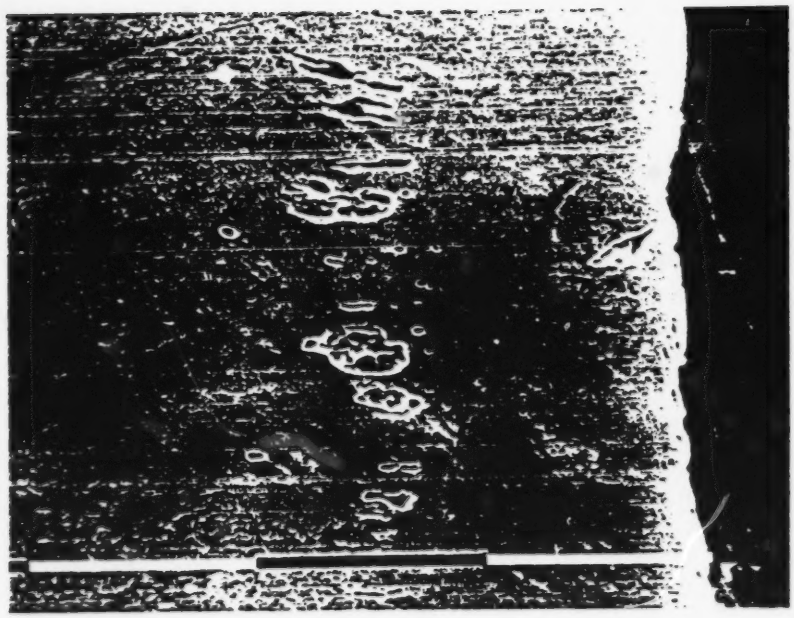

Figure 32. (a) S.E.M. micrograph of Fe-5a% Al sample after dipping in Al. (312X).

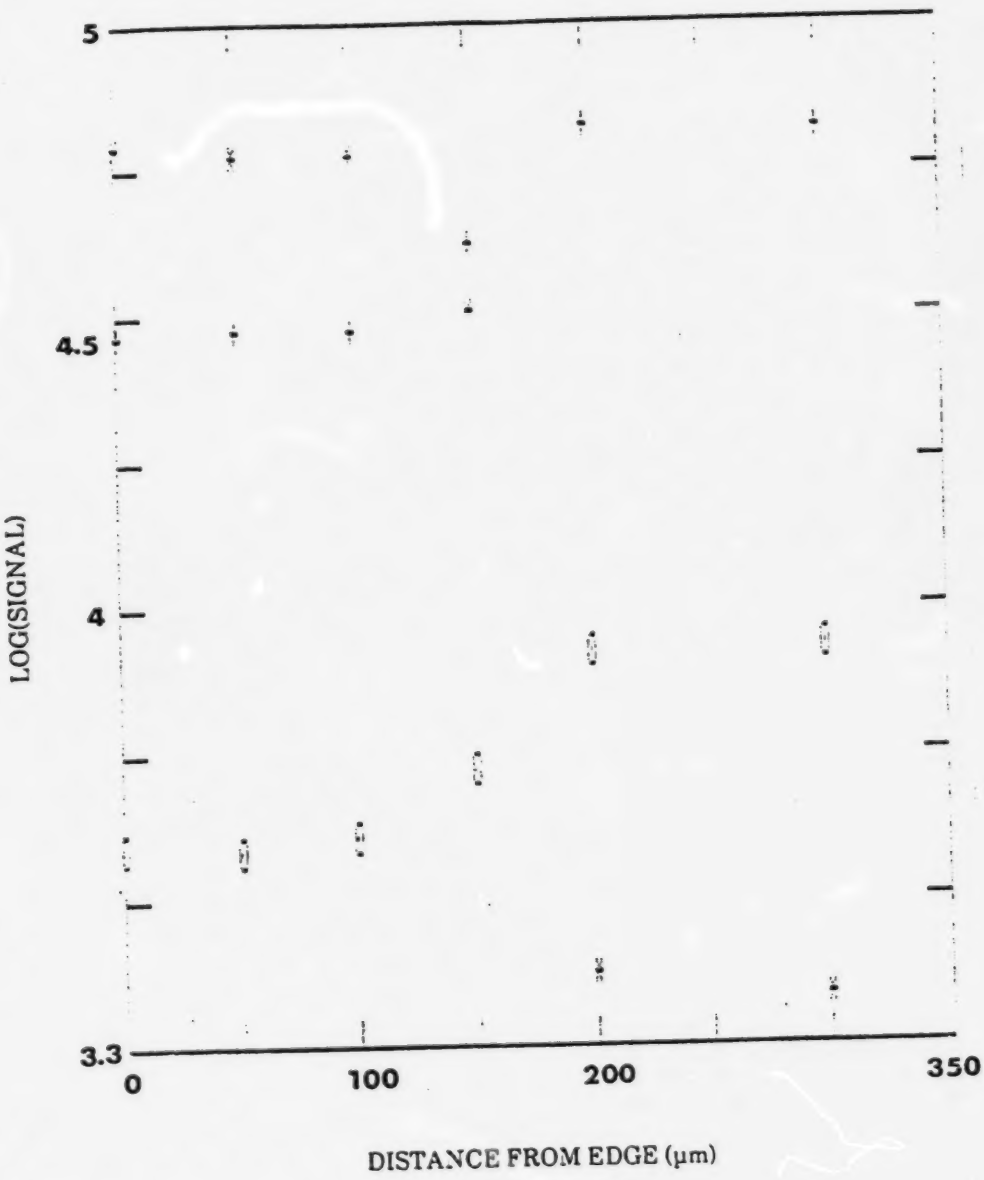

Figure 32. (b) EDAX results from scan of same sample.

• Al $K_{\alpha 1}$ and $K_{\alpha 2}$
+ Fe $K_{\alpha 1}$ and $K_{\alpha 2}$
O Fe $K_{\beta 1}$

After polishing, samples were washed with acetone and ethanol, then stored in a dessicator until needed.

Area determination was made with either a Beuhler Image Analyzer, accurate to within ~1%, or by using a Zeiss optical microscope and a calibrated grid, which had an accuracy of ~5%.

3.2 Implantation

Implantation was carried out using a Wickham Engineering Ion Impantation accelerator, Figure 33, delivering up to 600 uA of mass-analyzed, singly-charged, 100 kV Al ions. Target chamber pressure was 3 x 10^{-4} Pa and a liquid nitrogen trap was used to reduce carbon build-up. Target holder temperature reached 333 K during high dose runs and the sample temperature was estimated as less than 425 K. The beam area was 1.0 x 10^{-3} m^2, allowing simultaneous implantation of three samples and a graphite blank for an independent check on dose by Rutherford Back Scattering (RBS). The results of the independent check are in Table 8.

There are at least two reasons why the doses measured by RBS are higher than expected: ions may have been neutralized by charge-exchange while in the beam line, or the carbon blank used for RBS may have been placed in a region of higher incident ion flux. Samples B12-B15 were implanted simultaneously, and indicate that not only are all doses higher than expected, but there is non-uniformity of as much as 25% from one sample to another.

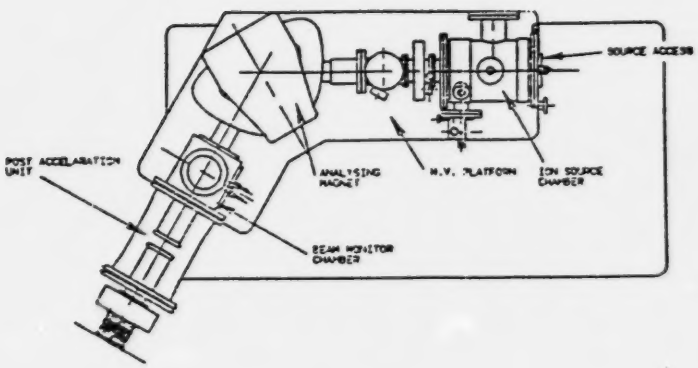

Figure 33. Whickham engineering ion implantation accelerator (71).

TABLE 8 Results of RBS check on implanted doses.

SAMPLE (NOMINAL)	DOSE (MEASURED)	DOSE	DIFFERENCE (%)
B12	1×10^{17}	$1.78 \pm 14 \times 10^{17}$	+ 78
B13	1×10^{17}	$1.32 \pm .06 \times 10^{17}$	+ 32
B14	1×10^{17}	$1.30 \pm .08 \times 10^{17}$	+ 30
B15	1×10^{17}	$1.40 \pm .18 \times 10^{17}$	+ 40
C9	1×10^{17}	$1.50 \pm .08 \times 10^{17}$	+ 50
C13	2×10^{17}	$3.11 \pm .31 \times 10^{17}$	+ 55
D13	2×10^{17}	$5.22 \pm .52 \times 10^{17}$	+ 161
E18	2.4×10^{17}	$3.97 \pm .40 \times 10^{17}$	+ 65
F10	1×10^{16}	$1.21 \pm .12 \times 10^{16}$	+ 21
F11	2.1×10^{17}	$2.98 \pm .30 \times 10^{17}$	+ 42
G7	1×10^{17}	$1.44 \pm .14 \times 10^{17}$	+ 44

Sputter-profiling with the Scanning Auger Microprobe (SAM) was carried out to determine the implanted species and for comparison with the predictions of section 2.6. The profile of Figure 34, which was made after an implantation of 5×10^{17} Al/cm^2 into pure Fe, shows a roughly Gaussian shape, indicative of a low sputtering rate. Low sputtering yield could be attributed to either surface carbon or to a layer of surface oxide, as oxides tend to have low sputtering yields compared to either Fe or Al. Carbon would tend to contaminate the surface of samples during transport to the SAM system, so the low level of carbon seen in Figure 34 indicates either a clean vacuum or removal of surface carbon by sputtering during implantation.

Figure 34 shows unusual Al enrichment near the surface. As Fe is reported to segregate at the surface (68) during ion bombardment of Fe-Al alloys, segregation is an unlikely explanation for this. Recoil implantation would also tend to deplete the surface of Al, the lighter element, rather than the observed enrichment. The most likely explanation for this enrichment and the observed low sputtering yield is the formation of an oxide layer.

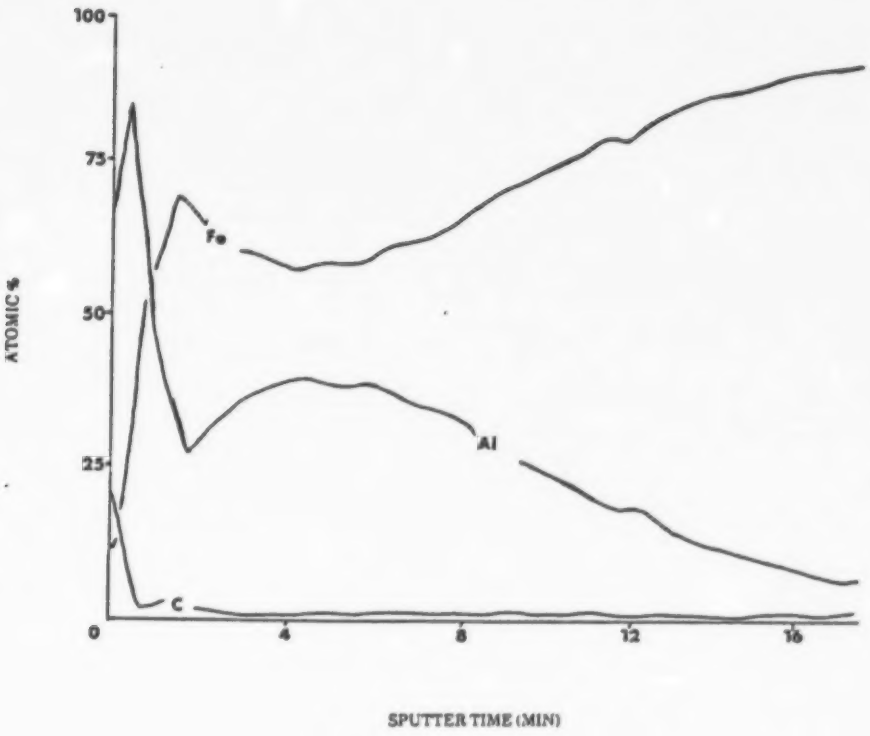

Figure 34. SAM profile after implantation of 7×10^{17} Al/cm^2, converted to atomic %.

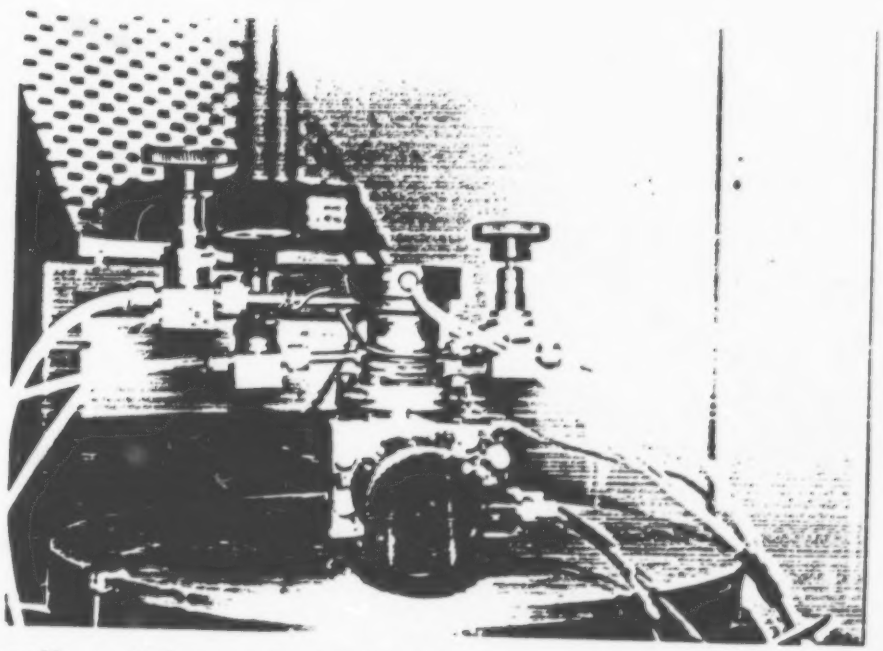

Figure 35. Hydrogen reduction chamber.

The low sputtering yield of Al_2O_3 in particular would make the surface enrichment appear to last over several minutes of sputtering.

A comparison of values observed by SAM and predictions using two different sputtering yields is given in Table 9. Sputtering yields for Al bombardment of Fe or Al were not available, but were approximated by the values for Ar bombardment of the same metals (69), 2.2 sputtered ions/incident ion in each case.

Doses of 5×10^{15} Al/cm^2 were not detectable by the SAM, putting a minimum detection capability for this system of a few a%. Observed peak concentrations are in the range of the predicted values, but the noise level is high enough on SAM profiles that no choice can be made between the two predictive models.

TABLE 9 - Comparison of predicted and observed as-implanted concentrations.

ALLOY	DOSE (/cm^2)	PEAK (Observed)	PREDICTED (51)	PREDICTED (52)
Fe	7.0×10^{15}	-	2.9	1.3
Fe	7.0×10^{16}	16	12.4	11.5
Fe	1.4×10^{17}	21	18.7	20.2
Fe	7.0×10^{17}	4	24.8	30.9
2a%	1.3×10^{17}	21	19.5	19.1
2a%	2.6×10^{17}	18	24.8	29.4
3.1a%	7.1×10^{16}	20	15.5	14.6
3.1a%	1.4×10^{17}	20	21.8	23.3
4.1a%	7.5×10^{16}	16	16.5	16.5
4.1a%	1.5×10^{17}	20	23.9	23.9
5a%	7.1×10^{16}	14	17.4	18.4
5a%	1.9×10^{17}	20	24.1	27.5
9.8a%	7.0×10^{16}	13	22.2	21.3
9.8a%	1.4×10^{17}	24	28.5	30.0

3.3 Thin Film Preparation and Mixing

In order to allow efficient ion beam mixing across the film/alloy interface, the room temperature oxide present on all samples on introduction to the chamber had to be removed (70). To this end, a hydrogen reduction chamber (Figure 35) was constructed and attached to the top of the chamber. Figures 36 and 37 show how sputter-profiling and SAM, as described earlier, was used to find optimal operating conditions for the reduction. Reduction at 823 K for three periods of 900 s, interupted by flushing of hydrogen through the chamber, was found to be successful. Flushing was required to prevent an oxygen equilibrium being reached in the reduction chamber.

After reduction, the reduction chamber was mechanically pumped of hydrogen to a pressure of 2.67 Pa. After this pumping was completed, the valve between the reduction and the main (evaporation) chamber was opened. This caused a large but short-lived rise in the chamber pressure, but no change in the partial pressure of oxygen. Evaporation began as soon as the chamber pressure dropped low enough to allow operation of the electron gun.

The evaporation chamber was diffusion-pumped with a base pressure of 3.0×10^{-9} Pa. A Thermionics triple hearth, 5 kV electron-beam evaporator allowed the sequential evaporation of up to three different materials without exposure of the sample to air. Both thickness and rate of deposition were monitored by an Inficon Crystal Thickness Monitor, the geometric constant of which was calibrated by RBS. Rates of deposition were between .1 and 15 nm/s for Al and Fe, and layer thicknesses ranged from 15 to 100 nm.

Ion beam mixing was carried out with Ar ions of energy between 80 and 140 kV and about 2 uA current, in order to determine the best combination of evaporated film configuration and dose for efficient mixing. When actually preparing samples for oxidation, 100 kV Al ions were used at currents of a few hundred uA. Chamber pressure during Ar

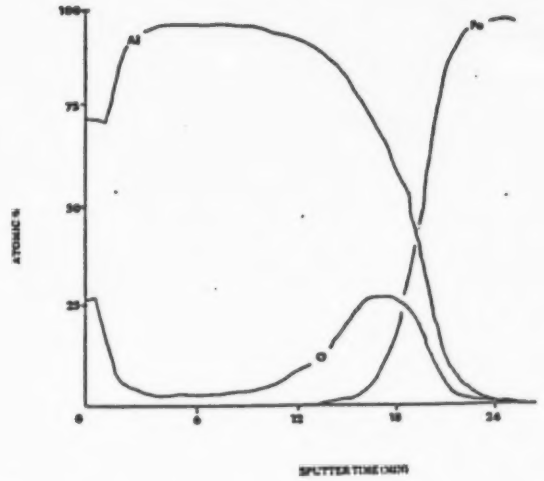

Figure 36. SAM profile of 100 nm of Al on Fe, surface prepared by six periods of 300 s and five periods of 600 s of hydrogen reduction.

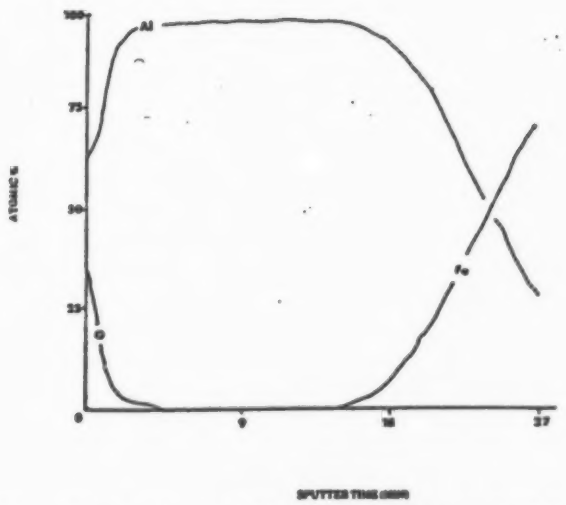

Figure 37. SAM profile of 100 nm of Al on Fe, surface prepared by three periods of 900 s of hydrogen reduction at 773 K.

implantation was between 2 x 10^{-8} to 4 x 10^{-8} Pa and a liquid nitrogen cold trap was used to reduce carbon contamination.

While multiple layer films are thought to speed mixing and development of a flat Al profile, the total thickness of evaporated material is limited by the mean damage range of the incident ion, so that the maximum amount of Al is provided by a single layer of Al on the Fe substrate. The hydrogen reduction system cannot reduce Al oxide, so only films on Fe substrates could be prepared, and the effectiveness of ion-beam mixing on alloy oxidation could not be tested.

Only one set of samples was oxidized after ion-beam mixing of an evaporated Al layer. Figures 38 and 39 show SAM profiles before and after 5 x 10^{16} Al/cm^2. Although oxygen levels are higher than those of Figures 36 and 37, there does not appear to be an oxide layer at the interface, and mixing did take place. Figure 40 is also a SAM profile, of the first side to be evaporated onto, previous to mixing. There has been substantial interdiffusion during the reduction of the other side, which was carried out at 823 K. A "cold" oxide-cleaning system using sputtering of the surface rather than hydrogen reduction could have been used to prepare films on alloys, but was not available. Such a system, operating at room temperature, would also have prevented the inward diffusion of the first evaporated film during the reduction of oxide on the second side.

3.4 Oxidation

Oxidation was carried out using the apparatus of Figure 41, a modified form of that used by Goursat (72). A Cahn RG microbalance was used to continuously monitor sample weight gain, with an uncertainty of 10 ug. The temperature of the inductively wound furnace was controlled by a Thermo-Electric RKC controller to within 1 K of the set point. The temperature profile of the furnace was measured by chromel-alumel thermo-couple to

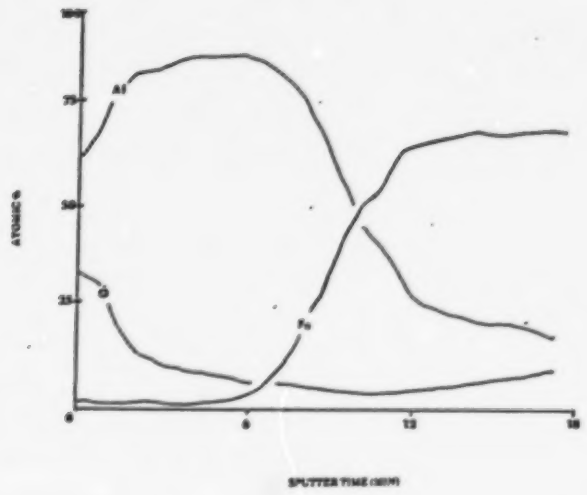

Figure 38. SAM profile of 100 nm of Al on Fe, surface prepared by 3 periods of 900 s at 823 K.

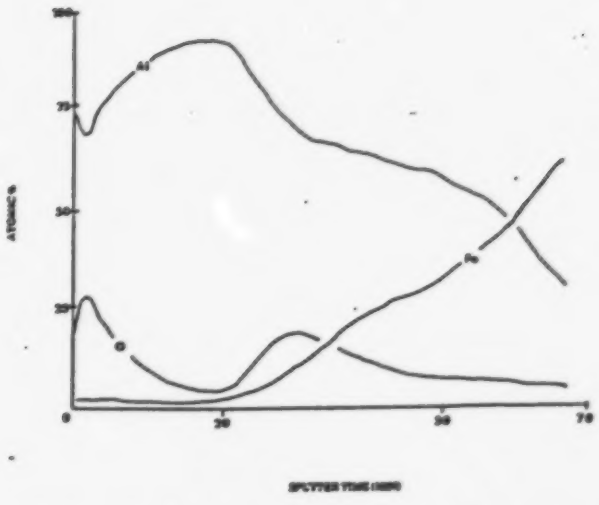

Figure 39. SAM profile of sample of Figure 38 after 5×10^{16} 100kV Al/cm^2.

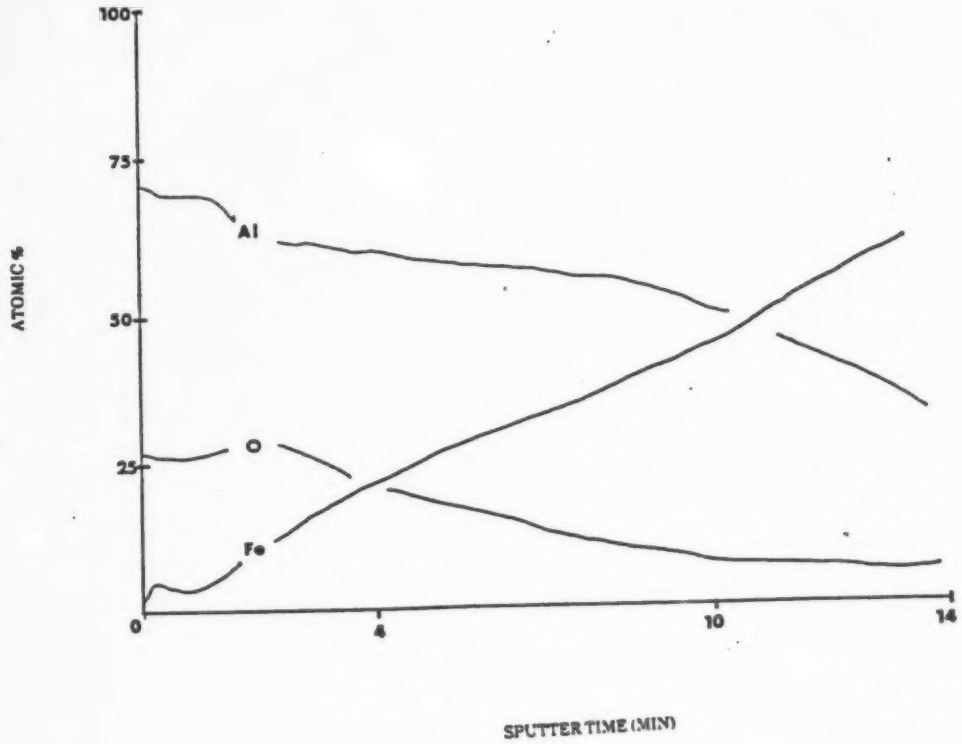

Figure 40. SAM profile of sample of Figure 38, after opposite side has been reduced.

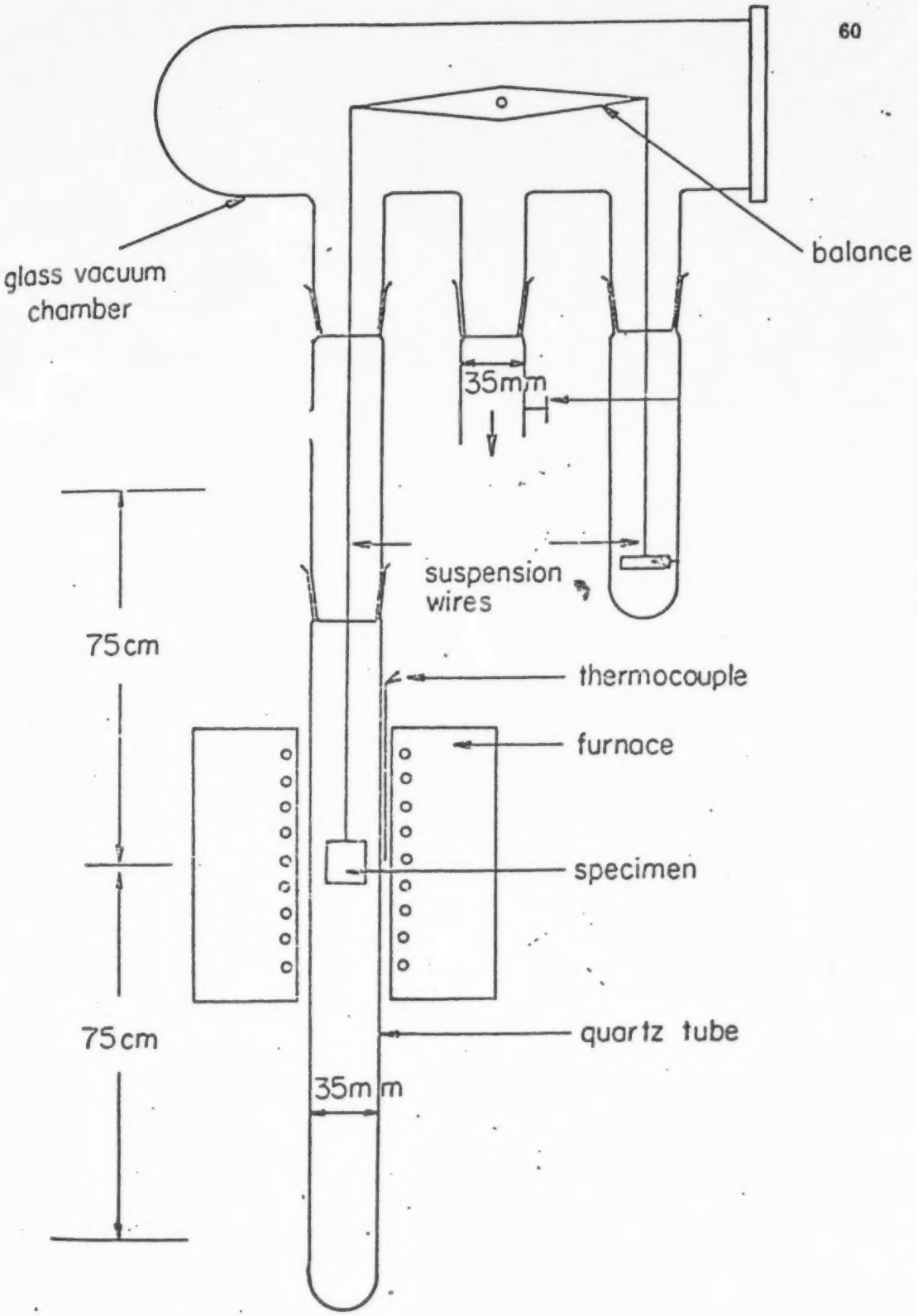

Figure 41. **Oxidation apparatus (72).**

determine the hot zone. Both the controlling thermocouple and the sample were held in this hot zone, which was found to be 20 mm thick. The actual sample temperature for a set point of 1173 K was 1180 K.

The sample was held in a Pt sling attached to a quartz fiber 200 um in diameter. Before beginning an experiment, the apparatus was pumped out by a mechanical pump and backfilled with UHP grade oxygen, the assay for which is in Table 10. This purging procedure was repeated several times before the apparatus was finally filled to a pressure of 26.7 kPa with UHP oxygen, as measured by mercury manometer. Uptake of oxygen by a sample was no more than 75 mg, implying a change in pressure of 2 kPa and a change in the oxygen solubility of less than 4%.

TABLE 10 - Assay for UHP oxygen supplied by Canada Liquid Air.

IMPURITY	CONCENTRATION
ARGON	<30 PPM
CO	<.5 PPM
CO2	<.5 PPM
CH4	<2 PPM
H2	<5 PPM
N2	<50 PPM
H20	<5 PPM

Before starting an experiment, the furnace, in the lowered position, was heated to 15 K hotter than the desired experimental temperature in order to decrease the time required to reach experimental temperature after the drop in temperature due to introduction of the sample. When magnetic, the sample had a force exerted on it by the inductively-wound furnace coil so that the time at which the sample became non-magnetic could be noted. Total

time to reach experimental temperature was no more than 250 s. After oxidation, the furnace was gradually lowered to minimise spalling of the oxide film.

CHAPTER 4

ANALYTICAL TECHNIQUES

4.1 Energy Dispersive X-Ray Analysis

EDAX was carried out using the Kevex detector on the previously described Phillips 515 SEM. The peaks examined are tabulated in Table 11. Samples for EDAX were polished to 50 nm after polishing as described in section 3.1, as resolution can be degraded by topography.

TABLE 11 - Conditions of EDAX analysis.

PEAK ENERGY (keV)	IDENTITY
1.19	AL $K_{\alpha 1}$ and $K_{\alpha 2}$
7.04	FE $K_{\alpha 1}$ and $K_{\alpha 2}$
6.39	FE $K_{\beta 1}$

4.2 Rutherford Back-scattering

Rutherford Back-Scattering was carried out with 2 MeV He ions produced in a Van De Graff generator. Samples were held both normal and at 60° to the beam in a cryo-pumped target chamber. Beam current was 50 nA, and the analysis dose was 6 μC. A silicon surface barrier detector at 160° in the lab coordinate system was used to acquire a profile. Detector dead time was less than 5%. RBS can measure and amount of implanted material as accurately as beam current can be measured. Depth scales are as accurate as tabulated

stopping powers and the energy calibration of the accelerator. Mixing progress is followed with RBS by measuring the increase in variance of the signal corresponding to an evaporated film, or by computer-aided deconvolution. Unfortunately for this investigation, it is difficult to use RBS to study a low-Z material on a heavier substrate, as the signal corresponding to the lighter element appears superimposed on the signal of the heavier element.

4.3 Auger Electron Spectroscopy

A PHI 600 Auger Electron Spectrometer was used for all analyses. The operating settings are listed in Table 12. Sputter rate was determined by raster size and varied from 2x2 mm to 3x3 mm. Table 13 contains sputter rates for pure Al and Fe for the various settings, and were calculated by sputtering of evaporated films which had previously been analyzed by RBS to determine thickness. Depth scales can be determined from these only with some caution, as sputtering rates will vary from pure element rates with concentration.

Atomic concentration was calculated by PHI software which smoothed and differentiated the raw N(E) signal and compared minimum and maximum values in the elemental window to internal standards. As a result of noise, a zero atomic concentration was rarely seen, even in the absence of the element in question.

TABLE 12 - Conditions of AES analysis.

PEAK ENERGY (eV)	WINDOW (eV)	IDENTITY
703	688-708	FE LMM
1396	1372-1402	AL KLL
272	245-275	C KLL
503	495-515	O KLL

ELECTRON BEAM ENERGY 8 kV

SPUTTER ION	Ar
SPUTTER ION ENERGY	5 kV
SPOT SIZE	~1 um

TABLE 13 - Sputter rates for AES profiling.

ELEMENT	RASTER SETTING	RATE OF SPUTTERING
FE	2x2 mm	4.8 nm/min
AL	2x2 mm	3.9 nm/min
FE	2x3 mm	2.3 nm/min
AL	2x3 mm	1.9 nm/min

4.4 Optical Microscopy

For all samples of 4a% Al and less, and for the unimplanted 5a% Al samples, a scale was produced thick enough to allow optical microscopy, using a Zeiss optical microscope. Samples were mounted vertically in cold-setting Epofix resin, cross sectioned, and polished as outlined in 3.1.

4.5 Electron Microscopy

A Phillips 515 Scanning Electron Microscope was used in the secondary electron mode to examine the surface topography of oxides, the undersides of spalled oxides and the structure of internal precipitates revealed after the removal of alloy by a Methanol-10% Bromine solution. To prevent charge build-up, a layer of carbon was evaporated on to all specimens before observation.

4.6 X-Ray Diffraction

X-Ray Powder Diffraction was possible on all samples oxidized at 1173 K, and was used to identify the phases present in spalled oxides. Cu-K_α radiation (λ = .14505 nm) from a 20 mA 30 kV source allowed calculation of d-spacings which were then compared with d-spacings tabulated in the J.C.P.D.S. powder diffraction file (73).

Insufficient oxide existed on specimens oxidized at 873 K for powder diffraction, so reflection X-Ray diffraction was carried out. In all cases, a Phillips X-Ray diffractometer was used.

CHAPTER 5

RESULTS AND DISCUSSION

5.1 Ion-beam mixing experiments

Samples consisting of either 3 or 5 alternating layers of Fe and Al, as shown schematically in Figure 42, were prepared on both C and Fe substrates. Mixing was carried out with Ar or Al ions in the energy range of 80-120 kV. Sample RBS spectra of mixed and unmixed samples are shown in Figure 43 and the corresponding SAM profiles are given in Figures 44 and 45.

The differences between the RBS and SAM techniques discussed in chapter IV are apparent with comparison between Figures 43 and 44 or 45. Broadening of individual peaks in the mixed spectrum of 43 represents mixing, but a more detailed profile is given by SAM. The unmixed SAM profile shows some layer intermixing due to the sputter-profiling ions. This effect increases with depth so that the final Al peak is quite diffuse. Oxide layers on the surface and between the graphite and evaporated films can be seen only on the SAM profile.

Samples consisting of five evaporated films mixed more rapidly than samples consisting of three evaporated films. The total thickness of evaporated films was limited by the mean damage range of the incident ion, so films in the five-layer case were thinner, and faster mixing is to be expected. Although mixing is faster with multilayer samples, the maximum amount of Al enrichment is achieved with a single Al layer. Whether oxidation benefit depends on the absolute amount of Al or on the existence of a well-mixed volume is unknown.

The outermost layer, an Al layer, lost material by the sputtering effect of mixing ions as well as intermixing with deeper layers. The sputtering effect was apparent with SAM

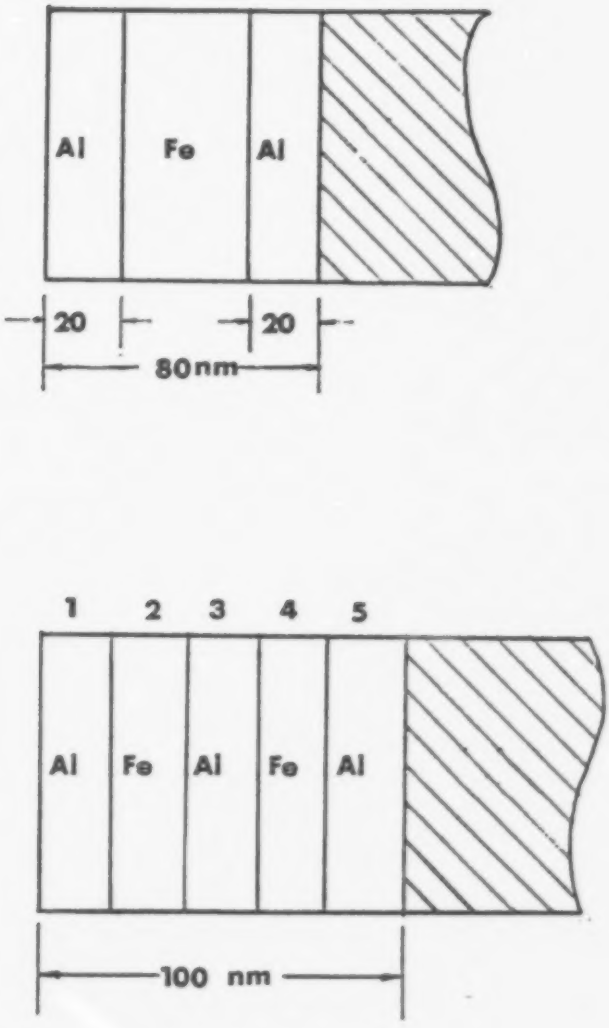

Figure 42. Configurations of evaporated films for ion-beam mixing experiments.

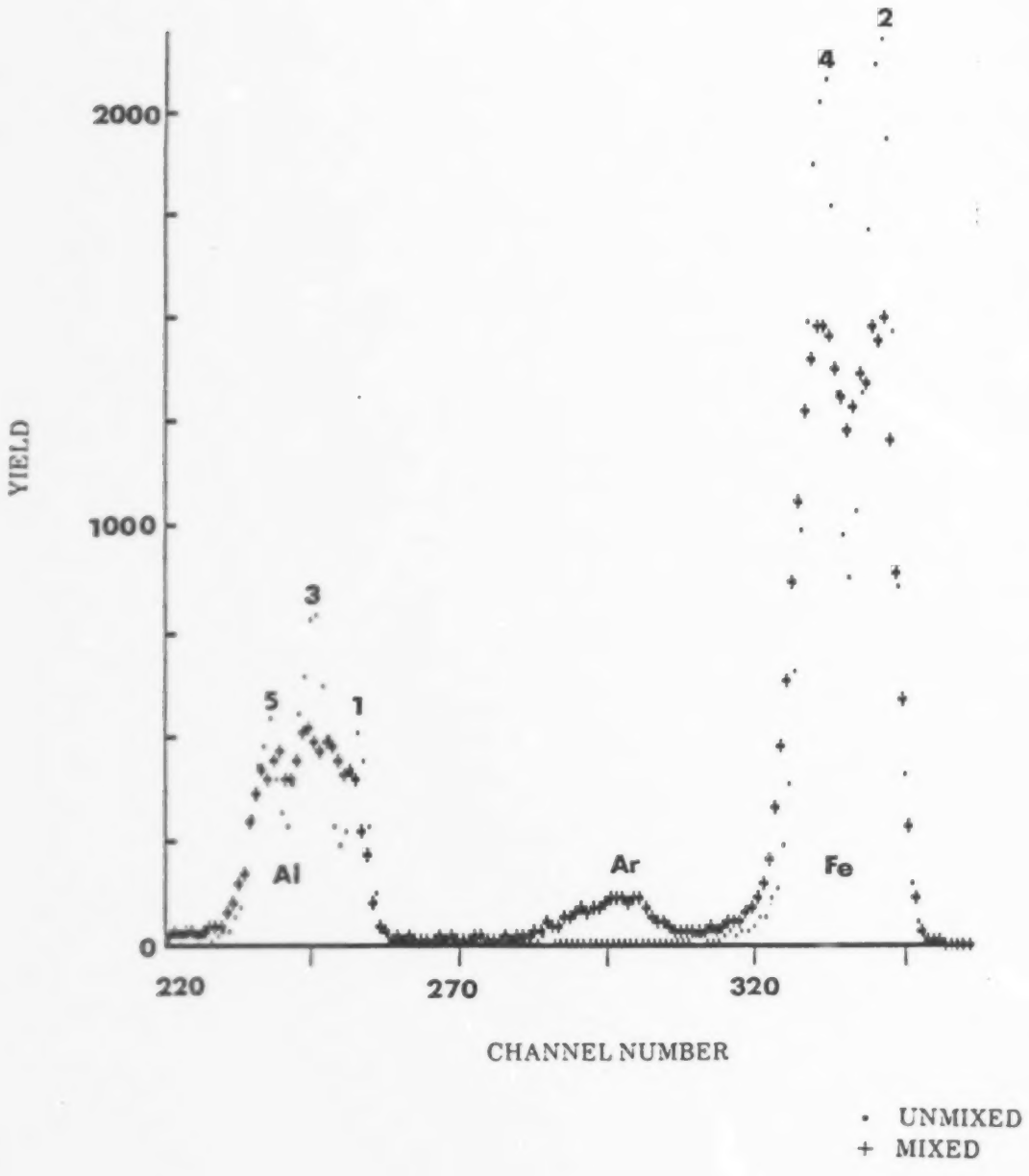

Figure 43. Typical RBS spectra for mixed and unmixed films.

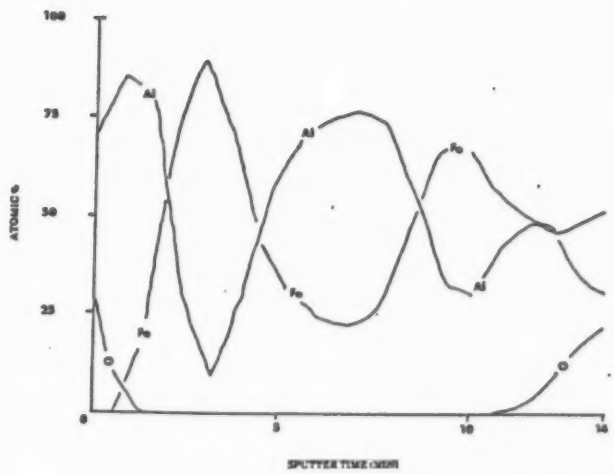

Figure 44. SAM profile of unmixed evaporated films.

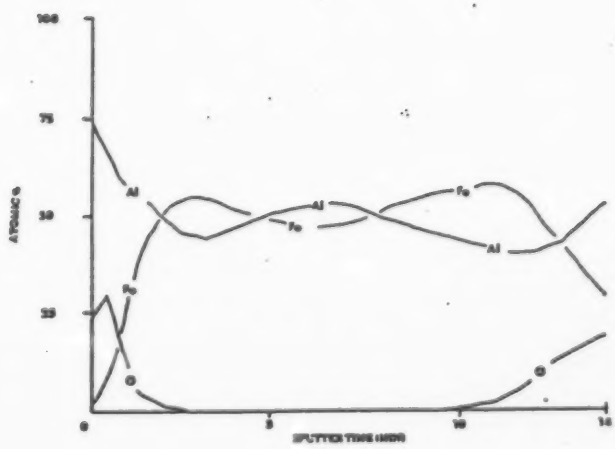

Figure 45. SAM profile of mixed evaporated films.

profiles, particularily of three-layer samples, in that a shorter time was required to sputter through the first layer. The hydrogen reduction process prior to evaporation invariably resulted in an efficient thermal interdiffusion of any evaporated film on the reverse side. The oxidation resistance of each side could not be independently tested, but morphologies were identical.

Evaporating films onto a graphite substrate allowed the use of RBS to follow the progress of mixing, however mixing results differed from those on Fe substrates. Al and C are completely insoluble, so the only mechanism for movement across an Al/C interface is recoil implantation. Since the graphite surface was unreduced, oxygen was present at the film/substrate interface which may have been converted to alumina, which would act as a diffusion barrier. Fe and C are quite soluble, but have an intervening Al layer. As a result, mixed films on graphite (such as Figure 45) have nearly flat concentration profiles. Well-mixed films on Fe substrates, on the other hand, develop Fe profiles which increase monotonically from the surface and Al profiles which tail into the substrate.

5.2 Oxidation experiments

The work of Pons (63) suggests that pure iron can be made oxidation-resistant, even at temperatures as high as 1023 K. Early lack of success with pure Fe at 1173 K in this investigation led to a range of alloys being investigated to determine the minimum alloy enrichment for support of an aluminum-rich film formed, or helped to form, by ion-beam techniques.

a) Pure Fe 873 K P_{o_2} 13.4 kPa

Scales were too thin for either optical metallography or for powder XRD, but reflection XRD showed Fe_3O_4 on both the untreated sample and the sample implanted with 7.1×10^{16} Al/cm^2, with γ-Alumina and Fe_3O_4 on the sample implanted with 1.4×10^{17} Al/cm^2. Even reflection XRD was impossible for the other specimens, due to the extremely thin oxide films formed. Observed line spacings are presented in Table 14.

Table 14 - Line spacings observed from reflection XRD of samples oxidized at 873 K and 13.4 kPa.

SAMPLE	DOSE	OBSERVED D-SPACINGS	IDENTITY
B5	NIL	2.55	Fe_3O_4
		2.54	Fe_3O_4
		1.46	Fe_3O_4
B23	7.1×10^{16}	2.51	Fe_3O_4
		1.45	Fe_3O_4
		1.32	Fe_3O_4
B17	1.4×10^{17}	2.54	Fe_3O_4
		1.94	γ-Al_2O_3
		1.46	Fe_3O_4
		1.45	γ-Al_2O_3

Hematite, magnetite and wustite should have been present on sample B5, but only magnetite was identified. This suggests that thin layers such as hematite and buried layers such as the wustite may not be seen by reflection XRD. γ-Al_2O_3 was detected on the sample implanted with the highest dose, and is a phase not seen or suggested to occur by Pons, but

seen on Fe-20a% Al alloys at this temperature (37). Neither spinel nor $FeAlO_3$ were detected on any specimen, but their presence cannot be ruled out. Many alloys whose protective oxide is spinel below 833 K develop Al_2O_3 above this temperature (39), so perhaps the mechanism of inhibition proposed by Pons is strictly applicable only below 833 K.

Weight-gain kinetics are shown in Figures 46 and 47, and parabolic rate constants with 3σ confidence intervals are given in Table 15. Weight gains were less than parabolic in all cases, and in sample A65 a period of slow growth succeeded faster early growth after t_{12}. All ion-beam modified specimens gained less weight than the control, especially the ion-beam mixed specimen, A52. A52 gained weight at a rate two orders of magnitude lower than the control for the first 1.5×10^4 s, and an order of magnitude lower for the duration of the test.

Table 15 - Parabolic rate constants and confidence estimates for oxidations at 873 K and 13.4 kPa.

SAMPLE	DOSE	K_{p1} (mg^2/cm^4s)	K_{p2} (mg^2/cm^4s)	t_{12}(s)
A65	NIL	$3.12 \pm .37 \times 10^{-4}$	$1.76 \pm .47 \times 10^{-4}$	2.5×10^4
B5	NIL	$2.40 \pm .18 \times 10^{-4}$		
B32	7.1×10^{15}	$1.59 \pm .08 \times 10^{-4}$		
B23	7.1×10^{16}	$2.25 \pm .26 \times 10^{-4}$		
B17	1.4×10^{17}	$1.59 \pm .22 \times 10^{-4}$		
A52	EVAP.	$2.52 \pm 1.8 \times 10^{-6}$	$1.86 \pm .37 \times 10^{-5}$	1.5×10^4

Kinetics of Fe-Al alloys are not available for comparison with the low weight gain observed for the ion-beam mixed sample, but the sigmoidal weight gain observed is typical of pure Al oxidation at these conditions. (75) The work of references 68 and 69 given in Table 16 was done at a lower pressure than this work, but shows that rates comparable to those of the ion beam mixed sample are attributed to Al_2O_3 formation.

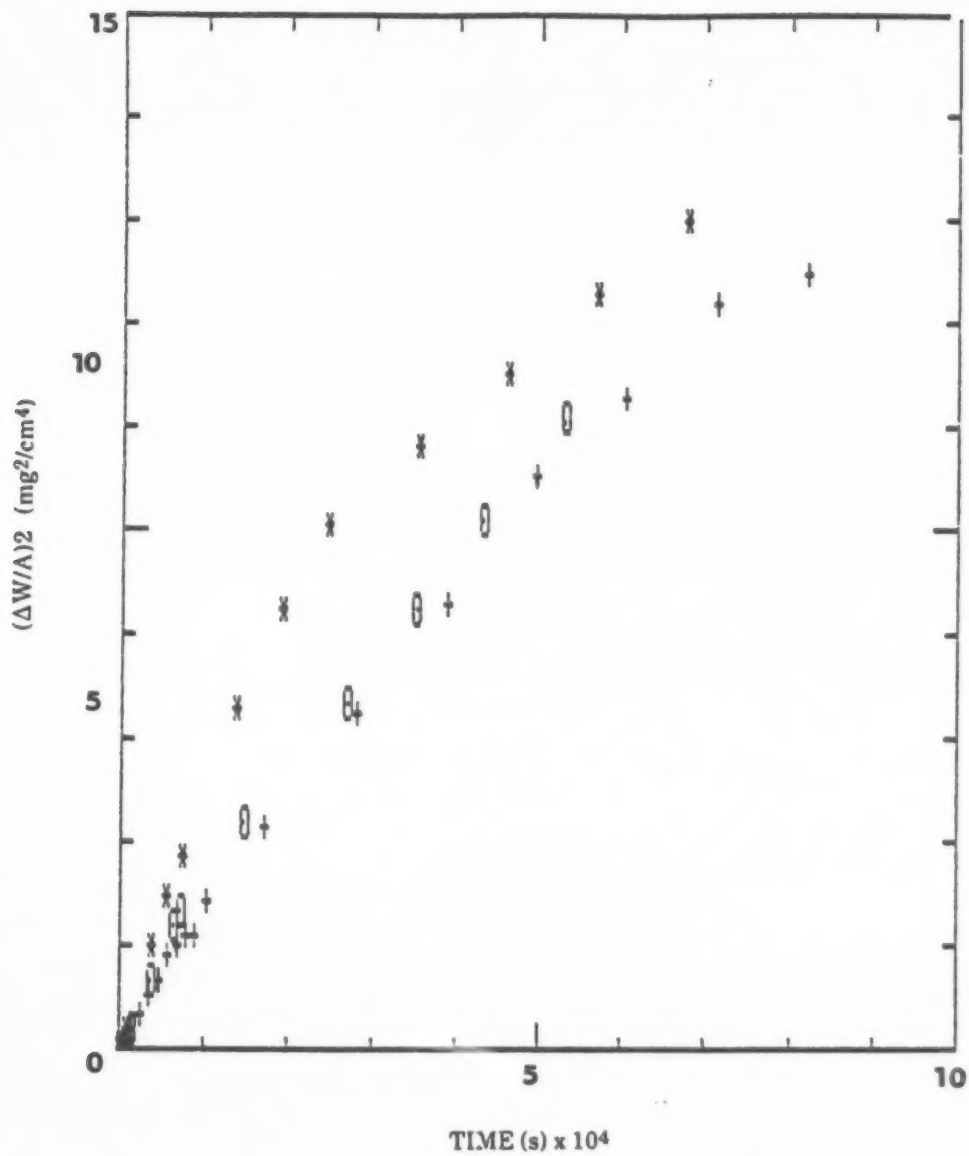

Figure 46. Weight gain of samples oxidized at 873 K, 13.4 kPa.

* - Unimplanted - A65
+ - 7.1 x 10^{15} Al/cm^2 - B32
0 - 7.1 x 10^{16} Al/cm^2 - B23

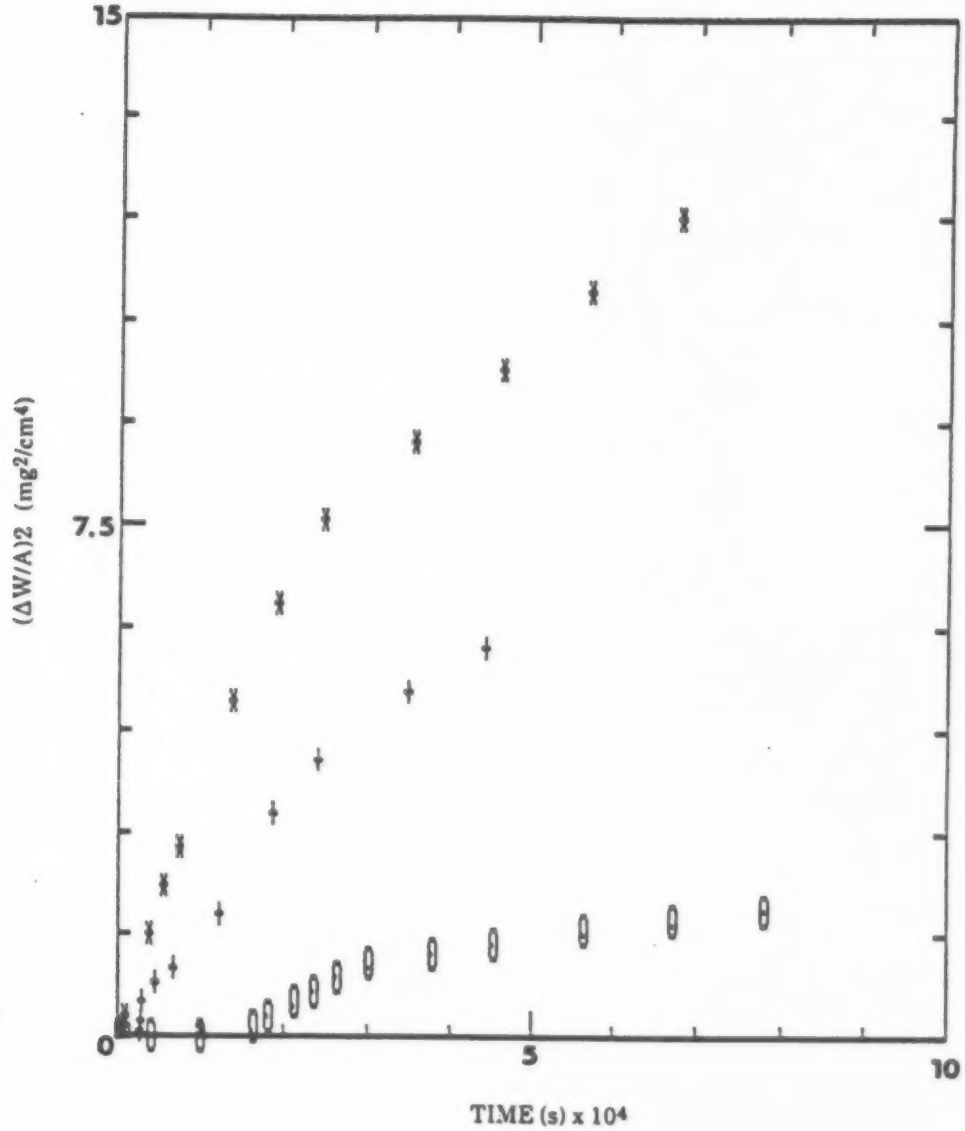

Figure 47. Weight gain of samples oxidized at 873 K, 13.4 kPa.

* - Unimplanted - A65
+ - 1.4 x 10^{17} Al/cm^2 - B17
0 - 100nm Al and 5 x 10^{16} Al/cm^2 -A52

Table 16 - Reported parabolic rate constants at 873 K and 10.1 kPa

K_{p1} (mg^2/cm^4s)	K_{p2} (mg^2/cm^4s)	t_{12} (h)	P (kPa)	source
6.8×10^{-7}	1.1×10^{-6}	1	10.1	(76)
6.0×10^{-7}	9.6×10^{-7}	1	10.1	(76)
8.3×10^{-5}	-	?		(77)

Although no direct identification of the oxide on the ion-beam mixed sample was possible, its slow rate of weight gain suggests that an Al_2O_3 layer, albeit highly defective or perhaps amorphous, may have been formed.

Agreement with the work of Pons can be seen in the results at these conditions. Pons found that a dose of between 1×10^{15} and 1×10^{16} Al/cm^2 was required for an improvement, the lowest dose attempted in this investigation, 7.1×10^{15}, resulted in improvement. Near-zero rates were reported by Pons at 873 K with a sample implanted to 1×10^{17} Al/cm^2 after about 5×10^4 s and a weight gain of 5mg/cm^2. Although the sample implanted here with 1.4×10^{17} Al/cm^2 was perhaps not oxidized long enough to show near-zero rates, its weight gain after 5×10^4 s was 5.5mg/cm^2, within experimental uncertainty of Pons' result.

b) Pure Fe 1173 K P_{O_2} 26.7 kPa

As shown in the micrographs of Figures 48 and 49, representing the ion-beam mixed sample and the sample implanted with 1.4×10^{17} Al/cm^2 respectively, this more aggressive environment produced the triplex morphology characteristic of pure Fe for all samples. A thin whitish layer of Fe_2O_3 above a light gray layer of Fe_3O_4 covers a thick gray layer of FeO, and the ratio of thicknesses is

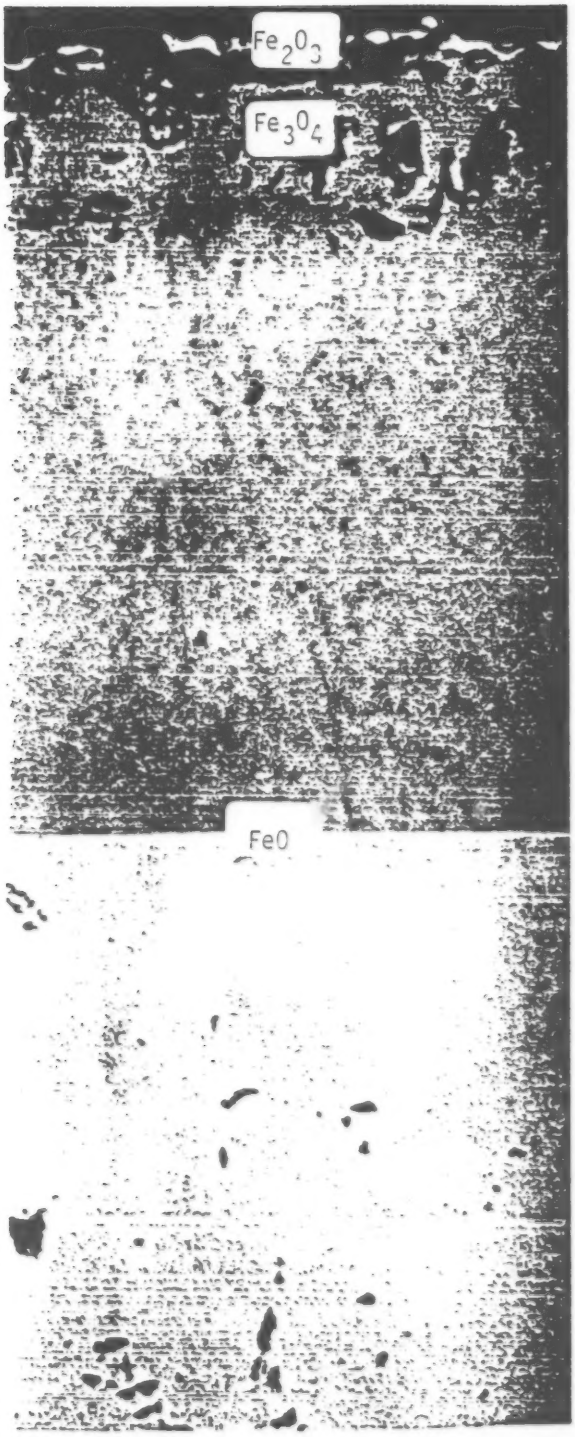

Figure 48. Metallographic cross-section of pure iron sample with **100nm Al mixed by 5 x** 10^{16} Al cm^{-2} after 2.9 x 10^4s at 1173 K and 26.7 kPa (400X).

Figure 49. **Metallographic cross-section of pure iron sample with 1.4×10^{17} Al/cm^2 after 1.4×10^4 s at 1173 K and 26.7 kPa (400X).**

about 1:15:75 for all samples. A network of Fe_3O_4 can be seen in the FeO phase, a result of precipitation during cooling. Weight gain kinetics are shown in Figures 50 and 51, and the calculated parabolic rate constants and 3σ confidence limits are given in Table 17. The largest dose attempted, 7.1×10^{17} Al/cm^2, produced kinetics somewhat slower than those of untreated Fe, but only for the first 2.5×10^3 s, after which its rate of weight gain exceeded that of untreated Fe. No other sample showed kinetics significantly different from the control, and no dose dependence could be found. In all samples the oxide surface had an even gray appearance.

TABLE 17 - Parabolic rate constants and confidence estimates for samples oxidized at 1173 K and 26.7 kPa.

SAMPLE	DOSE	K_{pl} (mg^2/cm^{4}s)
B1	NIL	.144 ± .007
B33	7.1×10^{15}	.185 ± .002
B31	7.1×10^{15}	.148 ± .012
B24	7.1×10^{16}	.142 ± .007
B18	1.4×10^{17}	.177 ± .001
A49	EVAP	.124 ± .006
A54	7.1×10^{17}	.154 ± .019

Figure 28, from Pons, would seem to predict near-zero weight gains after a short period ($t < 3.6 \times 10^4$ s) of fast weight gain. The mechanism advanced by Pons to explain the near-zero rate of weight gain he observed after long exposure was the formation of blocking islands of hercynite below the iron oxides. As shown by Smeltzer and Elrefaie (19), hercynite is partially miscible with magnetite at temperatures as high as 1073 K, but becomes totally miscible by 1173 K, forming a single spinel field as on Figure 8. While hercynite is a good

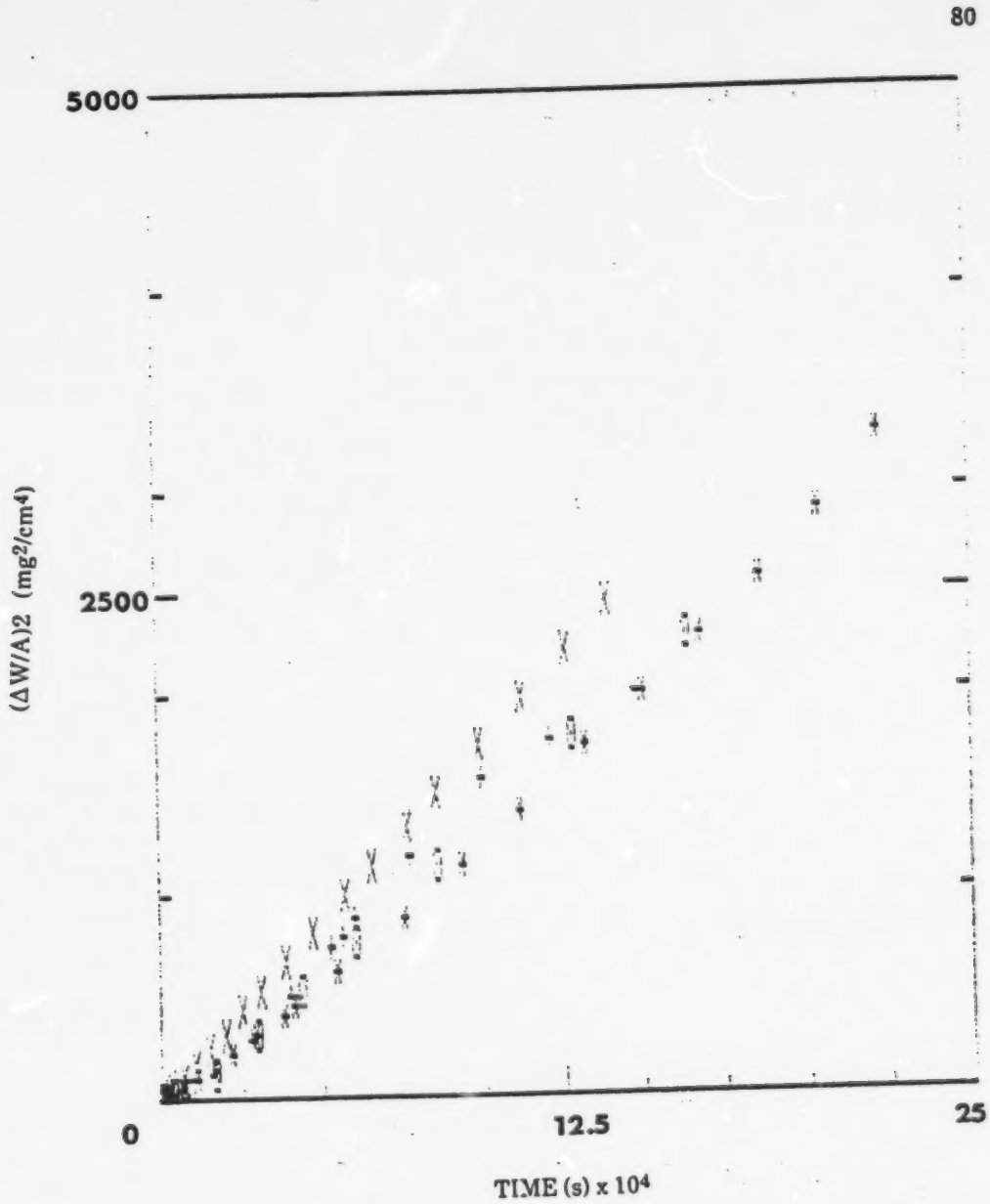

Figure 50. Weight gain kinetics for pure iron samples at 1173 K and 26.7 kPa.

• - Unimplanted - B1
+ - 7.1 x 10^{15} Al/cm2 - B31
0 - 7.1 x 10^{16} Al/cm^2 - B24
x - 1.4 x 10^{17} Al/cm^2 - B18

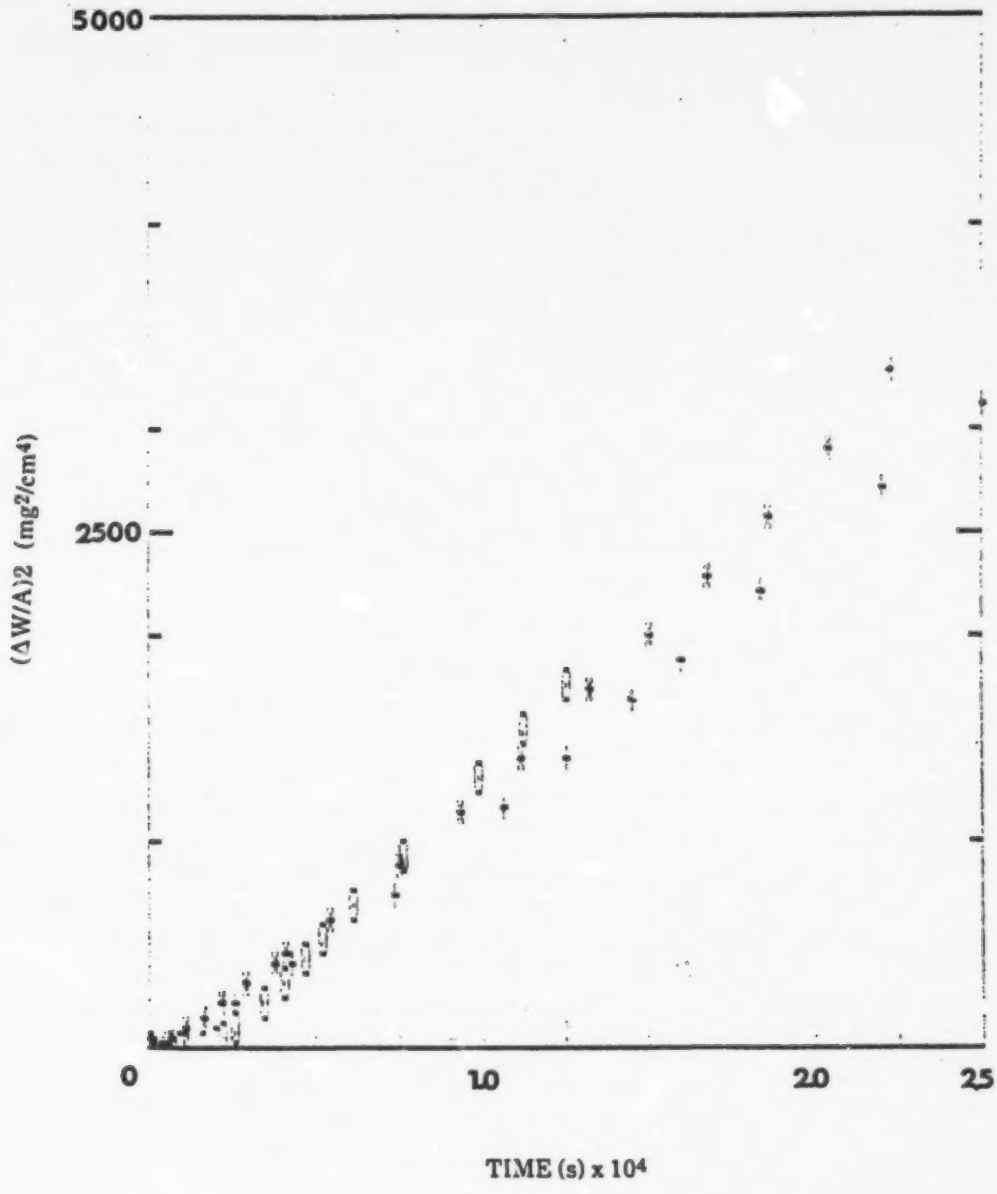

Figure 51. Weight-gain kinetics for pure iron samples at 1173 K and 26.7 kPa.

* - Unimplanted - B1
\+ - 100nm Al and 5 x 10^{16} Al/cm^2 - A49
0 - 7.1 x 10^{17} Al/cm^2 - A54

diffusion barrier, Al-poor spinel is not. If all the Al atoms implanted into the sample of Figure 49 were present in the Fe_3O_4 layer, Al atoms would be outnumbered by Fe atoms 1000 to one. This low concentration cannot provide much of a diffusion barrier, and the kinetics of Figures 50 and 51, very similar to those of pure Fe, are explicable.

The initial rate of weight gain of the sample implanted with 7.1×10^{17} Al/cm^2 was very slow, a weight gain of only 9 mg/cm^2 being recorded after 2.5×10^3 s. This is about an order of magnitude slower than pure Fe rates, but much faster than the rate of alumina-forming alloys. Films produced on Fe-7 or -8a% Al alloys are initially Al_2O_3 (33) on which a surface hematite layer forms by outward diffusion of Fe through short-circuit paths. Such an alloy is capable of healing short-circuit paths by alumina formation below them, but no such healing is possible for pure Fe. Perhaps an Al_2O_3 film forms, but has a large concentration of short-circuit defects. Without healing, the alumina film, would be buried in fast-growing FeO, converted to $FeAl_2O_4$ and perhaps finally dissolved in Fe_3O_4.

c) Fe-2a% Al 1173 K P_{O_2} 101.3 and 26.7 kPa

Optical microscopy revealed no FeO on any specimen of this alloy, but a duplex layer, irregularly attached to the substrate, of Fe_2O_3 on Fe_3O_4. An internal precipitate zone as thick as the duplex scale was identified as spinel + Al_2O_3 as in the earlier work of Ahmed (33). The sample oxidized at 1 atmosphere had a thick, continuous Fe_3O_4 layer which is visible in Figure 52. Samples oxidized at 26.7 kPa produced a thicker layer of Fe_2O_3 with occasional and irregular pieces of Fe_3O_4 near the alloy/scale interface, as Figures 53 and 54 demonstrate. This outer layer frequently spalled off on cooling and allowed powder XRD to confirm the phases present as hematite and magnetite, as shown in Table 18.

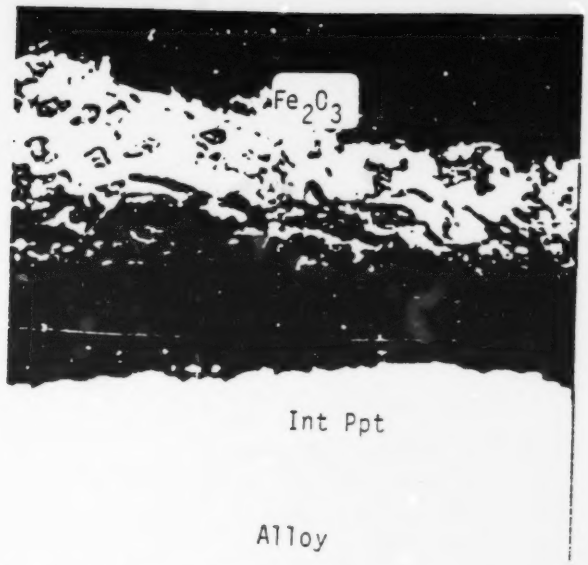

Figure 52. Metallographic cross-section of scale from Fe-2a% Al alloy with 2.6×10^{17} Al/cm^2 after 8.65×10^4 at 1173 K and 101.3 kPa (400X).

Figure 53. Metallographic cross-section of Fe-2a% Al alloy, unimplanted, after 8.3×10^4 s at 1173 K and 26.7 kPa (400X).

Figure 54. Metallographic cross section of Fe-2a% Al alloy with $1 \times 10^{17}/cm^2$ after 2.5×10^4 at 1173 K and 26.7 kPa (400X).

TABLE 18 - Line spacings observed from powder XRD of Fe-2a% Al sample oxidized at 1173 K and 26.7 kPa.

SAMPLE	D-SPACING	IDENTITY
D17	3.71	Fe_2O_3
	2.72	Fe_2O_3
	2.53	Fe_2O_3, Fe_3O_4
	2.22	?
	1.85	Fe_2O_3
	1.70	Fe_2O_3
	1.49	Fe_3O_4, Fe_2O_3

The outer surface of oxides appeared light or dark gray as were the pure Fe specimens, while the underside of spalled oxide was orange with a large black centre. Both the gray and the orange colouring are typical of hematite, while the black layer was identified as magnetite.

The kinetics of weight gain are shown in Figures 55 and 56, and show little difference between implanted and unimplanted specimens. Samples implanted with 1.3 x 10^{16} Al/cm^2 and control specimens had indistinguishable kinetics, while more highly implanted specimens gained somewhat less weight. The control specimen and specimen implanted with 1.3 x 10^{16} Al/cm^2 grew slowly after about 1.0 x 10^4 s, and the corresponding two rate constants are given in Table 19.

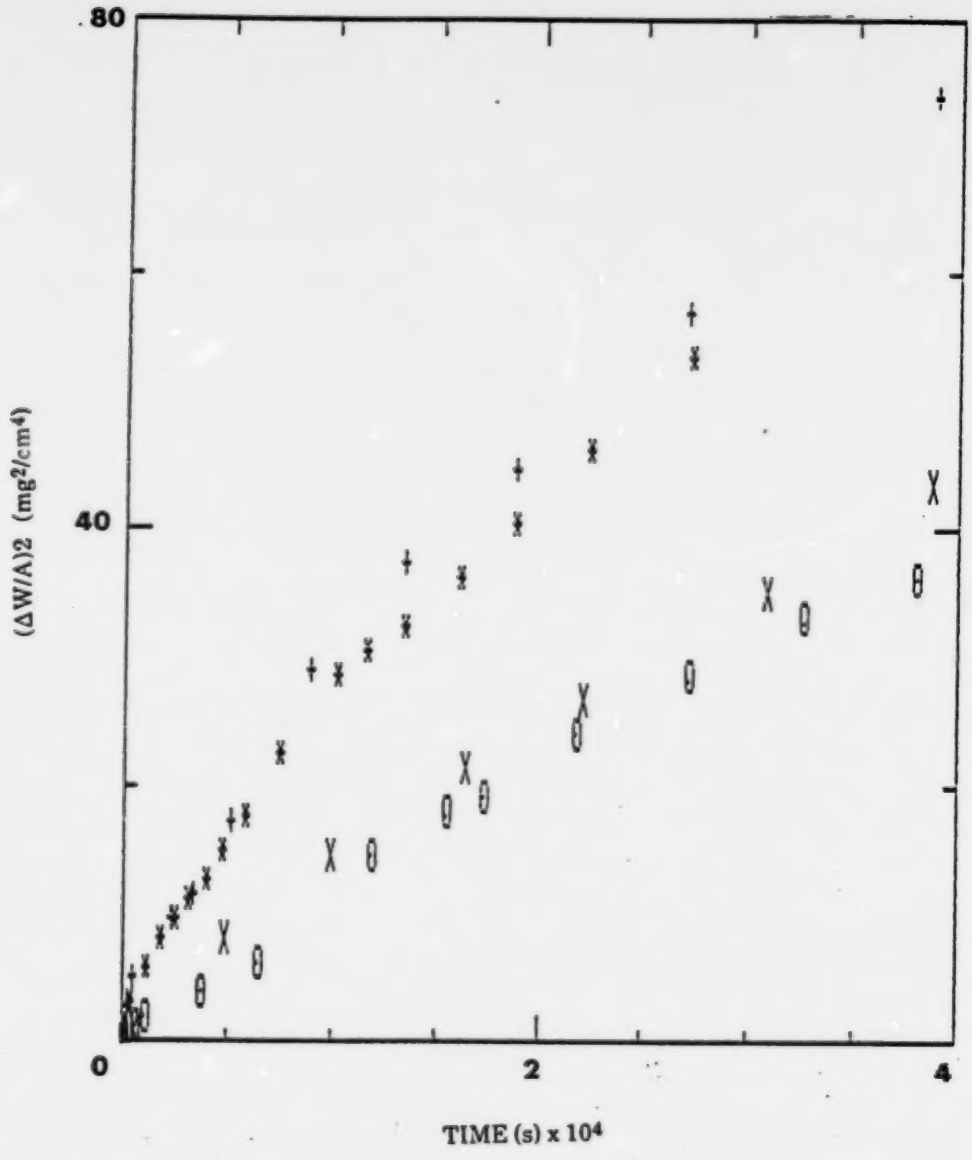

Figure 55. Weight gain kinetics for Fe-2a% Al samples at 1173 K and 26.7 kPa.

* - Unimplanted - D14
X - Unimplanted - D15
0 - 1.3 x 10^{16} Al/cm^2 - D4
\+ - 1.3 x 10^{16} Al/cm^2 - D2

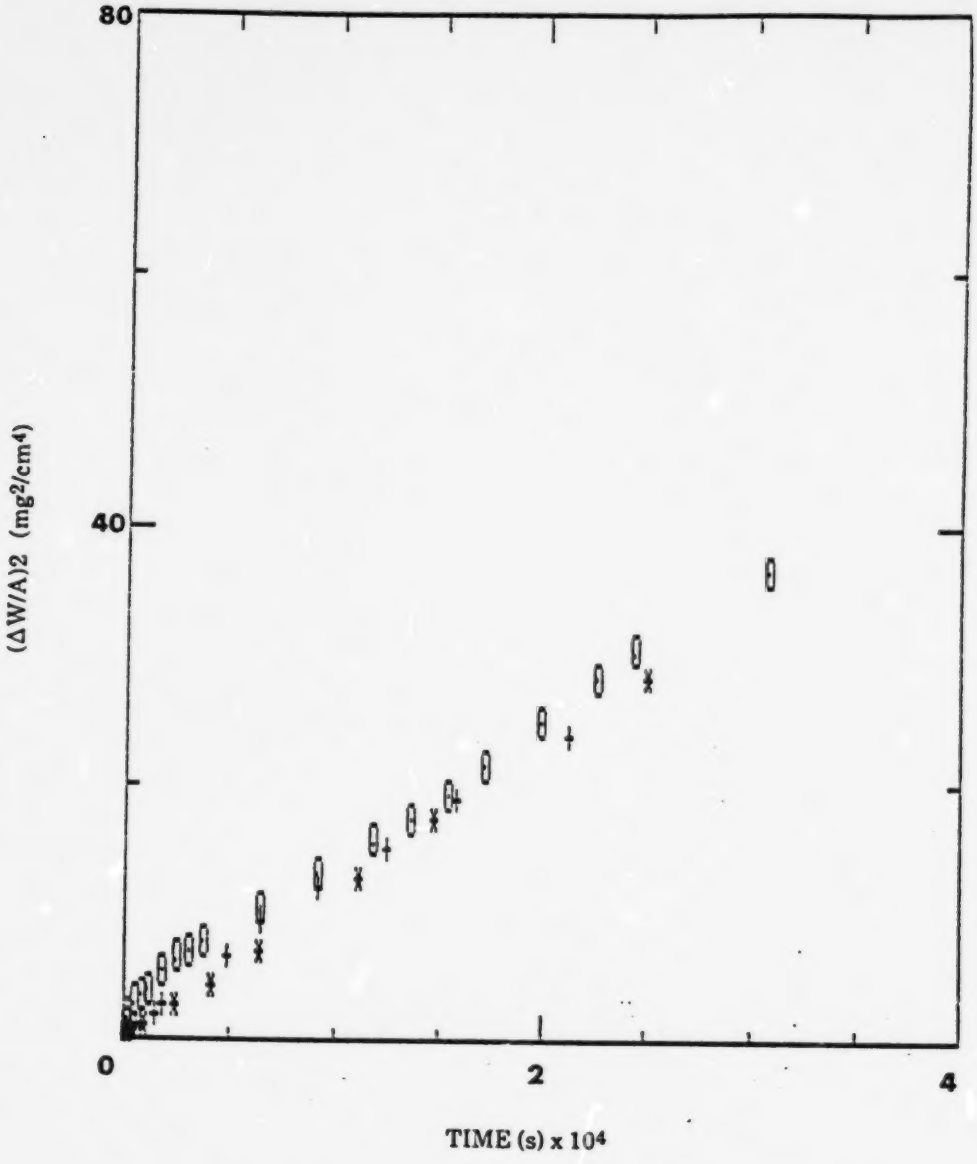

Figure 56. Weight-gain kinetics for Fe-2a% Al samples at 1173 K and 26.7 kPa.

* - 1.3 x 10^{17} Al/cm^2 - D7
0 - 1.3 x 10^{17} Al/cm^2 - D8
+ - 2.6 x 10^{17} Al/cm^2 - D12

Table 19 - Parabolic rate constants and confidence estimates for Fe-2a% Al samples oxidized at 1173 K and 26.7 kPa.

SAMPLE	DOSE	K_{p1} (mg^2/cm^4s)	K_{p2} (mg^2/cm^4s)	t_{12} (s)
D15	NIL	$1.45 \pm .57 \times 10^{-3}$	$1.80 \pm .21 \times 10^{-3}$	1.0×10^4
D14	NIL	$2.80 \pm .35 \times 10^{-3}$	$1.46 \pm .85 \times 10^{-3}$	1.0×10^4
D2	1.3×10^{16}	$3.11 \pm .42 \times 10^{-3}$	$1.45 \pm .045 \times 10^{-3}$	1.0×10^4
D4	1.3×10^{16}	$1.06 \pm .23 \times 10^{-3}$	$7.55 \pm .35 \times 10^{-4}$	1.5×10^4
D7	1.3×10^{17}	$1.13 \pm .04 \times 10^{-3}$		
D8	1.3×10^{17}	$1.10 \pm .03 \times 10^{-3}$		
D12	2.6×10^{17}	$1.154 \pm .10 \times 10^{-3}$		

The faster initial period of oxidation for unimplanted alloys is thought to be a period during which fast Fe_3O_4 growth takes place, and an internal precipitation zone forms. Growth slows when the level of Al in the $(Fe,Al)_3O_4$ layer increases near the scale-metal interface. Hematite appears above the magnetite when Fe diffusion outwards is not sufficient to react with all the adsorbed O at the surface. Later stages see conversion of magnetite to hematite by the reaction

$$2Fe_3O_4 + O \rightleftharpoons 3Fe_2O_3$$

and dissociation of magnetite to provide oxygen for growth of the internal precipitates (33). At this pressure, the transition to slower growth was made after 1×10^4 s rather than 5×10^4 s, although the ratio of K_{p1}/K_{p2} is about the same for this and Ahmed's work. Tomas' investigation, also carried out at this pressure, observed transition times of about 1×10^4 s. Lower oxygen activities and oxidation rates could promote the formation of Al-rich oxides with high oxygen affinities in the subscale, and result in lower transition times.

The absence of two-stage oxidation in samples implanted with 1.3×10^{17} and 2.6×10^{17} Al/cm^2 suggests that the presence of additional, implanted, Al in initially-formed oxide

produces a diffusion barrier, perhaps the same $(Fe,Al)_3O_4$ layer as in unimplanted oxides. That most implanted specimens oxidized at a rate lower than the second-stage of unimplanted specimens suggests that the diffusion barrier may even be a $FeAl_2O_4$ layer under the oxide. Such a layer is sometimes observed (33) under the magnetite layer on an unimplanted specimen.

While implantation resulted in about 20% reduction in weight gain, it produced little if any change in the character of oxide morphology.

d) Fe-3.1 a% Al 1173 K P_{O_2} 26.7 kPa

The morphologies and kinetics of this alloy showed a distinct and interesting dose dependence. Metallography revealed that the morphology of both unimplanted (Figure 57) and 6.1 x 10^{15} Al/cm^2 samples was the same as that of the Fe-2a% Al alloys. The kinetics of these two samples as shown in Figure 58 and rate constants given in Table 20 were similar and much higher than those of samples more heavily implanted. One sample implanted with 7.1 x 10^{16} Al/cm^2 produced a reddish scale overgrown with gray oxide, and the greatest weight gain observed on this alloy, probably a result of a large number of iron oxide nodules coalescing to form the gray scale. The sample implanted with 1.4 x 10^{17} Al/cm^2 (Figure 59) produced a similar reddish scale with several nodules and very low weight gain. The rate constants of this more highly implanted specimen and the sample implanted with 7.1 x 10^{16} Al/cm^2 which did not produce a reddish film were about an order of magnitude lower than those of the unimplanted specimen (Figure 60).

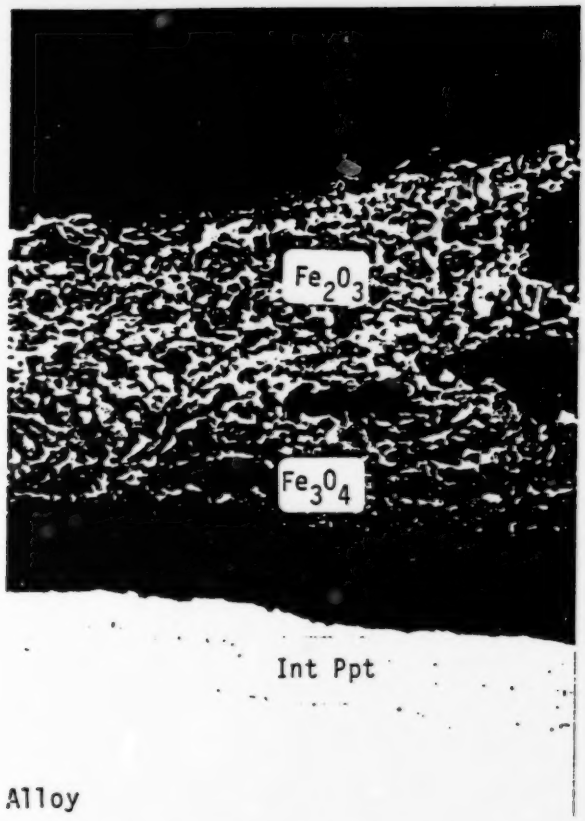

Figure 57. Metallographic cross-section of Fe-3.1a% Al alloy, unimplanted after 8.65 x 10^4 s at 1173K and 26.7 kPa (400X).

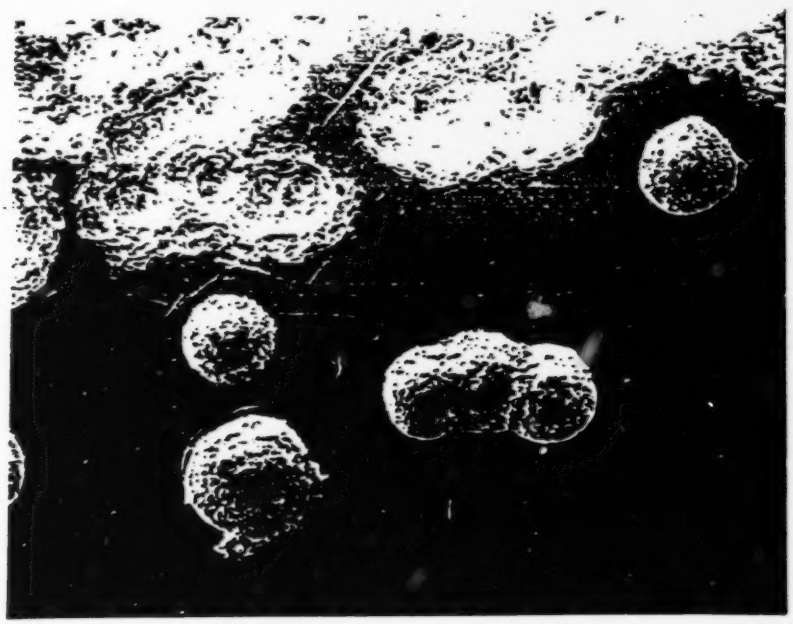

Figure 59. S.E.M. view of Fe-3.1a% Al alloy implanted with 2.6 x 10^{17} Al/cm^2 after 8.65 x 10^4 s at 1173 K and 26.7 kPa (40.8X).

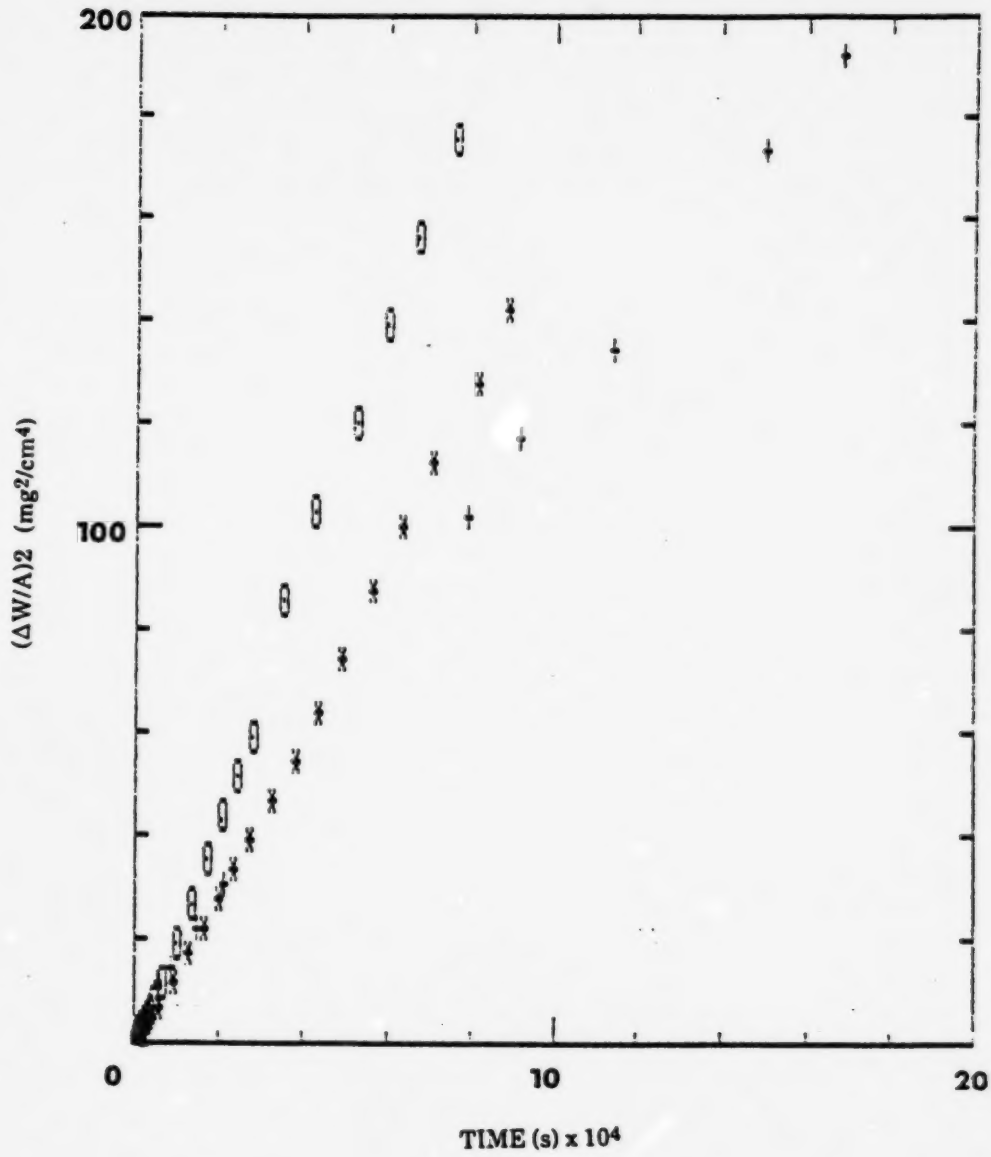

Figure 58. Weight-gain kinetics of Fe-3.1a% Al samples oxidized at 1173K and 26.7 kPa.

* - Unimplanted - F1
0 - Unimplanted - F3
+ - 7.1 x 10^{15} Al/cm^2 - F2

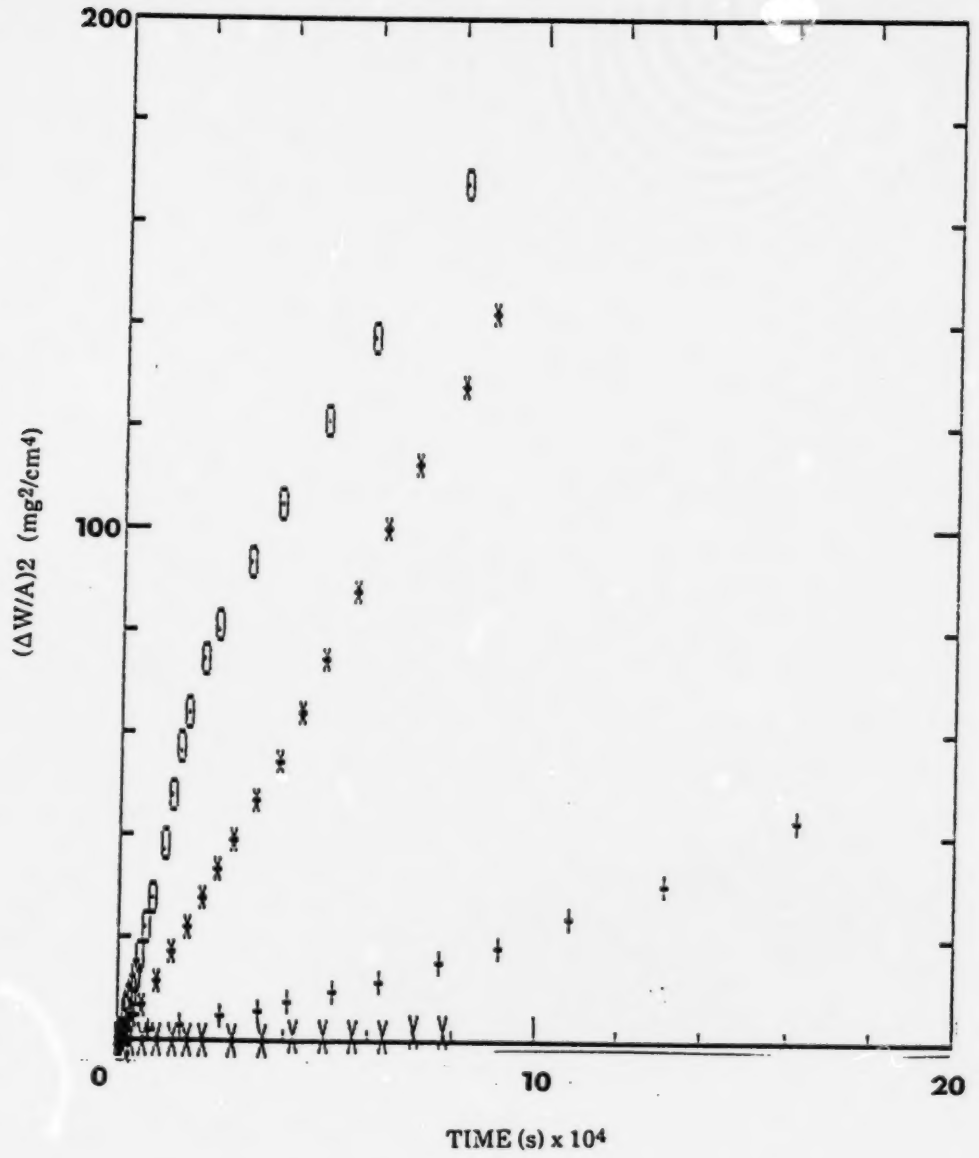

Figure 60. Weight-gain kinetics of Fe-3.1a% Al samples oxidized at 1173K and 26.7 kPa.

* - Unimplanted - F1
\+ - 7.1 x 10^{16} Al/cm^2 - F4
0 - 7.1 x 10^{16} Al/cm^2 - F5
X - 1.4 x 10^{17} Al/cm^2 - F9

TABLE 20 - Parabolic rate constants for Fe-3.1a% Al samples oxidized at 1173 K and 26.7 kPa.

SAMPLE	DOSE	K_{p1} (mg^2/cm^4s)	K_{p2} (mg^2/cm^4s)	t_{12}(s)
F1	NIL	$1.60 \pm .03 \times 10^{-3}$		
F3	NIL	$2.64 \pm .94 \times 10^{-3}$	$1.24 \pm .001 \times 10^{-3}$	3.5E4
F2	7.1×10^{15}	$2.36 \pm .08 \times 10^{-3}$		
F4	7.1×10^{16}	$1.97 \pm .14 \times 10^{-4}$		
F5	7.1×10^{16}	$2.19 \pm .38 \times 10^{-3}$		
F9	1.4×10^{17}	$2.45 \pm .73 \times 10^{-5}$		

The unimplanted and 7.1×10^{15} Al/cm^2 samples had quite similar morphologies and kinetics, both comparable to Fe-2a% results. The most heavily implanted specimen produced a reddish film with a few gray nodules, the morphology seen by Tomas between Fe-3.8 and 13.3a% Al, and in this investigation on Fe-9.8a% Al samples. It is interesting that this duplex morphology was produced with implantation, rather than the triplex morphology formed on unimplanted Fe-5a% Al specimens. An alumina film forms below the internal precipitation zone on such alloys when oxygen diffusion through the $(Fe,Al)_3O_4$ layer is slowed enough as to allow lateral growth of the precipitates (33). Two models could account for this. Either an alumina film forms immediately on this alloy and a hematite film grows on top of it in the same way it does on Fe-7 and 8a% Al alloys in 101 kPa oxygen, or a thin volume of hematite on magnetite above internal precipitate is totally converted to hematite when a layer of alumina forms much earlier than it does on unimplanted Fe-5a% Al alloys.

One side of F5 was a reddish film overgrown with thick gray oxides, one side was a uniform gray oxide. The kinetics of F5 are high because of the contribution of the iron oxide nodules through the duplex film, as explained in section 2.5. The other side of F5 and the other sample implanted to 7.1×10^{16} had very low weight gain even without the formation of

a duplex film, probably because of enhanced blocking in the $(Fe,Al)_3O_4$ layer as in unimplanted specimens. This suggests that for this alloy a dose of 7.1×10^{16} Al/cm^2 is a boundary between two morphologies. Alternatively, alloy inhomogeneity or uncertainty in measuring the implanted dose may have produced two morphologies on the same sample.

e) Fe-4.1a% Al 1173 K P_{O_2} 26.7 kPa and 101 kPa

The unimplanted Fe-4.1a% Al sample oxidized in 26.7 kPa of oxygen produced an outer scale in which no Fe_3O_4 could be observed, and an internal precipitation zone with dark bands running parallel to the alloy surface (Figure 61). The same alloy oxidized in 1 atmosphere of oxygen produced a more adherent scale containing some Fe_3O_4 at the metal/oxide interface as well as patches of internal precipitate (Figure 62). Samples implanted to higher doses and then oxidized at 26.7 kPa had larger amounts of Fe_3O_4, and indistinct bands in the internal precipitate zone can be seen in Figures 63 and 64. The appearance of dark bands in the internal precipitate zone became more pronounced in samples implanted with higher doses. Figures 65 and 66 are SEM micrographs of the internal precipitation zone after etching to remove the alloy. The internal precipitate appears as long rods, with no sign of an alumina layer forming at its tips.

The formation of a duplex film with nodules on only one side of one specimen, C12, suggests that the boundary for the creation of duplex films is 7.5×10^{16}-1.5×10^{17} Al/cm^2 and Fe-3 to 4a% Al, as accurately as alloy content and dose are known. The weight gain of this one sample is quite high, higher than the unimplanted sample due to nodule growth. The upturn in the weight gain of the other 1.5×10^{17} Al/cm^2 specimen suggests nodule growth after an induction period.

Most weight gain kinetics were less than parabolic, suggesting the formation of a blocking layer. One sample implanted with 1.5×10^{17} Al/cm^2 showed only 10% of the

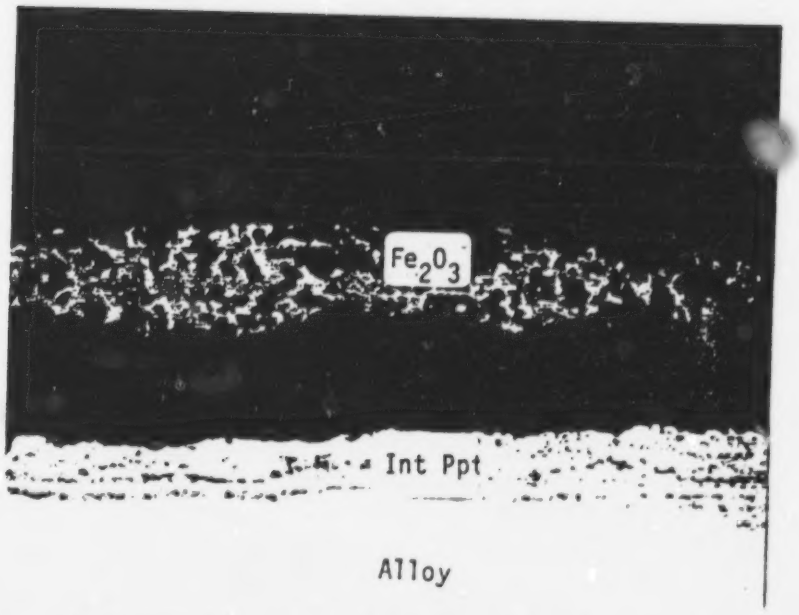

Figure 61. Metallographic cross-section of unimplanted Fe-4.1a% Al sample after 2.5 x 10^4 s at 1173 K, 26.7 kPa (400X).

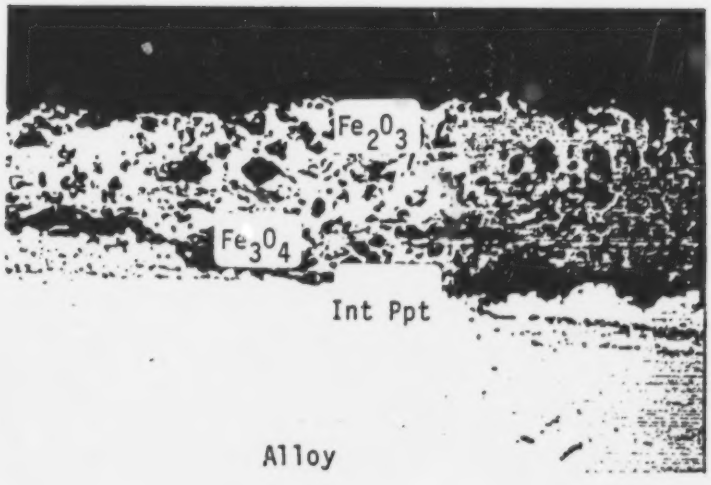

Figure 62. Metallographic cross-section of unimplanted specimen of Fe-4.1a% Al after 8.65 x 10^4 s at 1173 K, 101 kPa (400X).

Figure 63. Metallographic cross-section of Fe-4.1a% Al sample implanted with 7.5×10^{16} Al/cm^2 after 8.65×10^4 s at 1173 K and 101 kPa (400X).

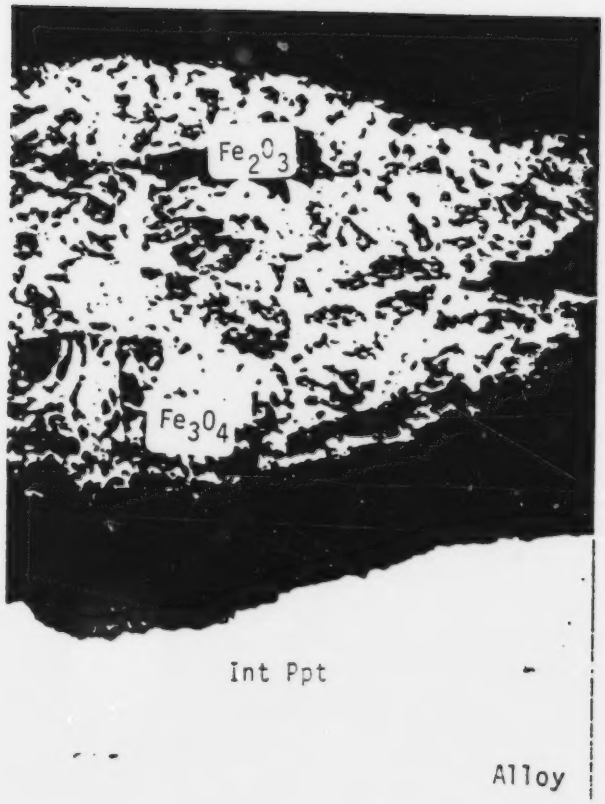

Figure 64. Metallographic cross-section of Fe-4 1a% Al sample implanted with 1.5×10^{17} Al/cm^2 after 7.55×10^4s at 1173 K and 26.7 kPa (400X).

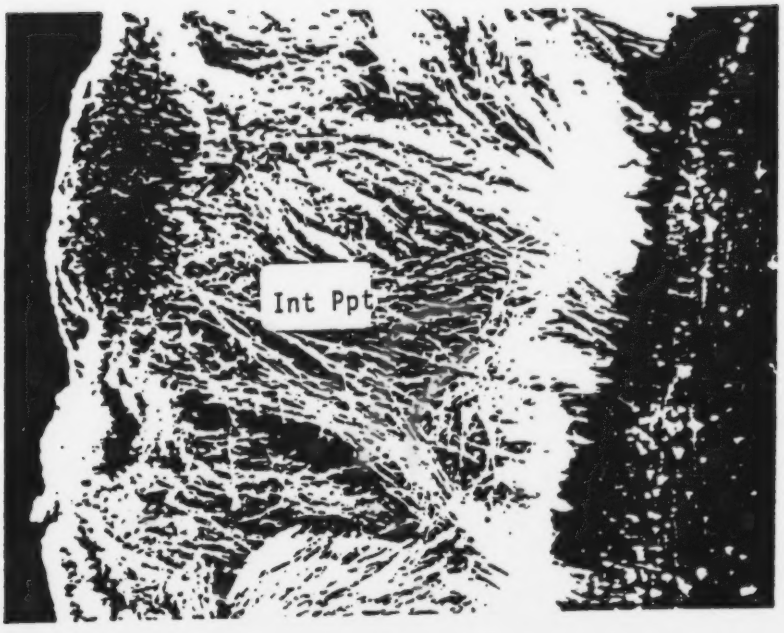

Figure 65. S.E.M. view of internal precipitates after etching. Sample is Fe-4.1a% Al implanted with 1.5 x 10^{17} Al/cm2 after 2.15 x 10^{4} s at 1173 K and 26.7 kPa (965X).

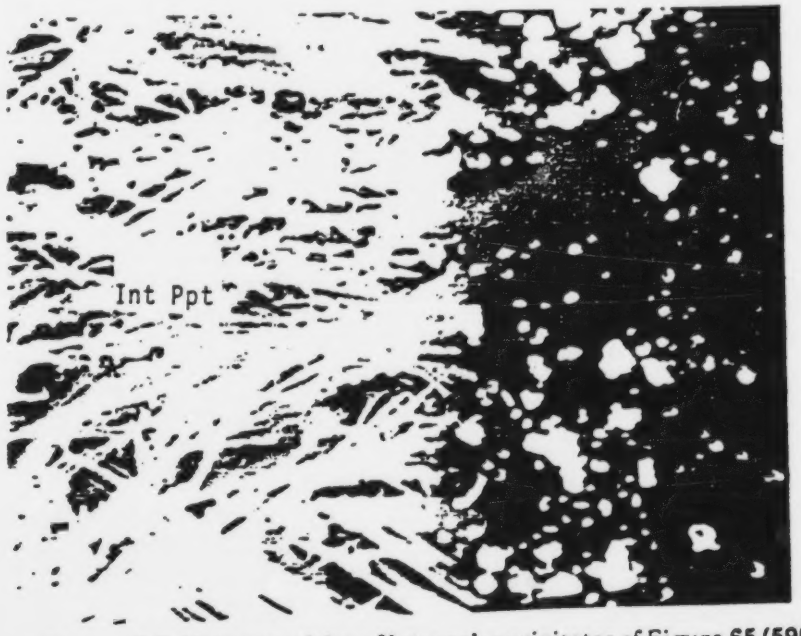

Figure 66. S.E.M. image of tips of internal precipitates of Figure 65 (5950X).

unimplanted weight gain, although its morphology was similar to the control sample's. The other sample implanted with 1.5×10^{17} Al/cm^2 displayed a reddish film with gray nodules and weight gain somewhat higher than that of the control. The samples implanted with 7.5×10^{15} and 7.5×10^{16} Al/cm^2 showed weight gain somewhat less than the control and much the same morphology. Kinetics are presented in Figures 67 and 68, and the parabolic rate constants in Table 21. Note the large uncertainties associated with these, and the two regimes of most samples.

TABLE 21 - Parabolic rate constants and estimated confidence intervals for Fe-4.1a% Al samples oxidized at 1173 K and 26.7 kPa.

SAMPLE	DOSE	K_{p1} (mg^2/cm^{4}s)	K_{p2} (mg^2/cm^{4}s)	t_{12}(s)
C14	NIL	$1.09 \pm .68 \times 10^{-3}$	$4.09 \pm .20 \times 10^{-4}$	5.0×10^3
C4	7.5×10^{15}	$4.63 \pm .25 \times 10^{-4}$	$1.44 \pm .06 \times 10^{-4}$	5.0×10^3
C2	7.5×10^{15}	$4.30 \pm 1.2 \times 10^{-4}$	$1.28 \pm .25 \times 10^{-4}$	5.0×10^3
C8	7.5×10^{16}	$4.93 \pm .09 \times 10^{-4}$	$1.88 \pm .004 \times 10^{-4}$	1.0×10^4
C11	1.5×10^{17}	$1.05 \pm .01 \times 10^{-4}$	$2.53 \pm .11 \times 10^{-4}$	5.0×10^4
C12	1.5×10^{17}	$1.24 \pm .27 \times 10^{-3}$		

◊ Fe-5a% Al 1173 K P_{o_2} 26.7 kPa

Only the unimplanted specimen produced a scale thick enough for the optical micrograph of Figure 69. Metallography revealed a thick oxide layer with irregular internal oxidation over a thin black layer of Al_2O_3. Morphology of all implanted specimens was similar: a thin reddish scale, overgrown to some degree by gray oxide nodules. As demonstrated in the SEM micrographs of Figures 70 to 72, the reddish scale is often quite convoluted and cracked. The long-time results in Figure 73 indicate sudden breakdown of the

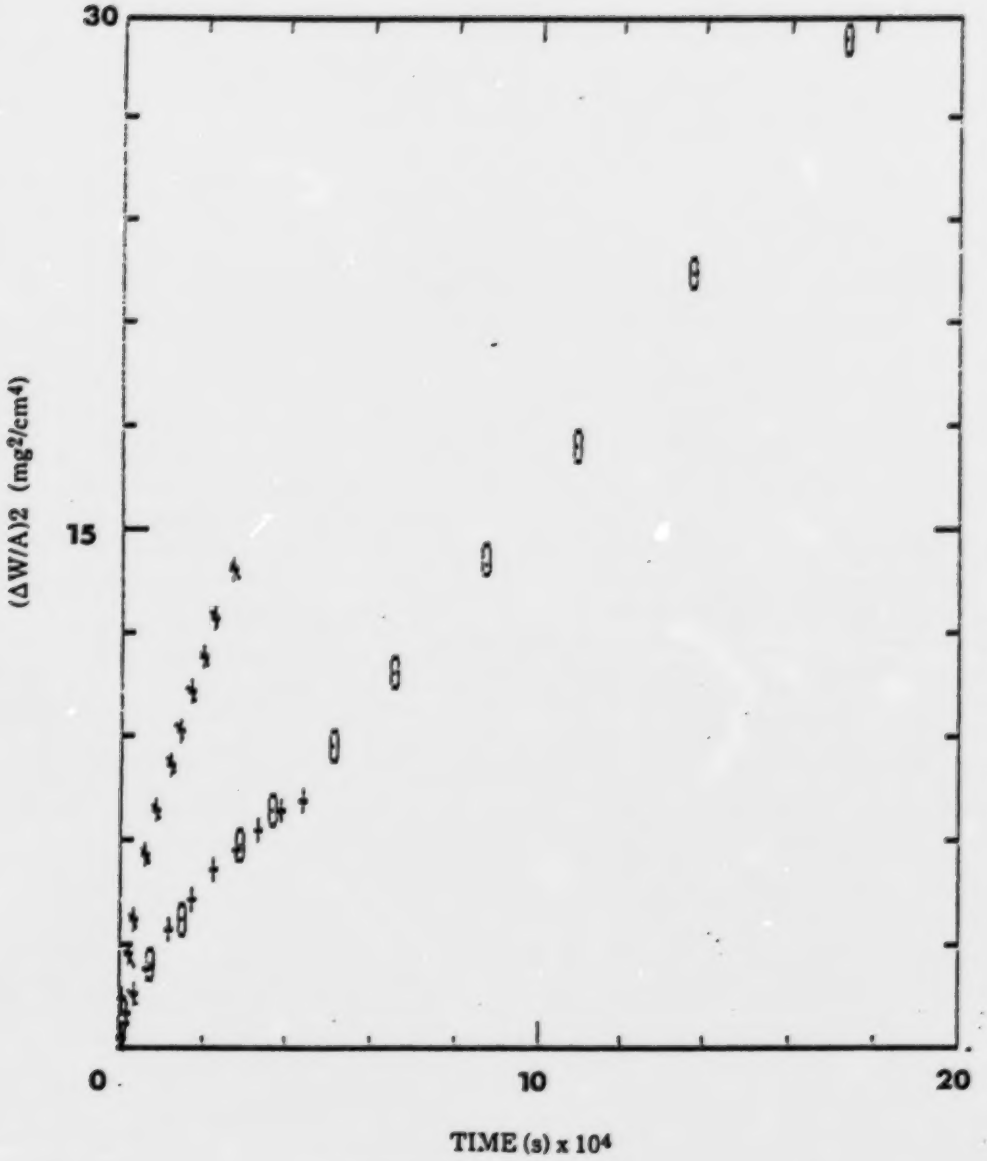

Figure 67. Weight-gain kinetics of Fe-4.1a% Al samples oxidized at 1173 K and 26.7 kPa.

* - Unimplanted - C14
+ - 7.5 x 10^{15} Al/cm^2 - C2
0 - 7.5 x 10^{15} Al/cm^2 - C4

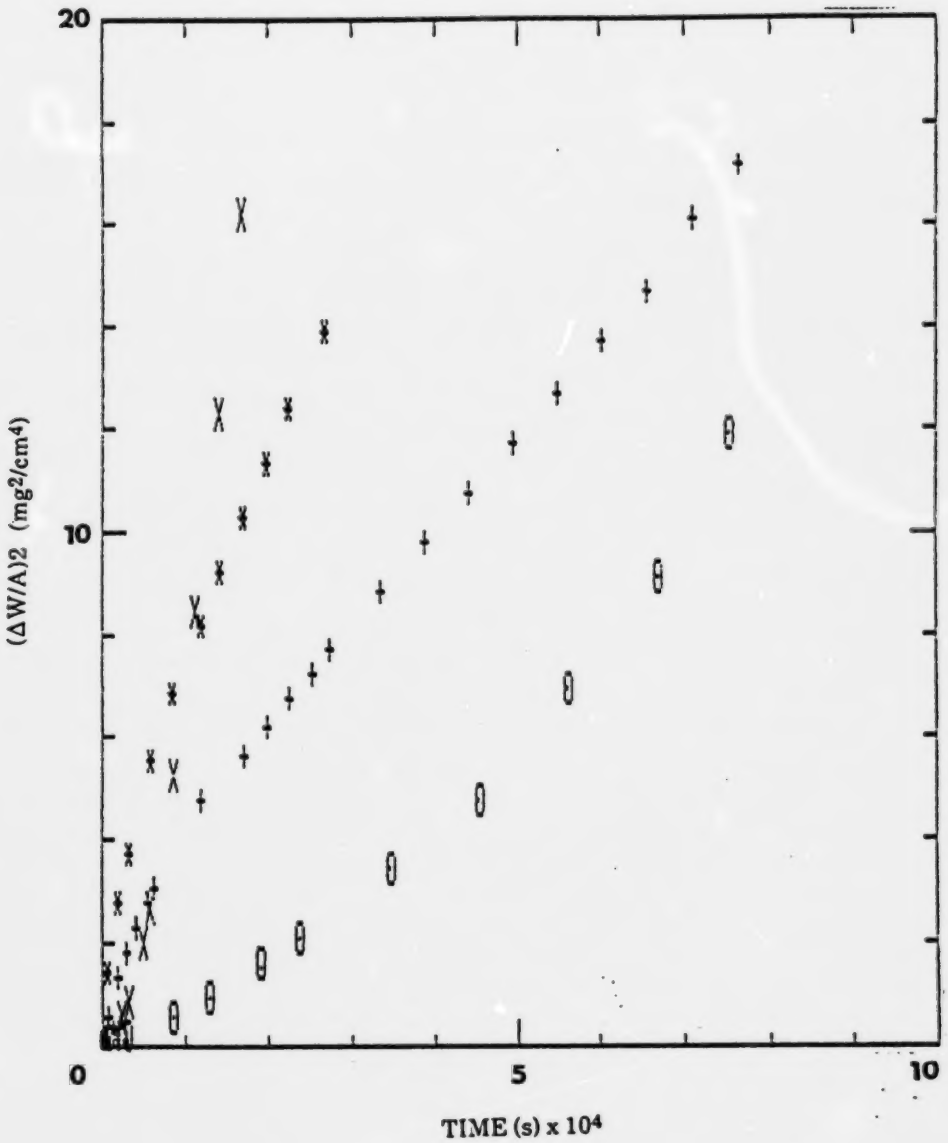

Figure 68. Weight-gain kinetics of Fe-4.1a% Al samples oxidized at 1173 K and 26.7 kPa.

* - Unimplanted - C14
\+ - 7.5 x 10^{16} Al/cm^2 - C8
0 - 1.5 x 10^{17} Al/cm^2 - C11
X - 1.5 x 10^{17} Al/cm^2 - C12

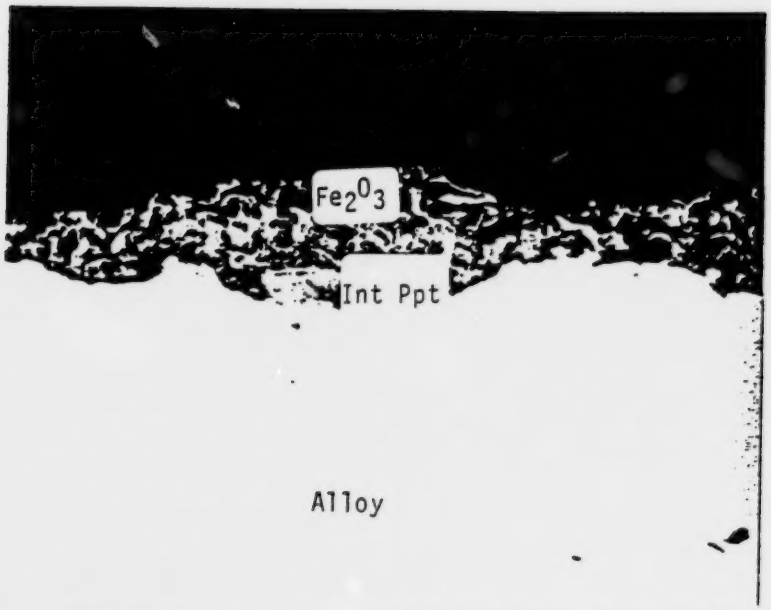

Figure 69. Metallographic cross-section of Fe-5a% Al sample, unimplanted after 8.65 x 10^4 s at 1173 K and 26.7 kPa (400X).

Figure 70. S.E.M. image of nodule on the surface of Fe-5a% Al alloy implanted with 7.1 x 10^{15} Al/cm^2, after 1.8 x 10^5 s at 1173 K and 26.7 kPa (287X).

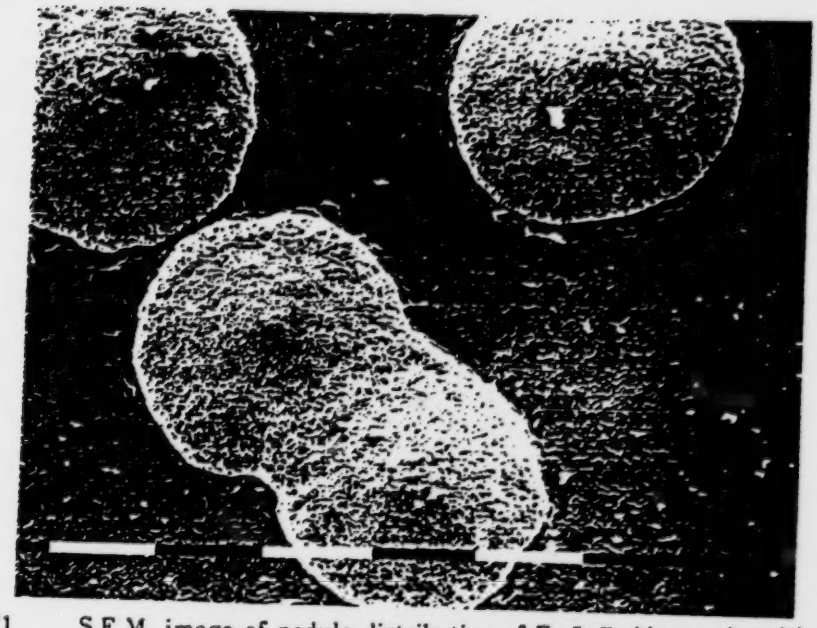

Figure 71. S.E.M. image of nodule distribution of Fe-5a% Al sample with 7.1×10^{15} Al/cm^2 after 7.2×10^4 s at 1173 K and 26.7 kPa (143X).

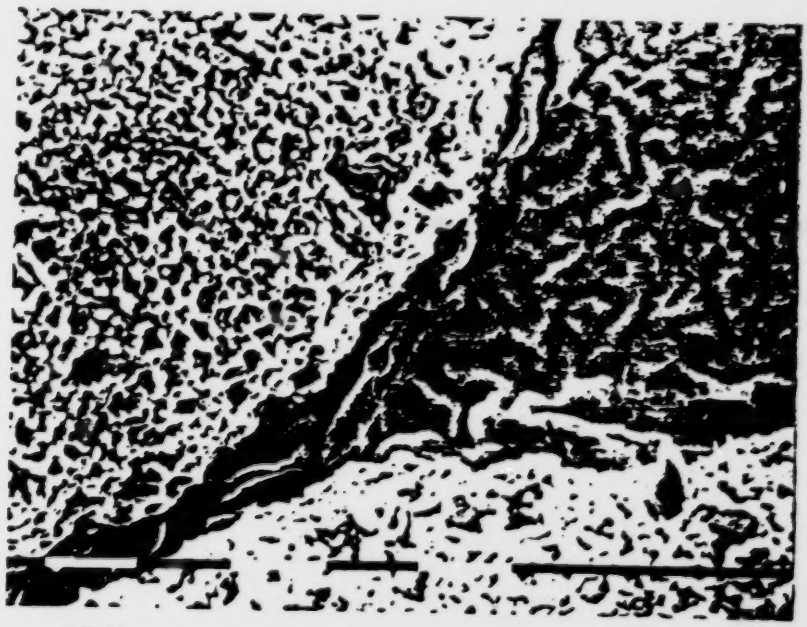

Figure 72. S.E.M. image of scale-nodule relationship on the same sample as Figure 71 (1250 X).

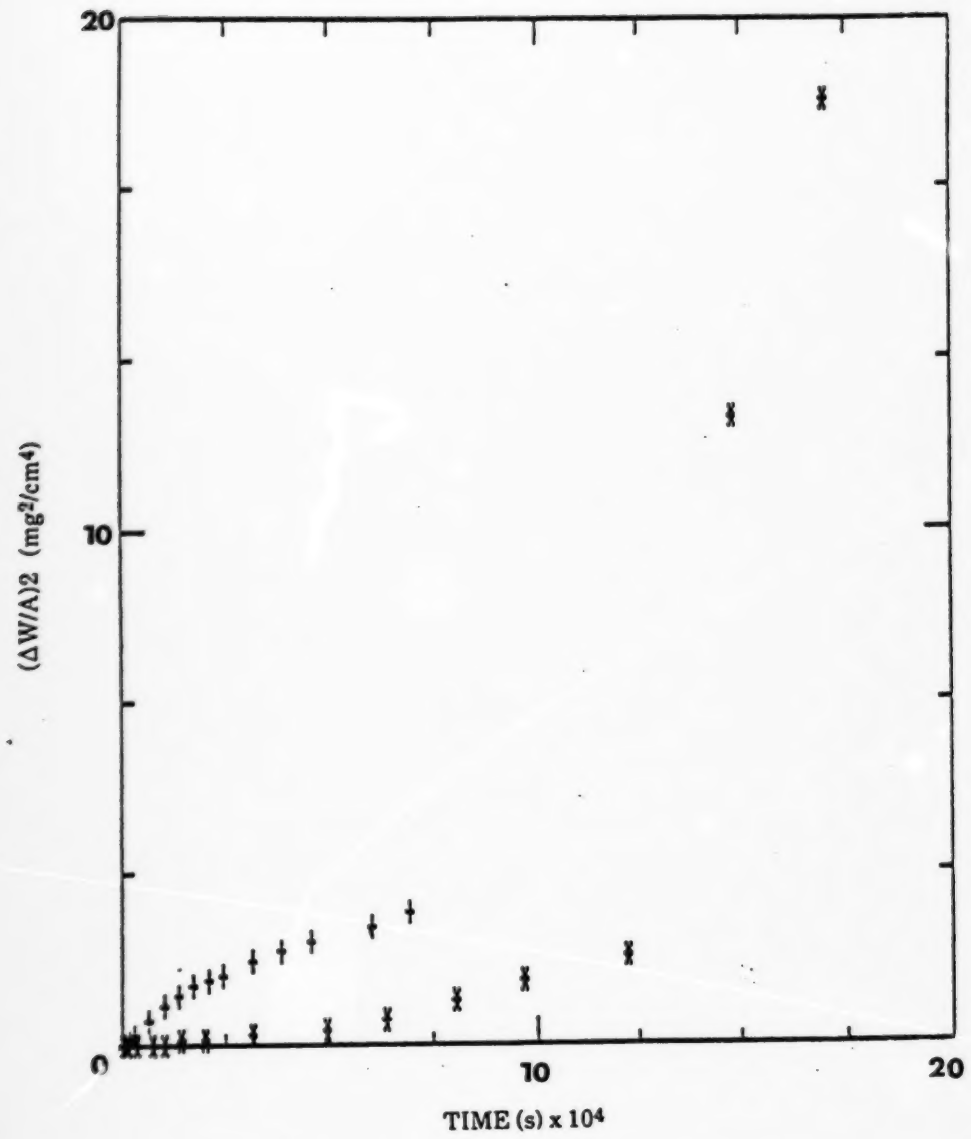

Figure 73. Long-term weight-gain kinetics for Fe-5a% Al samples oxidized at 1173 K and 26.7 kPa.

* - 1.9×10^{17} Al/cm² - E9
0 - 1.9×10^{17} Al/cm² - E10

initial protective film on a sample implanted with 1.65×10^{17} Al/cm^2 after a period of 1.25×10^5 s.

This alloy is definitely capable of forming duplex films as a result of implantation. Even the smallest dose attempted, 8.25×10^{15} Al/cm^2, produced a reddish film. One side of sample x 10^3 was overgrown with nodules after 2.5×10^4 s, resulting in weight gain much larger than that of sample E2. A long-term trial was carried out and nodule growth followed a 1.25×10^5 s induction period. The unimplanted alloy formed a triplex, $Fe_2O_3/Fe_3O_4/Al_2O_3$ film after only 2.9×10^4 s, much less time than the same morphology takes to form at 101 kPa.

Implanted Fe-5a% Al samples had a much slower weight-gain than unimplanted specimens, as shown in Figures 74 and 75. Table 22 contains parabolic rate constants and 3 σ confidence estimates for weight-gain kinetics.

TABLE 22 - Parabolic rate constants and estimated confidence intervals for Fe-5a% Al samples oxidized at 1173 K and 26.7 kPa.

SAMPLE	DOSE	K_{pl} (mg^2/cm^{4}s)	
E1	NIL	$2.38 \pm .30 \times 10^{-4}$	
E14	NIL	$2.74 \pm .57 \times 10^{-4}$	
E2	8.25×10^{15}	$1.14 \pm .08 \times 10^{-5}$	
E3	8.25×10^{15}	$8.88 \pm .62 \times 10^{-5}$	
E7	8.25×10^{16}	$4.99 \pm .42 \times 10^{-5}$	
E10	1.65×10^{17}	$4.38 \pm .68 \times 10^{-5}$	
E9	1.65×10^{17}	$8.27 \pm 2.2 \times 10^{-6}$	$t_{12} < 1.25 \times 10^5$ s.

g) Fe-9.8a% Al 1173 K P_{O_2} 26.7 kPa

The iron oxide nodules which produced the irreproducible kinetics of Figure 78 are shown in the SEM micrographs of Figures 76 and 77. Typically, a reddish scale, heavily

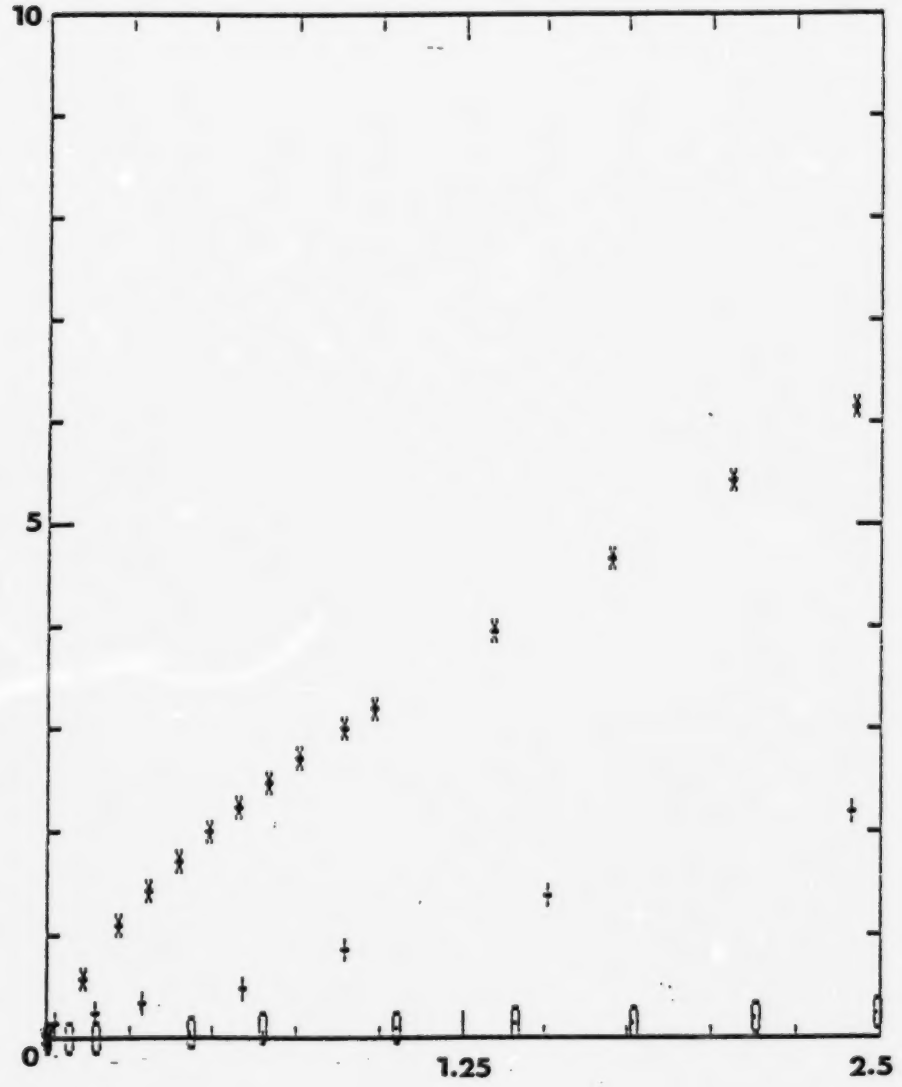

Figure 74. Weight-gain kinetics of Fe-5a% Al samples oxidized at 1173 K and 26.7 kPa.

* - Unimplanted - E1
+ - 7.1 x 10^{15} Al/cm2 - E3
0 - 7.1 x 10^{15} Al/cm2 - E2

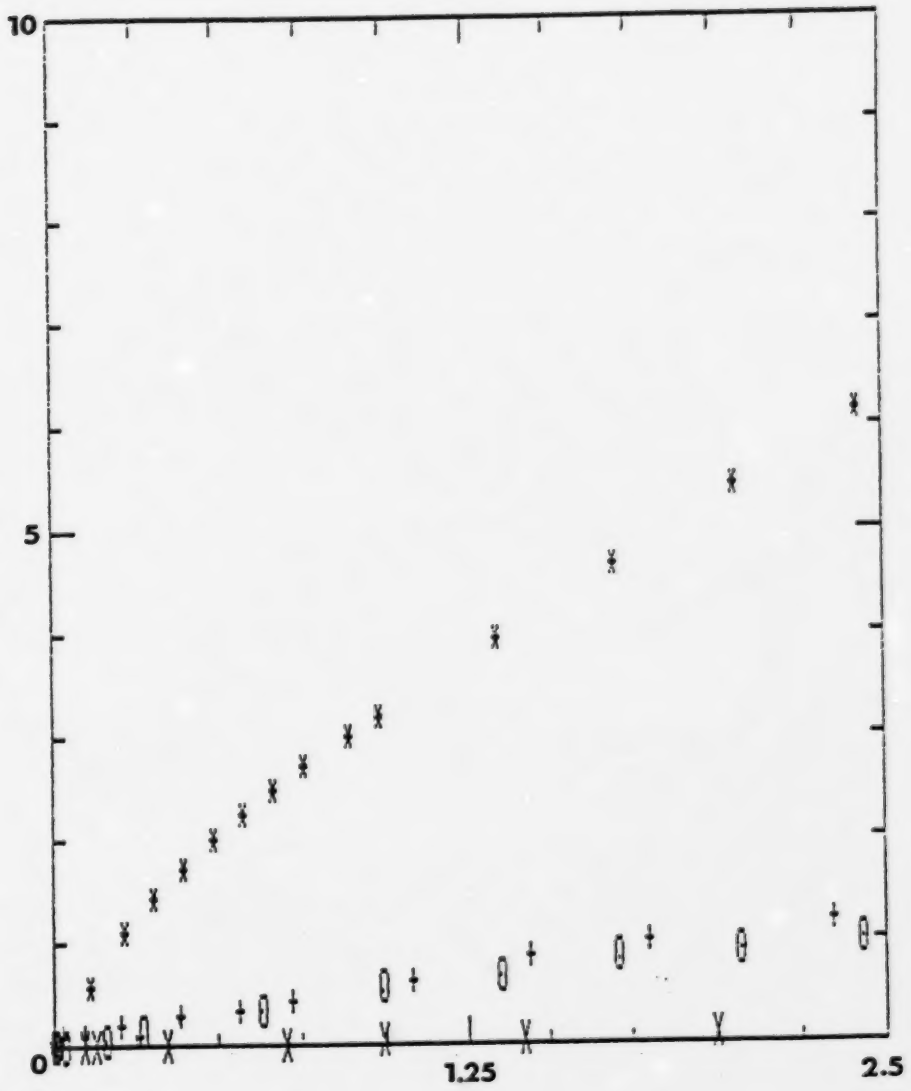

Figure 75. Weight-gain kinetics for Fe-5a% Al samples oxidized at 1173 K and 26.7 kPa.

* - Unimplanted - E1
\+ - 7.1 x 10^{16} Al/cm^2 - E7
0 - 1.9 x 10^{17} Al/cm^2 - E9
X - 1.9 x 10^{17} Al/cm^2 - E10

Figure 76. S.E.M. image of scale/nodule relationship on Fe-9.8a% Al sample implanted with 7×10^{15} Al/cm^2 after 3.25×10^4 s at 1173 K and 26.7 kPa (625X).

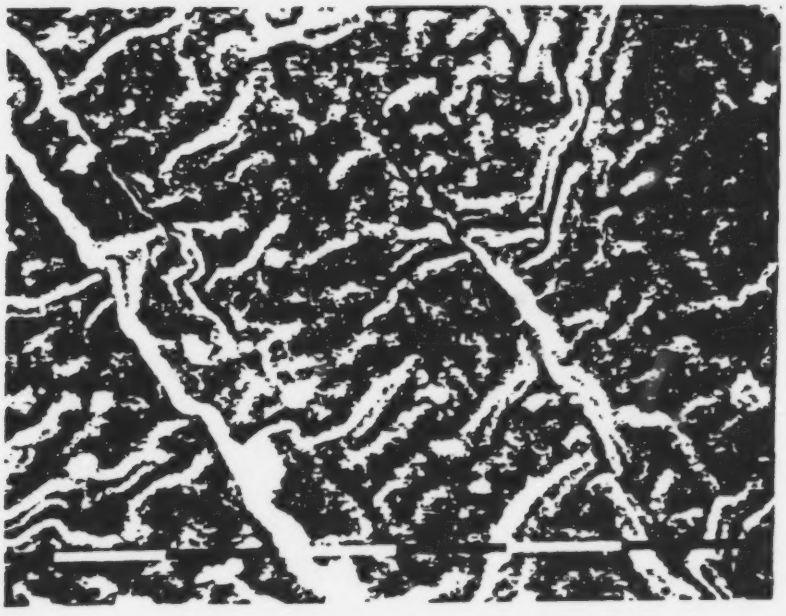

Figure 77. S.E.M. image of the same sample as Figure 76, scale morphology (1550X).

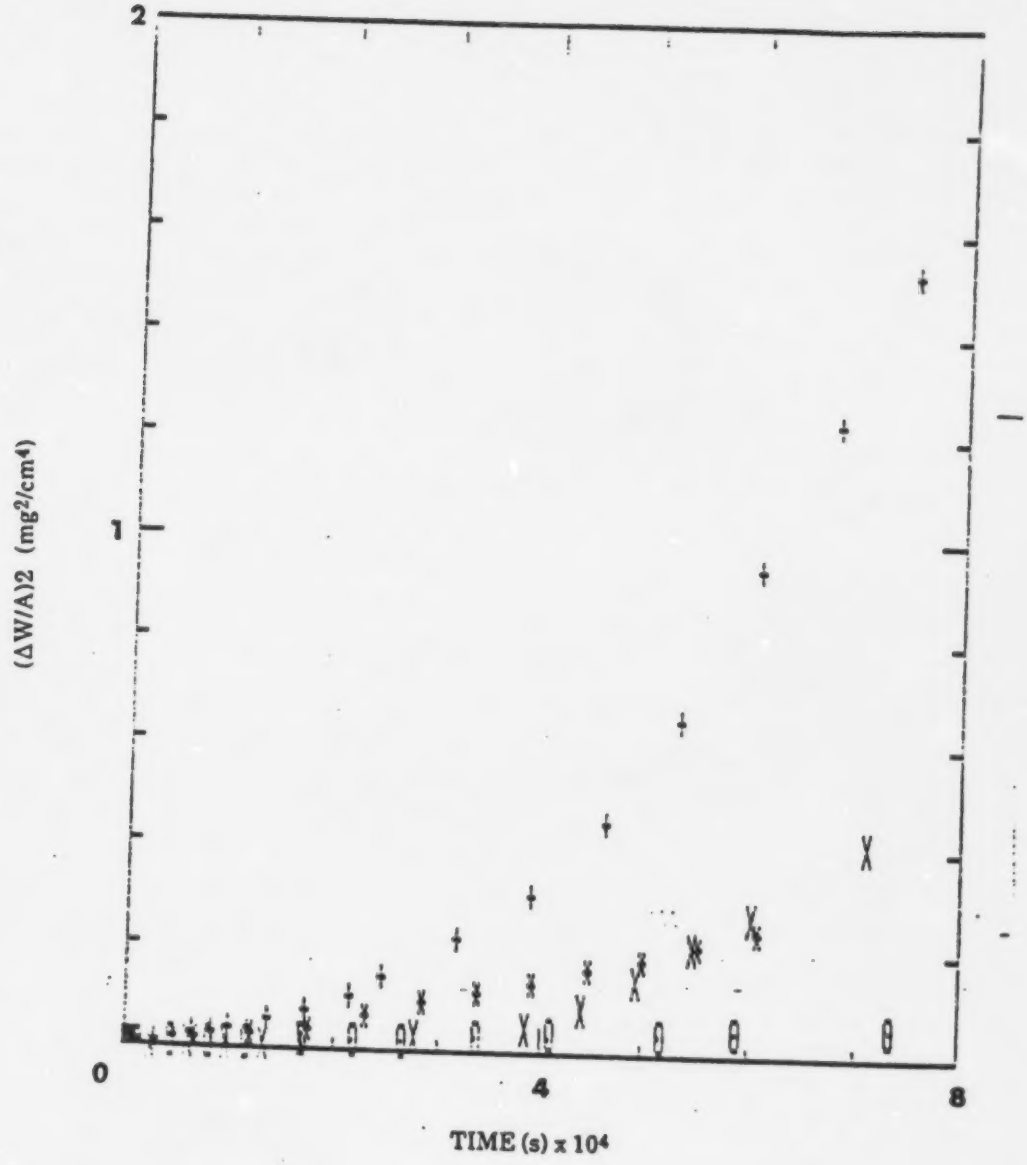

Figure 78. Weight-gain kinetics for Fe-9.8a% Al samples oxidized at 1173K and 26.7 kPa.

* - Unimplanted - B41
\+ - 7 x 10^{15} Al/cm² - B39
0 - 1.4 x 10^{17} Al/cm² - B44
X - 1.4 x 10^{17} Al/cm² - B45

wrinkled and buckled, was penetrated by these nodules. No weight gain was measurable on a sample oxidized two months after polishing, on which not a single nodule formed.

Weight-gain kinetics (Table 23) for this alloy were dominated by nodule growth. The only sample free of nodules was one oxidized several months after polishing. If the presence of a surface oxide has an inhibiting effect on nodules, there exists a systematic bias in favour of implanted specimens in this investigation: As implantation was on a batch basis, implanted samples, on average, had longer to form a surface oxide than unimplanted samples, which were polished soon before oxidation. The order of magnitude increases in parabolic rate constant sometimes seen after long exposure indicate the onset of runaway nodule growth after an induction period. A duplex film was observed by Ahmed (33) for alloys of Fe-7 and -8a% Al, but nodules were never observed. Nodules were observed, however, by Tomas (40) at similar enrichments on what he identified as an alumina film.

TABLE 23 - Parabolic rate curves and confidence estimates for Fe-9.8a% Al samples oxidized at 1173 K and 26.7 kPa.

SAMPLE	DOSE	K_{p1} (mg^2/cm^4s)	K_{p2} (mg^2/cm^4s)	t_{12}
B44	1.4×10^{17}	$8.04 \pm .47 \times 10^{-7}$		
B39	7.1×10^{15}	$7.23 \pm 1.54 \times 10^{-6}$	$3.79 \pm .42 \times 10^{-5}$	4.0×10^{4}
B45	1.4×10^{17}	$1.22 \pm .26 \times 10^{-6}$	$1.21 \pm .09 \times 10^{-5}$	4.0×10^{4}

No conclusions can be drawn about the improvement in kinetics of this alloy due to implantation, but it can be noted that a dose of 1.4×10^{17} was insufficient to produce undisturbed Al_2O_3 on this alloy.

The oxidation results of this investigation are summarised in Figure 79, which has as its two axes Al dose and Al alloy content. Kinetics of unimplanted samples were generally

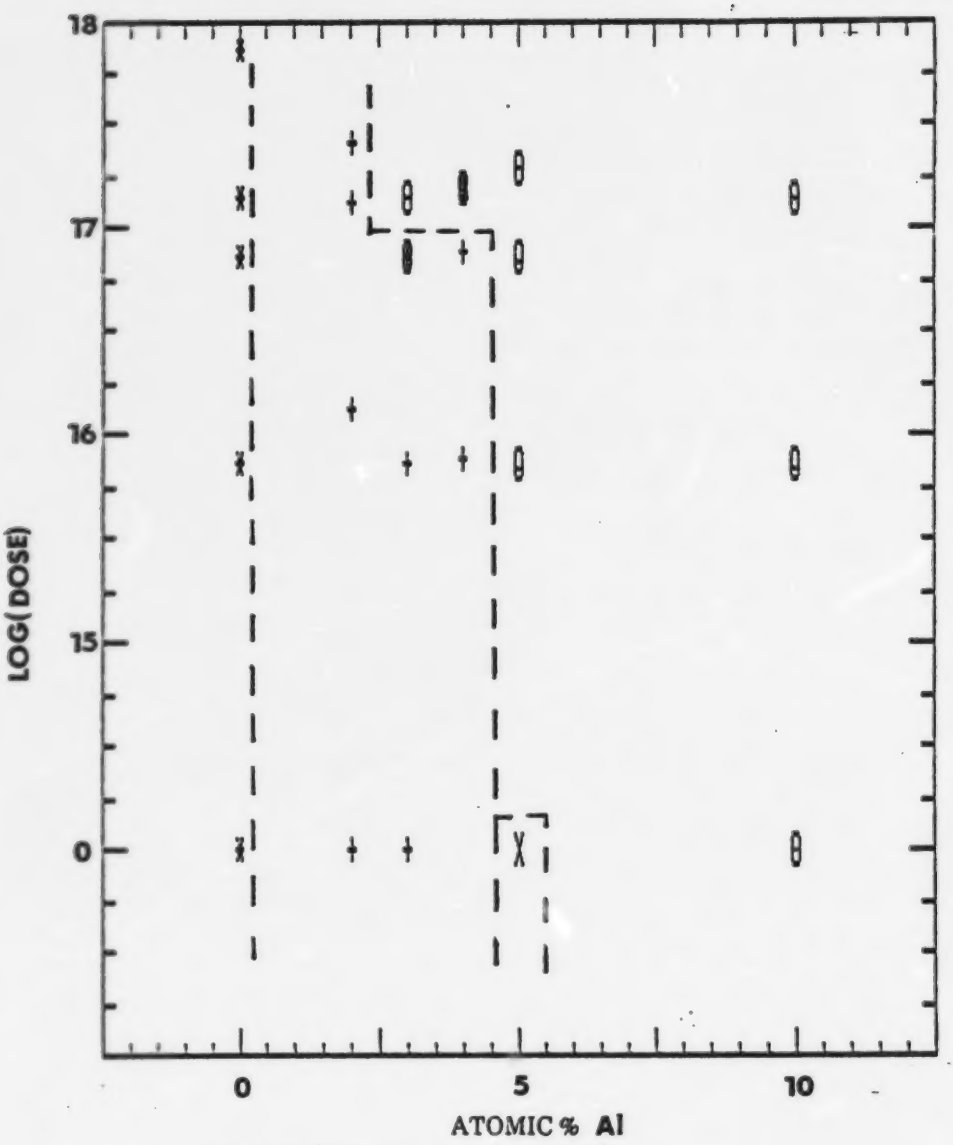

Figure 79. Observed morphologies as a function of alloy content and dose.

within 10% of replicate kinetics. Scatter was somewhat higher for implanted specimens without nodules, and very much higher for samples with nodules. Irreproducibility for any sample could be due to alloy composition inhomogeneity or irreproducible coating. The extra scatter observed for implanted specimens could be due to dose inhomogeneity. The first few minutes of oxidation were not very reproducible due to difficulty in heating up the specimen in a standard fashion.

Figure 80 outlines a proposed model for oxidation after Al implantation. Figure 80(a) illustrates the situation after implantation: a zone 200 nm thick has been created, enriched in Al but heavily damaged. The amount of oxygen required to oxidize this thin layer depends on the amount of Al, but is less than 150 $\mu g/cm^2$. Typically, this much oxygen is taken up in less than 100 s at 1173 K. Figure 80(b) represents the surface of the sample after this period. The sample has not reached 1173 K, and while the nature of the oxides present can not be known exactly, it seems certain that both Al and Fe oxides are present.

After the initial 100 s, the amount of Al in the alloy begins to influence the progress of oxidation. Figure 80(c) and (d) shows the progress of oxidation on a pure Fe sample.

The Fe-rich oxides become FeO, and rapid growth outward occurs. No Al exists to diffuse outward and support the Al-rich oxides on the surface, which become buried in a massive layer of FeO. FeO can dissolve up to .55 mole% Al_2O_3 at 1173, and the implanted Al will not be enough to exceed this limit. Perhaps islands of $FeAl_2O_4$ briefly exist under a continuous FeO layer, as in the model of Pons, but as the final rate of all implanted specimens is that of pure Fe oxidation, the implanted Al has almost certainly dissolved in FeO. For alloys of greater than 2a% Al, a duplex film with nodules could be formed on oxidation of specimens implanted with a sufficient dose. This suggests that after the initial 100 s, some parts of the sample were covered in a thin alumina film, and some had areas of Fe-rich oxide

Figure 80. Proposed model for oxidation of implanted Fe-Al alloys.

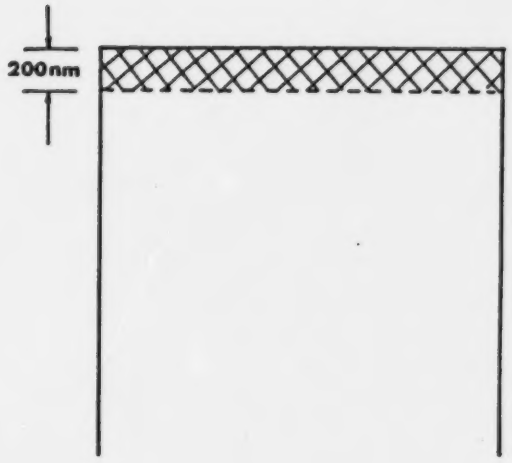

(a) Zone, 200 nm thick, enriched in Al and heavily radiation damaged.

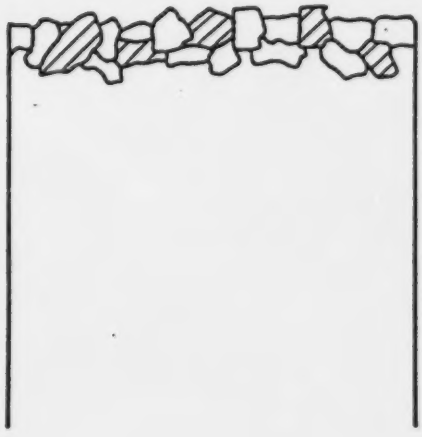

(b) Formation of mixed oxides of unknown form after 100 s of oxidation.

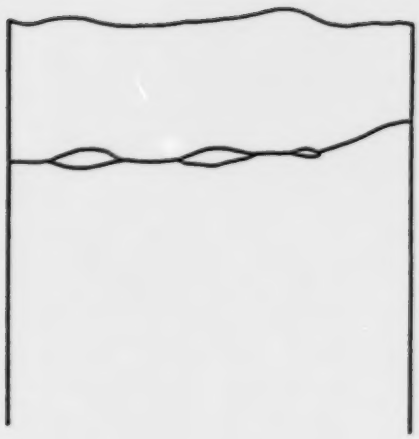

(c) Al-rich oxides buried by outward-growing FeO.

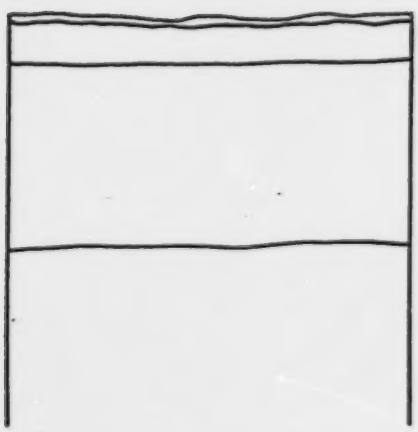

(d) Triplex morphology forms, Al dissolved in FeO.

(Fig. 80(e)). Fe diffusion would occur through the alumina film's short-circuit defects, (Figure 80(f)), creating a surface layer of hematite. The damage present in the as-implanted sample may result in an increased number of short-circuit paths, put there is no evidence to confirm this. Some outward Fe diffusion occured through the nodules, as some nodules had a distinctly bulging outward appearance. The noduled duplex film could not be produced on alloys of 2a% Al and less, regardless of dose, and a possible mechanism is outlined in Figure 80(g) to (i). As in the case of alloys with more than 2a% Al, Fe-rich nodules and an aluminum oxide film may appear.

Many more nodules and a thinner oxide film may result from less Al diffusion outward from the alloy. Diffusion of Fe through the alumina film perhaps first formed a hematite film on the surface, but the alumina was then converted to $(Fe,Al)_3O_4$. Internal precipitation of spinel/alumina particles occured when oxygen diffusion through the nodules reacted with alloy aluminum. After longer exposures, the nodules coalesced to form a continuous Fe_2O_3 film, thicker wherever nodules had originally formed, over a $(Fe,Al)_3O_4$ film, thicker wherever the alumina film originally existed.

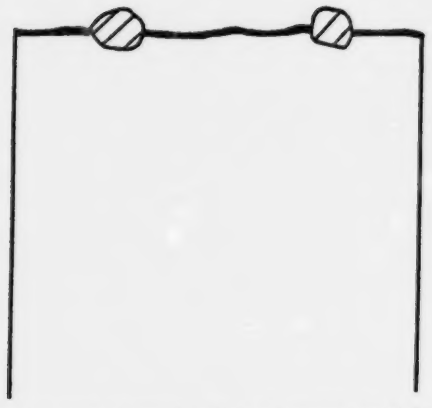

(e) Formation of nodules and alumina film on more enriched alloys after implantation.

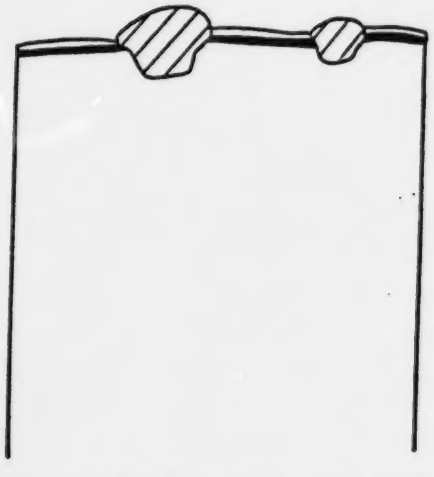

(f) Growth of nodules and hematite above alumina on more enriched alloys after implantion.

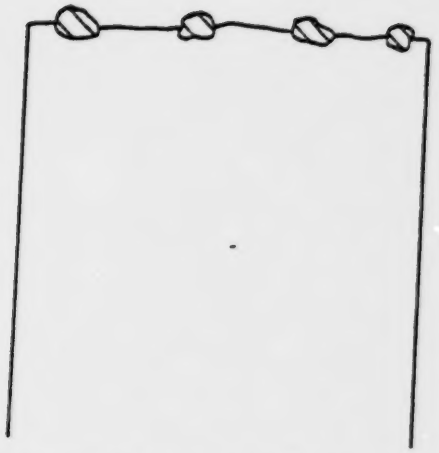

(g) Formation of many nodules and thin alumina film on implanted alloys of at least 2a%.

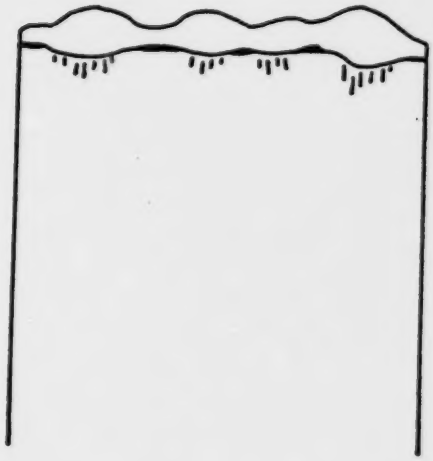

(h) Growth of nodules and thick hematite layer above alumina on implanted alloys of at least 2a%.

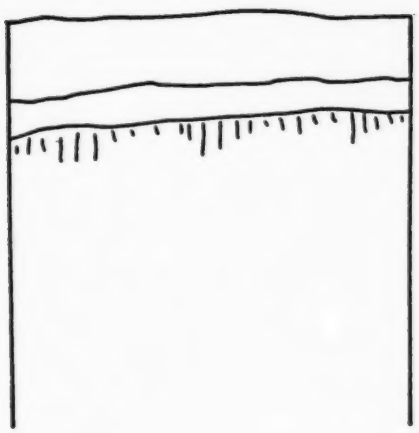

(i) Formation of $(Fe, Al)_3O_4$ layer under hematite and coalescense of nodules.

CHAPTER 6

CONCLUSIONS AND SUGGESTIONS FOR FURTHER WORK

Hydrogen reduction seems to be a workable method for the removal of room temperature oxide films from Fe prior to deposition of evaporated layers. A drawback to this technique is the significant interdiffusion of evaporated films on the first side to be reduced. Although such an effect makes preparation of uniform samples impossible, thermal diffusion could be a preferable technique for the formation of adherent Al layers.

Many layers and low oxygen levels speed ion beam mixing, but sample preparation is much more difficult. Trial mixing configurations can be tested on graphite blanks and the progress of mixing followed by RBS, but mixing results on graphite can differ from those of the same configuration on a metal substrate.

Al implantation of pure Fe is effective in decreasing oxidation rates at 873K, but ion-beam mixing shows even more effectiveness. The proposal that inhibition of oxidation at 810 K is due to formation of hercynite islands should be tested by identification of oxidation products resulting from oxidation of implanted pure iron at temperatures between 873 and 1173 K, as between these temperatures, hercynite becomes completely soluble in magnetite.

Some Fe-Al alloys treated by ion-implantation of Al show improvement in oxidation resistance at 1173 K, both in the rate of oxidation and the morphology of oxides. Al_2O_3 was not, unfortunately, formed on any alloy. A duplex Al_2O_3/Fe_2O_3 film with Fe oxide nodules can be formed by implantation, rather than the triplex $Al_2O_3/Fe_3O_4/Fe_2O_3$ morphology formed naturally on more enriched alloys.

In order to increase the surface concentration of Al, implantations should be carried out at lower energies. The higher sputtering yield at a lower energy should produce a

concentration profile less like a perfect Gaussian. Doses of two or more energies should be attempted to increase the retained dose of Al in the near-surface region. These two experiments would help to determine if the amount or surface concentration of implanted species is more important in improving kinetics.

If the proposed model be correct, the absolute amount of Al in the implanted zone is more important than the surface concentration. Further, some nodules of Fe oxides will always appear on the surface as implantation can never create a surface zone free of Fe. Ion-beam mixed surface films, which produce a pure Al layer, may therefore be capable of forming nodule-free surfaces. This will require a cold deposition system with some facility to remove surface oxide.

To form Al_2O_3 before raising the sample to temperature, an implantation of oxygen could follow implantation of aluminum in stoichiometric amounts (78). Annealing might be considered to form chemical bonds between the implanted species, before reaching oxidation conditions.

REFERENCES

1. "The thermodynamics of volatilization of Chromic Oxide. Part I." Kim, Y.W., and Belton, G.R., Met. Trans., 5, 1811. (1974).

2. "Untersuchungen uber die Verzunderung von Reisnen Eisen -Al-Legierungen in Sauerstoff.", Schmahl, Baumann and Schenk, Archiv. Eisenhutt. , 30, #6, 345. (1959)

3. "The physical properties of Fe-Al alloys.", C. Sykes and J. Bampfydle, J.I.S.I., 130, 389. (1934).

4. "Protective coatings for turbine parts.", E.S. Nichols et al, Mech. Eng., 87, 53. (1965).

5. "Implantation Metallurgy.", S.T. Picraux, Inst. Phys. Conf. Ser., #28, Chapter 5. (1976).

6. "Modification of the Corrosion behaviour of alloys by Ion Implantation.", Clayton, C.R., Wang, Y.F., IEEE Trans. Nucl. Sci., NS-30, #2, 1752. (1983).

7. "The oxidation of alloys.", G.R. Wallwork, Rep. Prog. Phys., 39, #5, 401. (1976).

8. "Some limiting factors on the use of alloys at high temperatures.", Wallwork, G.R., Hed, A.Z., Oxid. Met., 3, #2, 171. (1971).

9. "Oxidation of Iron.", A. Goursat and W.W. Smeltzer, Rev. High Temp. Mat., 1, 353. (1971).

10. "On the interdiffusion in solid solution of the Fe-Al system in Al vapour.", K. Nishida et al., Trans. Jap. Inst. Met., 12, 310. (1971)

11. "Metallurgy and Metal research: All-union scientific and technical conference on the use of radioactive and stable isotopes and radiation in the national economy and science.", Izd. Akad. Nauk SSSR, NP-Tr-448, Moscow. (1958)

12. "Investigation of Fe diffusion in corundum and rutile by means of 59Fe indicator.", Izvekov, V.I., Gorbunova, K.M., Fiz. Met. i Metalloved., 7, 713. (1959)

13. "High temperature oxidation of metals and alloys.", Frantsevich, I.N., et al., Gostekhizdat Ukr. S.S.R. (1963)

14. Hennicke, H.W., Strurhahn, H.H., Z. Tonindustrie, 95, 127. (1971).

15. "Self-diffusion in iron." Buffington, F.S., Hirano, K., Cohen, M., Acta Met., 9, 434. (1961)

16. "Self-diffusion in iron." Graham, D., Tomlin, D.H., Phil. Mag., 8, 1581. (1963)

17. "The Kirkendall effect in diffusion of Aluminium in α-Fe." Sato, K., Trans. J.I.M., 4, 121. (1963)

18. "Relative thermodynamic properties of solid Fe-Al alloys." S.V. Radcliffe et al., Acta. Met., 9, 169. (1961)

19. "Thermodynamics of the system Fe-Al-O between 1073K and 1573K.", F. Elrefaie and W.W. Smeltzer, Met. Trans., 14B, 85. (1983)

20. "Results of investigations of Important Solid-State Reactions.", P. Budnikov et al., Principles of Solid- State Chemistry, 298, Gordon & Breach, N.Y., N.Y. (1968)

21. "J.A.N.A.F. Thermochemical tables.", 2nd ed. D.R. Stull and H. Prophet, U.S. Dep't of Commerce. (1971)

22. "The system Fe-O. Part II Equilibrium and Thermodynamics of liquid oxide and other phases.", L. Darken and R. Gurry, J. Am. Chem. Soc., 68, 798. (1946)

23. "The dissociation pressure of hematite.", Bryant and W.W. Smeltzer, J. Electrochemical Soc., 116, 1409. (1969)

24. "Metal and Oxygen activities in the Fe-Ni-O and Ni-Cr-O systems between 900 and 1100 C.", H. Davies, Ph.D. Thesis, McMaster Univeristy. (1973)

25. "Electromotive measurements in high-temperature systems.", 3, B.C.H. Steele, American Elsevier, New York. (1968)

26. "Solidus, Subsolidus and Subdissociation Phase Equilibrium in the system Fe-Al-O.", L. Atlas and W. Sumida, J. Am. Ceram. Soc., 41, #5, 150. (1958)

27. "Thermochemical properties of inorganic substances.", I. Barin, O. Knacke and O. Kubachewski, Springer-Verlag, Berlin. (1977)

28. "Electrochemical measurement of the oxygen potential of Fe-Al-Hercynite in the temperature range 750-1600 C." J. C. Chan et al, Can. Met. Quarterly, 12, 439. (1973)

29. "Metallurgical Thermochemistry.", O. Kubachewski, Pergamon Press, Oxford. (1979)

30. "A review of the Diffusion path concept and its application to the high-temperature oxidation of binary alloys." A. Dalvi and D. Coates, Oxid. of Metals, 5, #2, 113. (1972)

31. "Formation of composite scales consisting of oxides of different metals.", C. Wagner, J. Electrochem. Soc., 103, #11, 627. (1956)

32. "Handbook of Chemistry and Physics.", ed. R.C. Weast, CRC publishing co., 60th edition, p B-52. (1979)

33. "Oxidation properties of Fe-Al alloys at 1173K.", H. A. Ahmed, Ph.D. thesis, McMaster University. (1984)

34. "High-temperature oxidation and corrosion of metals and alloys.", Stringer, J., Whittle, D.P., Rev. Int. Htes. Tempt. et Refract., 14, #1,6. (1977)

35. "On the diffusion of oxygen through solid iron." Meijering, J.L., Acta. Met., 3, 157. (1955)

36. "Handbook of Chemistry and Physics.", ed. R.C. Weast, CRC publishing co., 60th ed., pg B-85. (1979)

37. "Contribution a l'etude de la resistance a l'oxydation des alliages Fe-Al.", P.Pepin and L. Tertian, Metaux, 36, 140. (1961)

38. "Transformation observees dans des couches minces d'alliage Fer-Aluminium chaufées dans l'air ou dans le vide.", J.J. Trillat, L. Tertian, and P. Pepin, Metaux, 36, 133. (1961)

39. "The oxidation of Fe-Al alloys from 450 to 900 C.", W.E. Boggs, J. Electrochem. Soc., 118, #6, 906. (1971)

40. "The development of oxidation-resistant Fe-Al-Cr alloys." P. Tomas, Ph.D. Thesis, U.N.S.W. (1982)

41. "Oxidation of Fe-Al Alloys in the range 500-1000C." Saegusa,F. & Lee L., Corrosion, 22, 168. (1966)

42. "The oxidation of Fe, Ni and Co-base alloys containing Al.", W.C. Hagel, Corrosion, 21, 316. (1956)

43. "The oxidation properties of Fe-Al alloys at 1273 K." A.L. Porter, Senior thesis, McMaster University. (1984)

44. "Classical Mechanics.", Goldstein, H., Addison-Wesley, Cambridge. (1958)

45. "Influence of crystal lattice on motion of energetic charged particles." Lindhard, J., Mat.-Fys. Medd. Dan. Vid. Selsk., 34, 14. (1965)

46. "Range concepts and heavy ion ranges." Lindhard, J., Nielsen, V., Scharff, M., Mat.-Fys. Medd. Dan. Vid. Selsk. 33, 14. (1963)

47. "Energy deposition by ions in the keV range." Lindhard, J., Scharff, M., Phys. Rev., 124, 128. (1961)

48. "Spatial distribution of energy deposited by atomic particles in elastic collisions." Winterbon, K.B., et al., Mat.-Fys. Medd. Dan, Vid. Selsk. 37, 14. (1970)

49. "Influence of anisotropic scattering on stopping by elastic collisions.", Baroody, E.M., J. Appl. Phys., 36, 3565. (1965)

50. "Ion implantation range and energy deposition distribution." v. 2 "Low incident ion energies." Winterbon, K.B., IFI/Plenum Data Co., New York. (1975)

51. "DISTBN" Thompson, D.A., McMaster University, Hamilton.

52. "NUDIST" Beauprie, R.M., McMaster University, Hamilton.

53. "Ion implantation and beam processing.", ed. Poate, J.M. and Williams, J.S., pg 6., Academic Press, New York. (1984)

54. "On the nature of radiation damage in metals." Brinkmann, J. A., J. Appl. Phys., 25, 961. (1954)

55. "Stochastic problems in physics and astronomy." Chandrasekhar, S., Rev. Mod. Phys. 15, 1. (1943)

56. "Displacement of atoms during irradiation." Seitz, F., and Koehler, J.S., Solid State Physics, 2, 305. (1956)

57. "Radiation-enhanced diffusion in solids." Dienes, G.J., Damask, A.C., J. Appl. Phys., 29, 12, 1713. (1958)

58. "Ion beam mixing of Sb layers in Al." Paine, B.M., Nicolet, M.A., Banwell, T.C. in "Metastable materials formation by ion implantation." ed. Picraux, S.T. and Choyke, W.J. Elsevier Scientific, New York. (1982)

59. "A comparison of atomic mixing behaviour of Cu-Au and Cu-W systems for room temperature and low temperature irradiation." Wang, Z.L., Westendorp, J.F.M., Doorn, S., Saris, F.W. in "Metastable materials formation by ion implantation." ed. Picraux, S.T. and Choyke, W.J. Elsevier Scientific, New York. (1982)

60. "Ion mixing in Al, Si, and their oxides.", Barcz, A.I., and Nicolet, M.-A., Applied Physics A 33, 167. (1984)

61. "Ion mixing in Al, Si and their oxides.", Jaouen, C., et al., N. I. and M., B7/8, 591. (1985)

62. "Ion induced reactions in Fe/Al bilayers by pulsed beam ion irradiation and Xe irradiation." Nastasi, M., et al, in Proceedings of the Fourth International Conference on Ion beam modification of Materials, Cornell University, Ithaca, N.Y. July 16-20, 1984.

63. "The high-temperature oxidation of Al-implanted Fe." Pons, M., Caillet, M., Galerie, A., Corrosion Sci., 22, #3, 239. (1982)

64. "Crystal data on $(FeAl)_2O_3$.", Dayal et al., Acta. Cryst. 18, 574. (1965)

65. "Ion implantation into metals to prevent high temperature oxidation." Pons, M., Caillet, M., Galerie, A., N.I. &M. 209/210, 1011. (1983)

66. "The effects of heat treatment and implantation of Al on the oxidation resistance of Fe-Cr-Al-Y alloys." Bernabai, U., Cavallini, M., Bombara, G., Corrosion Sci., 20, 19. (1980)

67. "The influence of the surface ion implantation of Al and Y upon the oxidation behaviour of a Fe-15%Cr-4%Al Fecralloy stainless steel, in air, at 1100C." Bennet, M.J., Houlton, M.R., Dearnaley, G. Corrosion Sci., 20, 69. (1980)

68. "Oberflachenanreicherung bein zerstauben mit versheidenen ionenergien.", Opitz,M., Betz, G., Braun, P., Acta Phys. Acad. Sci. Hung., 49, 119. (1980)

69. "Energy dependence of the yields of ion-induced sputtering of monatomic solids." Matsunami, N., et al., IPPJ-AM-32, Institute of Plasma Physics of Japan, Nagoya University, Nagoya, Japan.

70. "Short and long range ion beam mixing in Cu:Al. Influence of interfacial oxide." Besebacher, F., Bottiger, J., Nielsen, S.K., Whitlow, H.J. Appl. Phys., A29, 141. (1982)

71. "Whickham Technology Systems Ltd. Ion Accelerator.", Whickham technology systems Ltd. (1985)

72. "Contribution a l'etude du mechanisme d'oxydation du fer par l'oxygene ou l'air a temperature elevee." Goursat, A., D.S.P. Thesis, Universite d'Orleans. (1980)

73. "Powder diffraction file search manual.", Joint committee of powder diffraction standards, Penna., U.S.A. (1977)

74. "Constitution of binary alloys." Hansen, M., McGraw-Hill, N.Y., 2nd ed. (1958)

75. "The oxidation of Al in the temperature range 400-600 C." Smeltzer, W.W., J. Electrochemical Soc., 103, 209. (1957)

76. "Investigation of steels and alloys.", Gorbunov, N.S., Izd. Nauka. (1964).

77. "Diffusion in solids, liquids and gases.", Jost, W., Academic Press Inc., New York. (1960)

78. "Formation of subsurface Al_2O_3 layers in aluminum by oxygen ion implantation." Musket, R.G., et al., in "Ion beam modification of materials." Cornell U., Ithaca, N.Y. ed. B.M. Ullrich. (1984)

SECTION II

THE EFFECT OF ION IMPLANTATION OF ALUMINUM UPON OXIDATION OF Fe-6 a% Al ALLOY AT 1173K

ABSTRACT

Samples of an Fe-6 at% alloy were implanted with doses of 5×10^{16} to 3×10^{17} Al^+ ions/cm^2 at 100 kV, and subsequently oxidized at 1173 K in O_2 gas at 27 kPa. By comparison with the behaviour of unimplanted specimens, no effect on oxidation was observed if the dose of implant was less than 1×10^{17} Al^+ ions/cm^2. Implanting to doses of 1×10^{17} Al^+ ions/cm^2 or higher, effected a change in the oxide scaling morphology from a duplex α- Fe_2O_3/α-Al_2O_3 scale to an α-Al_2O_3-enriched film with a dispersion of α- Fe_2O_3 nodules. Oxygen uptake by the high-dose samples was due principally to nodule formation and weight gains after 45 h were lower by 50% to 70% when compared to the unimplanted material. Nucleation and growth of the nodules occurred within the first 5 h of reaction only but their presence acted as an upper limit of the benefits provided by implantation of aluminum. Nodule formation was shown to be characteristic of the oxidation properties of the alloy material, not an extraneous feature introduced by the implantation process itself. Surface preparation prior to implantation had little effect on oxidation: high-dose electropolished samples behaved similarly to mechanically polished samples when implanted to comparable doses.

INTRODUCTION

Degradation of the mechanical properties of a metal matrix by elements added to impart corrosion resistance is a problem which recurringly confronts the materials engineer. Ion implantation of the potent element into the surface regions of the alloy provides a potential solution. Thus, for example, ion-beam enrichment of aluminum in the surface of iron-based alloys should in principle greatly improve the corrosion behaviour while at the same time, maintaining the mechanical integrity of the bulk material. To date, investigations on utilizing the implantation of aluminum ions into iron or steel for corrosion resistance have been few. Pons et al. (1) found that for pure iron, near-zero rates of oxidation in the temperature range 720-1020 K were possible for those samples implanted with doses of 5×10^{16} Al^+ ions cm^2 or greater. Reduction in the cross-sectional area for activated ion diffusion by the presence of $FeAl_2O_4$ precipitates close to the scale/metal interface was considered responsible for the beneficial behaviour. If aluminum already exists in the alloy at a concentration which is sufficient to maintain high-temperature strength but too low to form an external α-Al_2O_3 layer, then aluminum implantation into the alloy may effect the desired change to formation of an external α-Al_2O_3 layer.

Bernabai et al. (2) have implanted an Fe-24Cr-1.5-0.09Y alloy, which oxides normally to form a scale predominantly composed of (Fe, Cr, Al) spinel, with aluminum to various doses. Enrichment of aluminum in the resulting oxide scale was observed and for the maximum implanted dose of 10^{17} Al^+ ions cm^2, this development gave rise to a reduction in the parabolic rate constant of oxidation after 24 hours at 1373 K by a factor of 140 compared to that for the unimplanted alloy.

For the oxidaton of an Fe-Al alloy of composition 5 at% Al at 1173 K, a subsurface α-Al_2O_3 layer ultimately forms beneath the rapidly growing α- Fe_2O_3/$(Fe, Al)_3O_4$ scale (3). For alloys richer in aluminum ($\geq$7.4 at% Al), oxidation at 1373 K causes either a duplex α-Fe_2O_3/α-Al_2O_3 film (4) or a single-phase α-Al_2O_3 film (5) to develop. The purpose of the present study is to examine the possibility of causing a transition from α-Fe_2O_3/$(Fe_{\frac{1}{2}}Al)_3O_4$/$\alpha$-

Al_2O_3 scaling behaviour to an α-Al_2O_3-rich film-type behaviour by implantation of aluminum into the alloy surface. In a broader context, the results stemming from this work should provide an opportunity to comment on the effectiveness of surface implantation of aluminum vis-a-vis conventional methods (alloying metal with aluminum, or aluminum and chromium (6)), cladding metal surface with an Al-containing coating) in forming surface oxide layers rich in α- Al_2O_3.

EXPERIMENTAL

An alloy of nominal composition Fe-6 at% Al was chosen for the implantation-oxidation studies. To allow comparison with the oxidation behaviour of Al-rich alloys, Fe-12 at% Al and Fe-16 at% Al alloys were employed in the study. All three alloys were prepared by electric-arc melting of appropriate mixtures of iron and aluminum. The pure iron and aluminum components (nominally 99.99% pure) were supplied by A.D. Mackay Corporation. The actual compositions of the alloys were determined by neutron activation analyses to be within 0.1 at% of their nominal values.

Following annealing in vacuo at 1373 K for 30 h, the alloy ingots were machined on a lathe to produce cylindrical rods of 10 mm in diameter. The rods were cleaned of oil and grease and a second annealing treatment was carried out in flowing high-purity argon at 1373 K for 50 h. Discs 1.5 mm thick were cut from each rod and wet-ground on SiC papers of successively decreasing roughness. Specimens of the Fe-12 at% Al and Fe-16 at% Al alloys were given a final surface treatment by mechanically polishing on diamond-imbedded cloths. For the Fe-6 at% Al material, specimens were either mechanically polished or electropolished in a cold (-273 K) 15% MeOH-H_2SO_4 solution immediately prior to implantation.

Implantation was carried out using a Wickdam Engineering Ion Implantation accelerator, delivering up to 600 μA of mass-analysed, single-charged, 100 kV aluminum ions. A vacuum pressure of 3×10^{-4}Pa was achieved in the target chamber, with a liquid nitrogen trap being used to reduce carbon build-up on sample surfaces. The sample

temperature remained low during implantation and for high doses it did not exceed 425 K. The ion beam impinged upon a target area of 1.0×10^{-3} m^2, allowing simultaneous implantation of three samples and a graphite blank for an independent check on the implanted dose by Rutherford Back-Scattering (RBS). The analysis by RBS was performed using 2 MeV He ions produced in a Van der Graff generator. Beam current was 50 nA and the analysis dose was 6 μC.

The implanted species adopts a Gaussian-shaped concentration profile with the radiation-damaged surface zone of ~200 nm thickness expected for a beam energy of 100 keV. For the chosen doses of 5×10^{16}, 1×10^{17} and 3×10^{17} Al^+ ions/cm^2, theoretical predictions yield peak concentrations in the profiles at 50 , 40 and 5 nm.

To investigate a possible influence of the shape of the concentrated profile (i.e. distribution of implanted Al) on oxidation, two-stage (dual) and three-stage (triple) implants up to total nominal doses of 2×10^{17} Al^+ ions/cm^2 and 3×10^{17} Al^+ ions/cm^2 using combinations of high and low beam energies were also carried out.

The oxidation experiments were run in a Cahn-electrobalance assembly with a sensitivity of 1×10^{-5} g. Pure oxgen at 27 kPa and a reaction temperature of 1173 K provided the oxidising environment for all oxidation runs. Analysis of the corroded specimens involved the concerted use of scanning electron microscopy, optical microscopy, EDAX analysis, x-ray and electron diffraction analyses.

EXPERIMENTAL RESULTS

Gravimetric Kinetics

The weight-gain data for oxidation of the unimplanted Fe-6at% Al specimens and for those implanted with aluminum to various doses are presented in Fig. 1(a) (linear-co-ordinates) and in Fig. 1(b) (parabolic-growth co-ordinates) for reaction periods up to

50 hours. The data pertains only to specimens prepared with mechanically polished surfaces prior to Al-implantation. The oxide-growth curves exhibit similar features for all specimens: an initial stage of rapid oxidation is followed by an interval of decreasing reaction rate until a stage of slow growth of oxide eventually prevails. It may be seen from Fig. 1(b) that both stages of reactivity comply well with parabolic-type scaling behaviour and the measured parabolic rate constants are given in Table 1.

Typically, the weight gained prior to the onset of slow growth accounts for at least 90% of the total weight gained after 45 hours reaction. Thus the time at which slow growth commences is important. Samples implanted to doses up to 1×10^{17} Al^+ ions/cm^2 behave similarly to the untreated material, with the onset of slow growth occurring after reaction for ~20 hours. When the magnitude of the implant dose exceed 1×10^{17} Al^+ ions/cm^2, there is, however, a significant change. Slow growth now commences as early as 6 hours, thus resulting in weight-gains after reaction times of 45 hours which were reduced by 50 to 70% compared to the unimplanted specimens. Further increase in the dose of implant to 3×10^{17} Al^+ ions/cm^2 does not provide any additional benefits. Equally, the oxidation behaviour of samples of single implants is not at variance with that observed for samples of dual or of three-stage implants for the same total dose; it is only the absolute concentration of implanted aluminum which is of importance. In this regard, it must be mentioned, however, that, although the gravimetric data for the sample implanted to 1×10^{17} Al^+ ions/cm^2 suggests little improvement, a second set of samples implanted to this dose but in a different implant-run behaved differently. Weight-gain data was not recorded for these samples but they developed an oxide scale morphology characteristic of the samples of higher dose (discussed in a subsequent section) which exhibited the reduced weight-gains. Apart from the dose of 1×10^{17} Al^+ ions/cm^2, samples implanted in different implant-runs to the same nominal dose behaved similarly.

Scale Morphology and Composition

The scale formed on the unimplanted alloy after 48 hours reaction was composed principally of hematite, as revealed by x-ray diffraction analysis and optical metallography. The scale itself was of non-uniform thickness (Fig. 2) and in some instances, localised areas of internal precipitation existed beneath the scale. In such cases, the internal precipitates were generally undercut by a layer at the base of the precipitates. On examination of the underface of the stripped- off scale in SEM, it was found that this layer was present across the entire undersurface. Analysis by EDAX showed aluminum to be the principal alloying element in the layer; in counts/s, Al:Fe ≈ 10:1 using a 15 kV electron beam. Thus, we can reasonably infer that this layer is composed of aluminum oxide and in line with observations from other work on a similar system for reaction at 1173 K (3), we further assume that the aluminum oxide phase is α-Al_2O_3. Figure 3 shows lateral discontinuities in the α-Al_2O_3 layer where apparently coalescence of the α-Al_2O_3 precipitates has not yet fully occurred.

The mechanically polished samples implanted to nominal doses of 5×10^{16} Al^+ ions/cm^2 and 1×10^{17} Al^+ ions/cm^2 bore scales similar to the untreated alloy following their ~50 hour oxidation and were not subjected to further analysis. As expected from the gravimetic kinetics, samples of higher aluminum doses developed oxide coverages which were significantly different in morphology and structure. A semi-transparent film formed over a large fraction of the total surface with the remainder of the surface being covered by the nodules of α- Fe_2O_3. The effect of high-dose implantation of Al on the oxidation behaviour is illustrated in Fig. 4, where the oxidized surface of a sample which was partially masked during implantation to 2×1^{17} Al^+ ions/cm^2 is shown. From performing runs to different oxidation times, it became obvious that the incidence of nodule formations was not a function of exposure time (Fig. 5), with the percentage surface coverage by the nodules fluctuating around ~50%. A comparison of the optical micrographs of Fig. 6 and Fig. 2 shows that the oxide structure across the nodule is similar essentially to that for the scale formed on the unimplanted Fe- 6 at% Al material. It may be noted from Fig. 6 that the oxide nodules have

developed not only growth outward from the alloy surface but also by extensive inward growth.

Microscopic observations of the oxide film revealed it to be convoluted and these convolutions became more pronounced with increasing reaction time. Sectioning of the sample caused the oxide film to pop off in the region of the cut, thus enabling the underlying alloy surface to be observed. The undulating appearance of the oxide film was mirrored in the appearance of the alloy surface (Fig. 7). In addition, smooth furrows were also present in the alloy surface. Because of the close correlation between size and between distribution, it was clear that the furrows had developed beneath the large ridges in the oxide film. Electron diffraction of a stripped-off film formed after a 1 hour exposure, showed the presence of $Fe_2O_3.Al_2O_3$, α-Fe_2O_3 and α-Al_2O_3. As illustrated in the composite diffraction pattern in Fig. 8, the hexagonal phases of α-Fe_2O_3 and α-Al_2O_3 exhibited texture whereas $Fe_2O_3.Al_2O_3$ was randomly oriented.

For the electropolished samples implanted to doses of 1×10^{17} Al^+ ions/cm^2 or 2×10^{17} Al^+ ions/cm^2, oxidation also led to formation of a thin oxide film containing a dispersion of nodules. Here, however, the nodules were much fewer in number and of greater individual size in comparison to those formed on the mechanically polished surfaces (Fig. 9). Surface coverage by the oxide nodules was found to vary between 10 to 40%, irrespective of exposure time. The development of film ridges and the associated loss in contact with the underlying alloy surface were again prominent features in the growth of the oxide film (Fig. 10). It was further observed that the extent of ridging in the film could vary with the orientation of the alloy substrate (Fig. 11).

To allow assessment of the full effect of Al implantation on the oxidation of Fe-6 at% Al, long-term oxidation experiments were run on samples of Fe-12 at% Al and Fe-16 at% Al alloys. The appearances of the resulting oxidized surfaces are shown in Fig. 12. Close resemblence to the oxide morphology formed on the high- dose implanted surfaces of Fe-6 at% Al is evident for the Fe-12 at% Al specimen, with the presence of nodules being particularly

noteworthy. By contrast, an oxide film completely free of nodules had formed on the surface of the Fe-16 at% Al specimen.

DISCUSSION

In the following discussion, we consider first the oxidation characteristics of the unimplanted Fe-6 at% Al and then proceed to discuss the effect of Al- implantation on these characteristics.

Following conventional arguments, exposure of the untreated Fe-6 at% Al alloy to the hot oxygen gas results initially in the rapid development of an external α-Fe_2O_3 layer. The growth rate of this layer is relatively high, accounting for the major fraction of the initially large gain in weight which, in turn, amounts to over 90% of the total weight-gain after ~45 hours reaction. Evidently, a bulk concentration of 6 at% Al is much too low to allow aluminum to compete successfully with iron in forming the surface oxide layer. Oxidation of aluminum to α-Al_2O_3 is related to the scale/alloy interface and in the alloy as precipitates.

With increasing precipitation of α-Al_2O_3, physical blocking of iron diffusing to the external α-Fe_2O_3 becomes important and a continuous decrease in the reaction rate results. Growth of the iron oxide layer continues until lateral coalescence of the α-Al_2O_3 particles into a continuous layer stops virtually further outward diffusion of iron from the alloy. This lateral coalescence of the α-Al_2O_3 layer does not occur uniformly across the alloy surface and this is manifest in the observed variation in the thickness of the outer α-Fe_2O_3 layer.

Surface-enrichment of aluminum by ion implantation bears little effect on oxidation until a critical Al concentration, corresponding to an implanted dose of 1×10^{17} Al^+ ions/cm^2, is reached. For samples implanted to this dose or above, oxidation of iron is greatly suppressed, with a transition from the relatively thick α-Fe_2O_3/α-Al_2O_3 scale morphology to a mixed α-Fe_2O_3/(Fe,Al) spinel/α- Al_2O_3 film containing a dispersion of nodules being observed (Fig. 13). It is believed that the apparent inconsistency in the oxidation behaviour by the samples implanted to 1×10^{17} Al^+ ions/cm^2 is due to the aluminum enrichment resulting

from this dose being borderline between giving unaltered and the altered behaviour. The observed alteration in oxide surface morphology is responsible for reductions in weight-gain of between 50% to 70% after ~50 hours reaction. It must be mentioned here that the loss in adherency of the protective film during its growth is not considered to be of concern since preliminary work in our laboratory on Al-implanted Fe-6Al-0.15Y alloys have demonstrated that decohesion of the oxide film can be prevented. Differences in surface preparation prior to high-dose implants were found to have no significant effect on the oxidation reaction.

Despite the reductions in weight-gain, the full effect of Al-implanting the alloy surface on its oxidation behaviour was nonetheless disappointing. The desired effect of achieving a protective oxide film across the entire implanted surface was only partially achieved due to the additional presence of nodules. A thorough investigation of the cause of nodule formation was outside the scope of this work. However, we did establish some facts relevant to their formation in this alloy system. First, nucleation and growth of the nodules occurred close to the outset of oxidation. This is evident from Fig. 5 and from Fig. 1, in which extremely low rates of oxidation were observed onwards from exposures of 3-5 hours. Thus, the occurence of nodules is unrelated to the extensive buckling, and any associated mode of failure, observed in the protective oxide film at its later stages of growth. Secondly and equally importantly, the formation of nodules is not a development induced by the process of ion modification of the alloy surface. The observation that nodules also form on untreated Al-rich Fe-Al alloy, certainly up to 12 at% Al but not at 16 at% Al, demonstates clearly that these features are an inherent property of the oxidation behaviour of the alloy itself. This result was particularly disconcerting since in the other work performed on the oxidation of Fe-Al alloys under similar test conditions (3), thin duplex α-Fe_2O_3/α-Al_2O_3 films devoid of nodules formed on Fe-7.4 at% Al and Fe-8.4 at% Al alloys at 1173 K. The only essential difference between the two studies was in the source of iron used to make the alloys. If this difference is responsible for the formation of nodules, then alloy impurities, either dissolved or in the form of precipitates, or gas pores within the material must play an active role in the

oxidation process. Further discussion on the cause of this oxidation feature is not possible within the framework of the experimental results obtained in this study.

In assessing the overall merit of implanting with aluminum for corrosion resistance, we note that nodule growth is also encountered in oxidation of other similar alloy systems (5, 6, 7). Failure of aluminum implantation to suppress formation of α-Fe_2O_3 nodules suggests, therefore, that this technique does not really provide a realistic alternative to alloying the metal substrate, or to coating the metal surface, in situations where corrosion protection by surface α-Al_2O_3- rich layers is desired.

CONCLUSIONS

1. Oxidation of Fe-6 at% Al in oxygen at 1173 K proceeds through an initial stage of rapid weight-gain, attributed to formation and growth of an α- Fe_2O_3 layer; an interval of decreasing reaction rate due to a build-up of Al_2O_3 precipitates in the subsurface restricting the supply of iron to the α-Fe_2O_3 layer; a final stage of slow oxide growth controlled by growth of an α-Al_2O_3 layer formed by lateral coalescence of the subsurface precipitates.

2. Ion-beam implanting of aluminum exerted an effect on oxidation only for doses of 1×10^{17} Al^+ ions/cm^2 or greater. At such doses, a mixed α- Fe_2O_3/(Fe, Al) spinel/α-Al_2O_3 film with a dispersion of α-Fe_2O_3 nodules developed. The presence of the nodules acted to limit the benefits achieved by Al-implantation with weight gains being lower by 50-70% compared to the unimplanted alloy.

3. The development of the protective film/nodule morphology on an unimplanted Fe-12 at% Al alloy demonstrated that the occurrence of nodules was inherent to oxidation of the alloy material itself; it was not an extraneous feature introduced by the ion-implantation treatment.

4. The oxidation properties of mechanically polished and electropolished samples subjected to high-dose Al implants were similar. Difference with surface preparation arose only in the relative size and population density of the nodules.

5. The undesirable formation of nodules and the failure of aluminum implantation to suppress their growth, at least initially, restricts the use of aluminum implantation as an alternative to more conventional methods for imparting corrosion resistance.

ACKNOWLEDGEMENTS

The authors gratefully acknowledge the financial support of this research by CANMET, Department of Energy, Mines and Resources of Canada, Ottawa, Ontario, Canada.

REFERENCES

1. M. Pons, M. Caillet and A. Galerie, Corros. Sci. 22, 239 (1982).

2. U. Bernabai, M. Cavallini and G. Bombara, Corros. Sci., 20, 19 (1980)

3. H.A. Ahmed and W.W. Smeltzer, J. Electrochem. Soc. 133, 212 (1986).

4. H.A. Ahmed, R.P. Underhill, W.W. Smeltzer, M.E. Brett and M.J. Graham, to be published.

5. P. Tomazewicz and G.R. Wallwork, Oxid. Met. 19, 165 (1983).

6. P. Tomazewicz and G.R. Wallwork, Oxid. Met. 20, 75 (1983).

7. P.R.S. Jackson and G.R. Wallwork, Oxid. Met. 21, 135 (1984).

Table 1: Calculated rate constants ($g^2\,m^{-4}\,s^{-1}$) for parabolic-type oxide growth on specimens of Fe-6 at% Al implanted with Al to various doses. Growth proceeds through two stages of reactivity.

Dose (Al^+ ions/cm^2)	Parabolic Rate Constants	
	Initial	Final Stage
0	$1.2(\pm 0.05) \times 10-10$	$1.9(\pm 0.6) \times 10^{-12}$
"	"	"
5×10^{16}	"	"
1×10^{17}	"	"
2×10^{17}	"	n.m.[a]
3×10^{17}	$2.8(\pm 0.05) \times 10^{-11}$	$8.5(\pm 0.7) \times 10^{-13}$

[a] not measureable, weight gain below sensitivity limit of gravimetric technique.

FIGURE CAPTIONS

Fig. 1 Gravimetric kinetics for oxidation of 1173 K of an Fe-6 at% Al alloy implanted to various does of Al: (a) linear coordinates, (b) parabolic-growth coordinates.

Fig. 2 Optical micrographs of duplex α-Fe_2O_3/α-Al_2O_3 scale grown on Fe-6 at% Al in cross-section illustrating non-uniform thickness of scale and the occurrence of subsurface precipitation of α-Al_2O_3 (oxidation time = 48 hours).

Fig. 3 SEM micrograph of the underside of the α-Fe_2O_3/α-Al_2O_3 scale formed on Fe-6 at% Al after 48 hours reaction. The presence of the α- Al_2O_3 with apparently lateral discontinuities is revealed.

Fig. 4 SEM micrograph of the oxidized surface on Fe-6 at% Al sample partially masked during the prior implantation to 2×10^{17} Al^+ ions/cm^2. The effect of the implantation treatment on oxidation is evident. (Oxidation time = 51 hours).

Fig. 5 SEM micrographs of oxidized surfaces of Fe-6 at% Al samples implanted to doses of 2×10^{17} Al^+ ions/cm^2 after reaction for different times: (a) 10 hours, (b) 50 hours.

Fig. 6 Optical micrographs showing nodules in cross-section for an Fe-6 at% Al sample implanted to 2×10^{17} Al^+ ions/cm^2 and oxidized for 50 hours.

Fig. 7 SEM micrographs of oxidized surface of Fe-6 at% Al speciment implanted to 2×10^{17} Al^+ ions/cm^2: alloy surface revealed by spallation of oxide contains smooth furrows (Oxidation time = 50 hours).

Fig. 8 Electron diffraction pattern of oxide film developed following oxidation for 1 hour of an Fe-6 at% Al sample implanted to 2×10^{17} Al^+ ions/cm^2. Diffraction patterns shows the presence of $Fe_2O_3.Al_2O_3$ (random orientation), α-Fe_2O_3 (textured) and α-Al_2O_3 (textured).

Fig. 9 SEM micrograph of electropolished (Fe-6 at% Al) surface implanted to 2×10^{17} Al^+ ions/cm^2 and oxidized for 22 hours.

Fig. 10 SEM micrograph showing uncovered alloy surface and oxide film for an electropolished Fe-6 at% Al specimen implanted to 2×10^{17} Al^+ ions/cm^2. Facetting when the smooth furrows on the alloy surface is apparent. (Oxidation time = 22 hours).

Fig. 11 SEM micrograph illustrating effect of alloy substrate orientation on ridging within the oxide film grown on an electropolished Fe-6 at% Al sample implanted to 1×10^{17} Al^+ ions/cm^2 (Oxidation time = 16 1/2 hours).

Fig. 12 SEM micrographs of oxidized surfaces of (a) an Fe-12 at% Al specimen oxidized for 190 hours and (b) an Fe-16 a/o Al specimen oxidized for ½ hours.

Fig. 13 Schematic illustration showing effect of high dose aluminum implants on the long-term oxidation behaviour of Fe-6 at% Al at 1173 K.

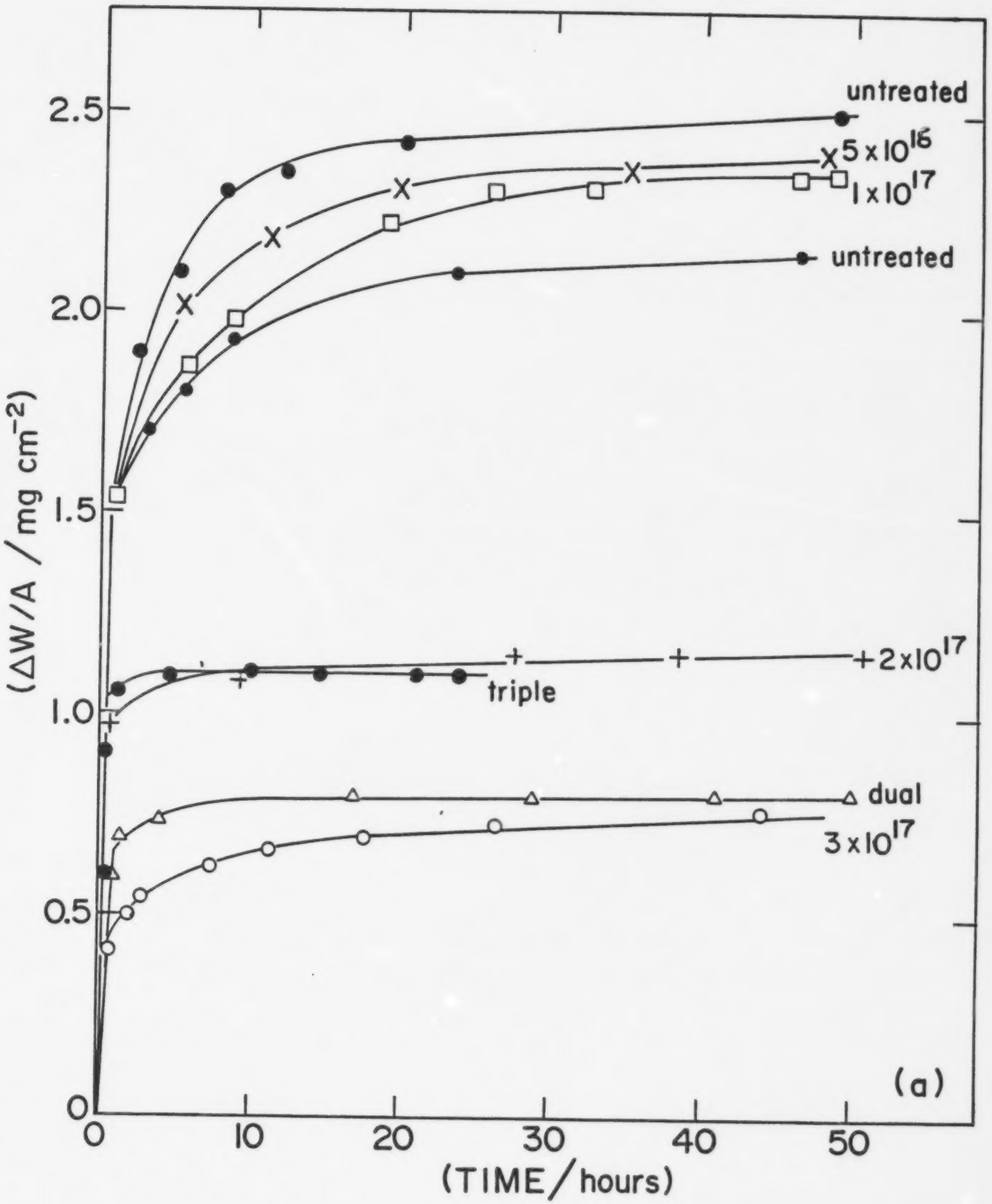
untreated
5 x 10^16
1 x 10^17
untreated
+2x10^17
triple
dual
3 x 10^17
(a)
(ΔW/A / mg cm^-2)
(TIME / hours)
0
0.5
1.0
1.5
2.0
2.5
0
10
20
30
40
50

Figure 1(a)

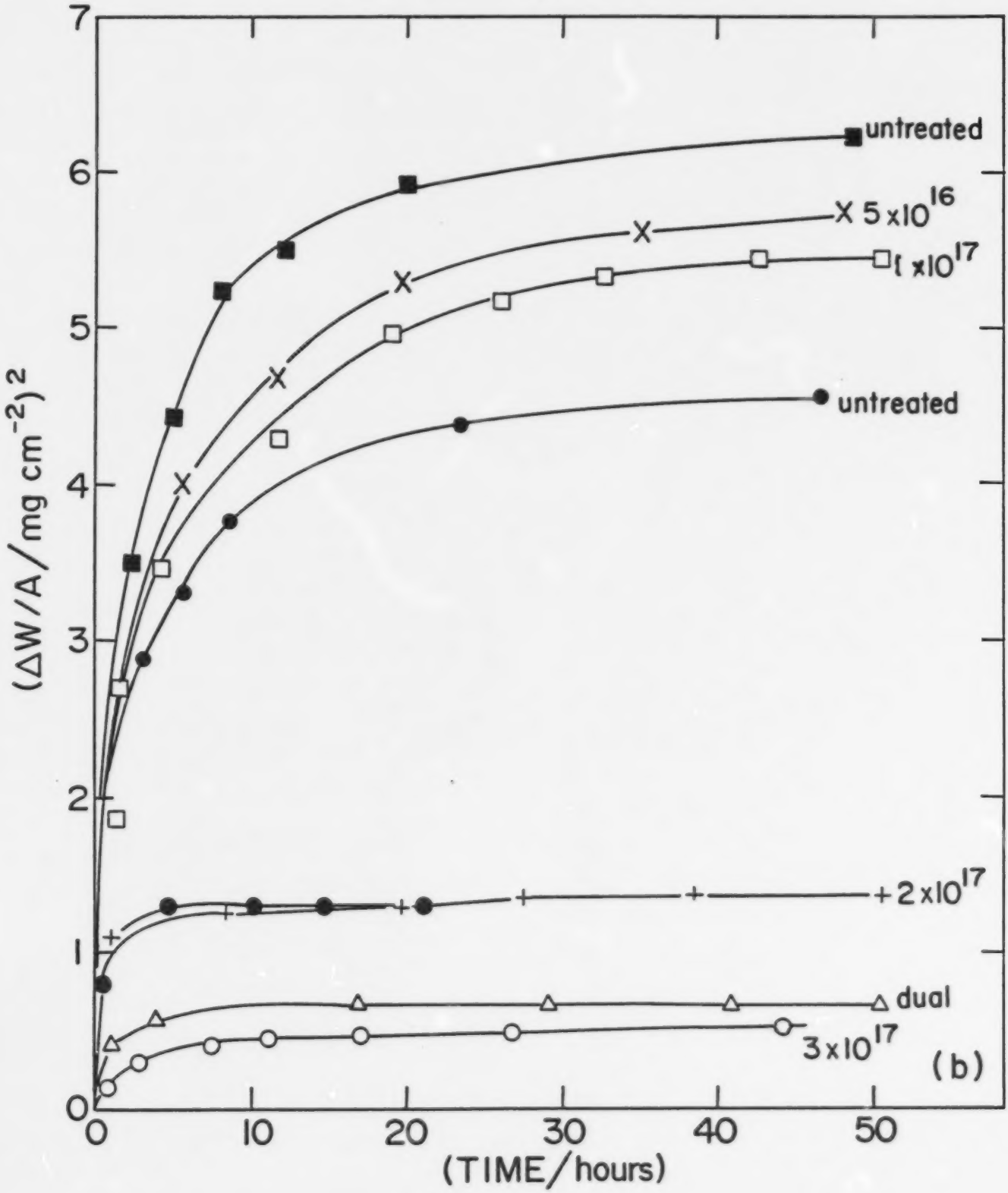
7
6
5
4
3
2
1
0
0
10
20
30
40
50
(ΔW/A/mg cm⁻²)²
(TIME/hours)
untreated
X 5x10¹⁶
t x10¹⁷
untreated
+2x10¹⁷
dual
3x10¹⁷
(b)

Figure 1(b)

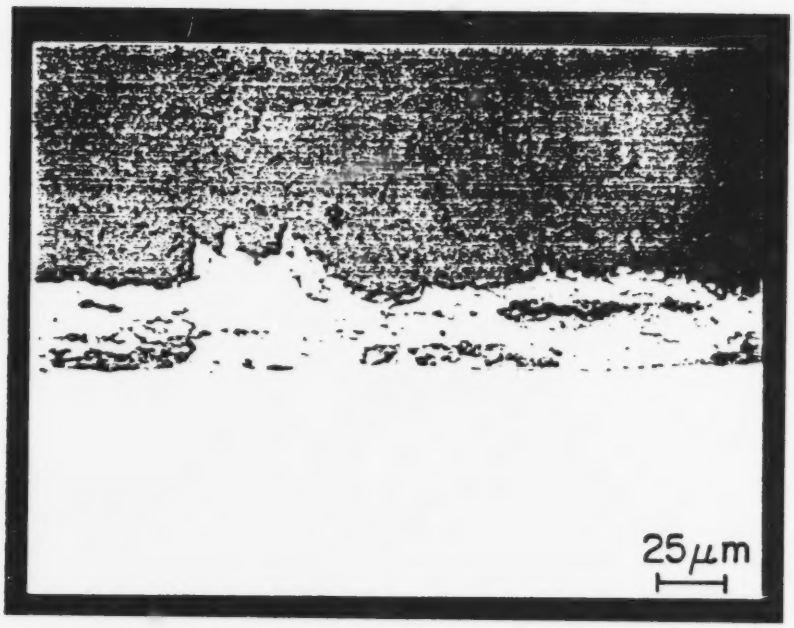

(a)

(b)

Figure 2

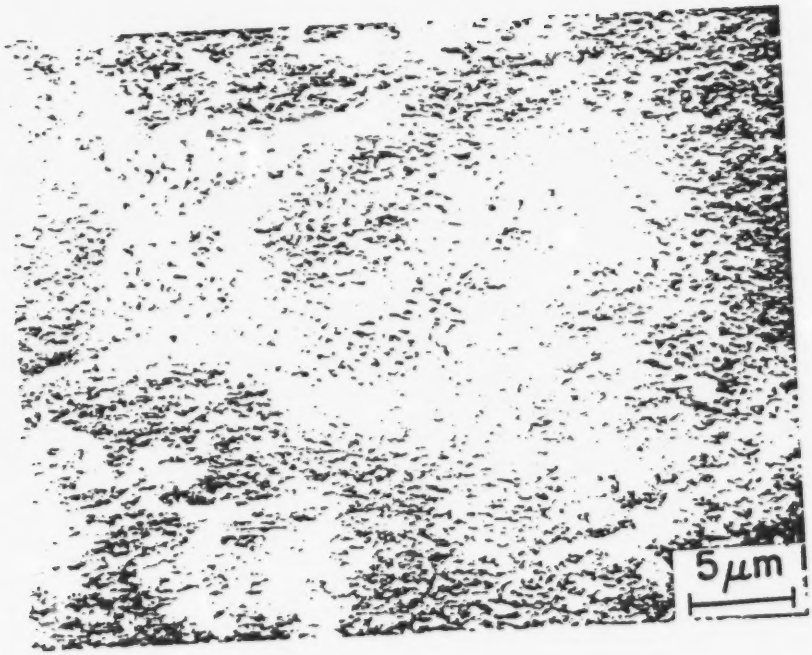

Figure 3

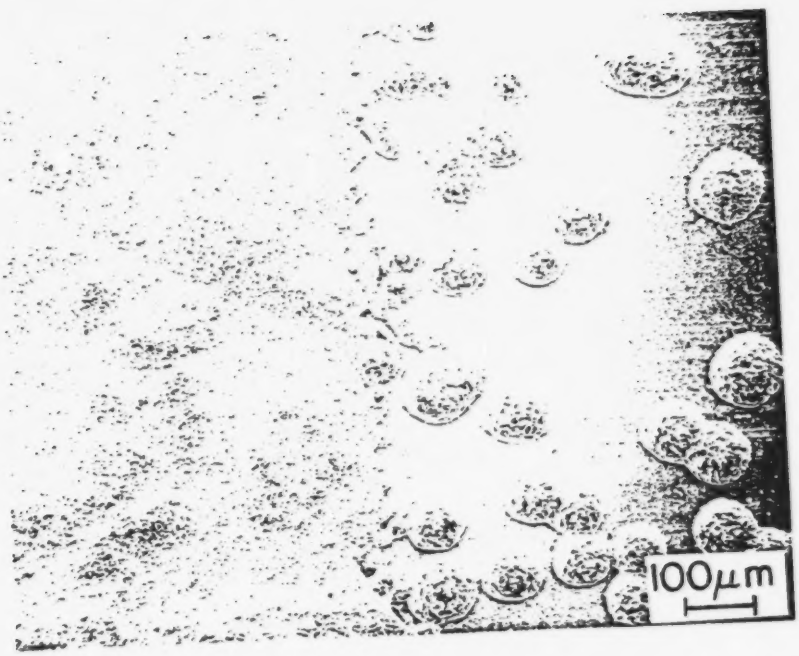

Figure 4

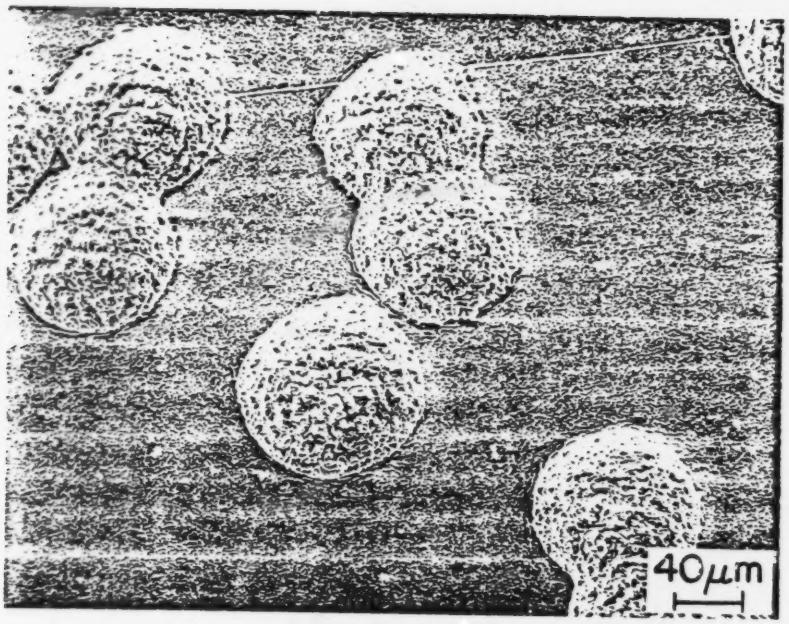

(a)

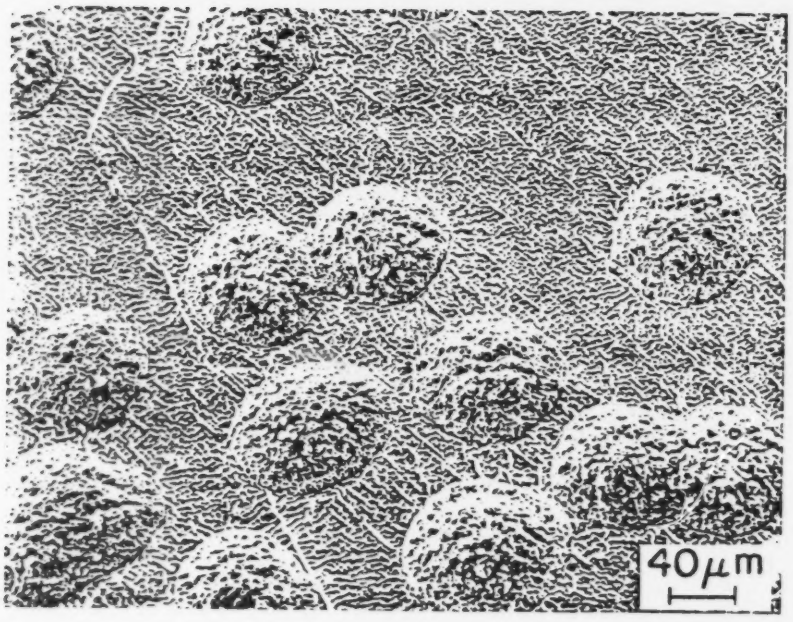

(b)

Figure 5

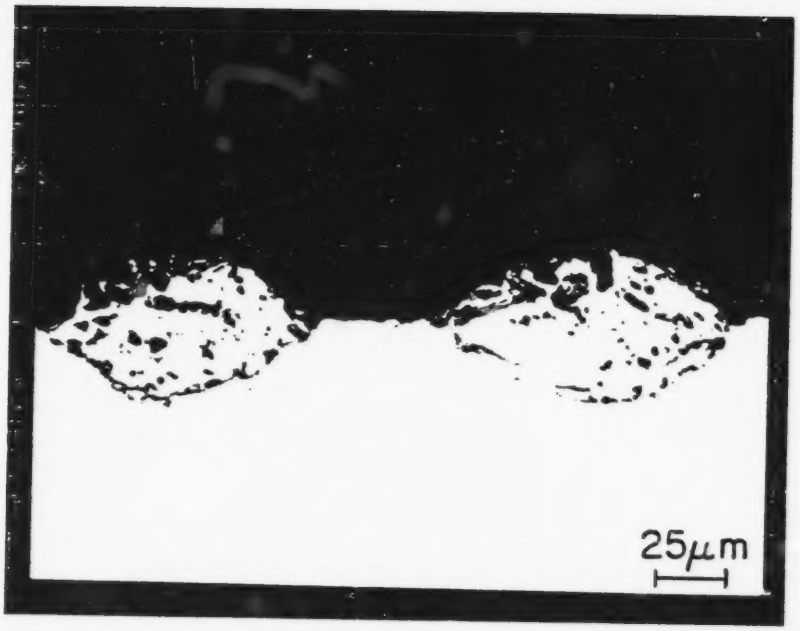

Figure 6

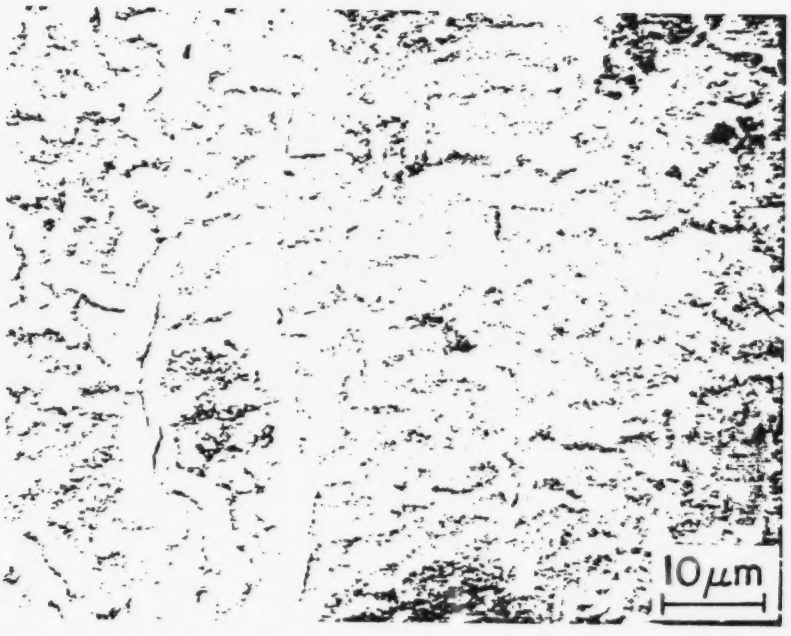

Figure 7

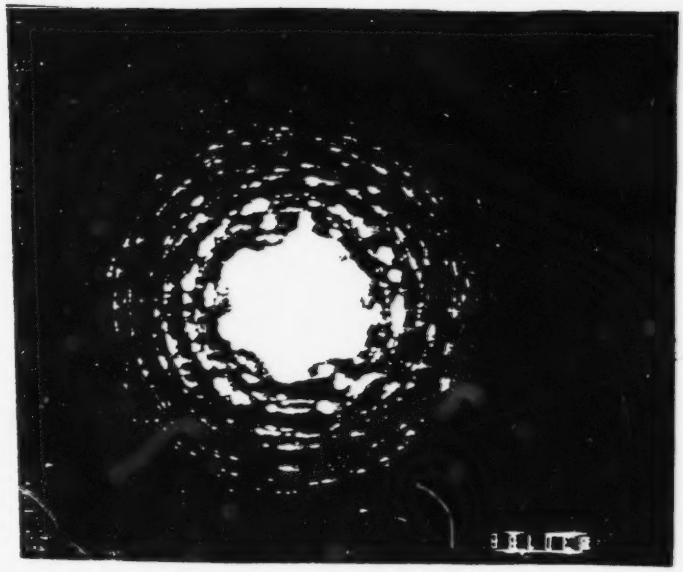

Figure 8

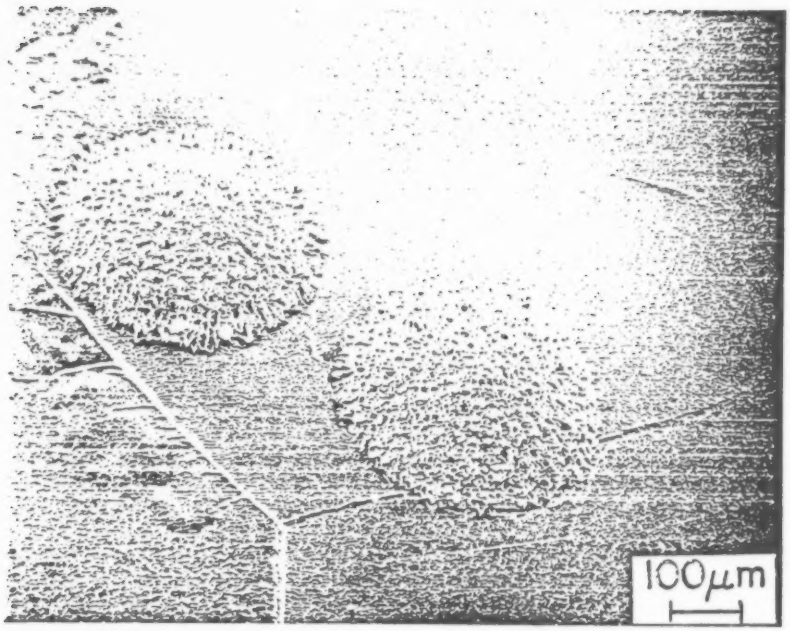

Figure 9

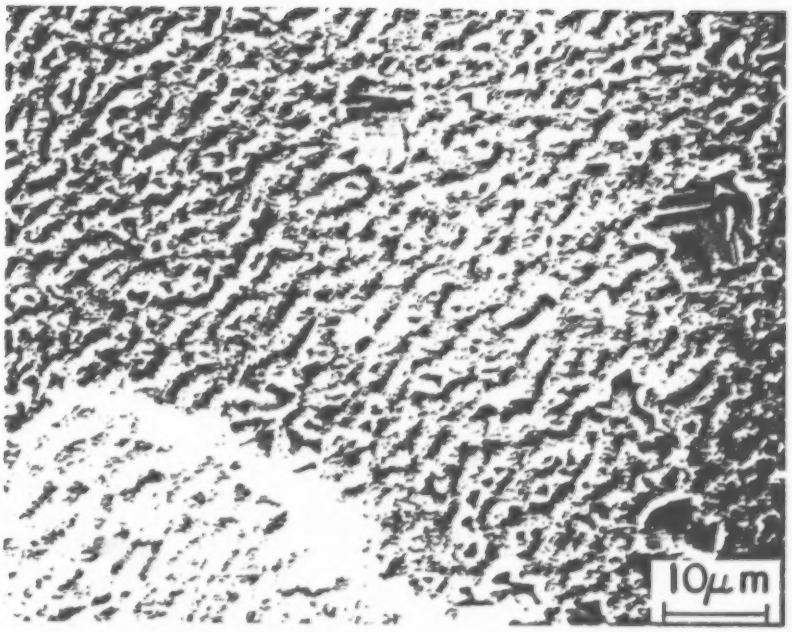

Figure 10

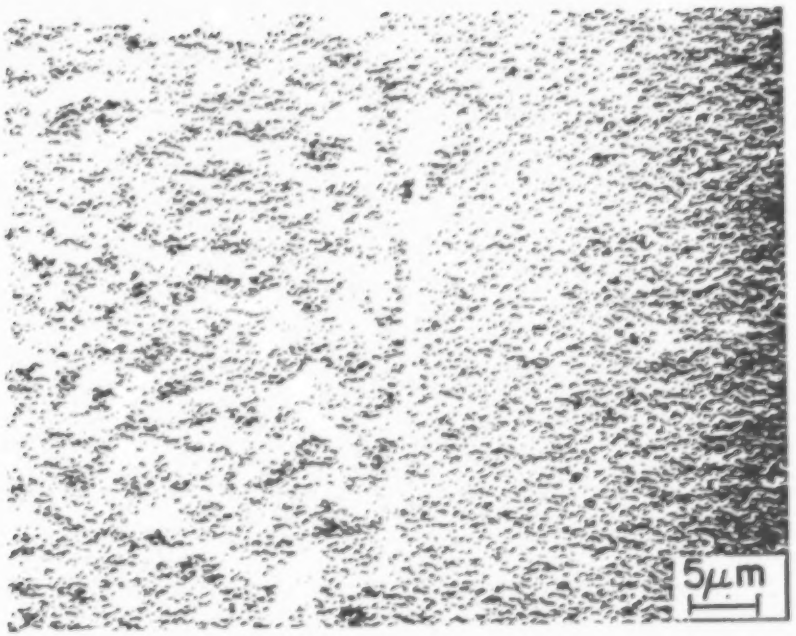

Figure 11

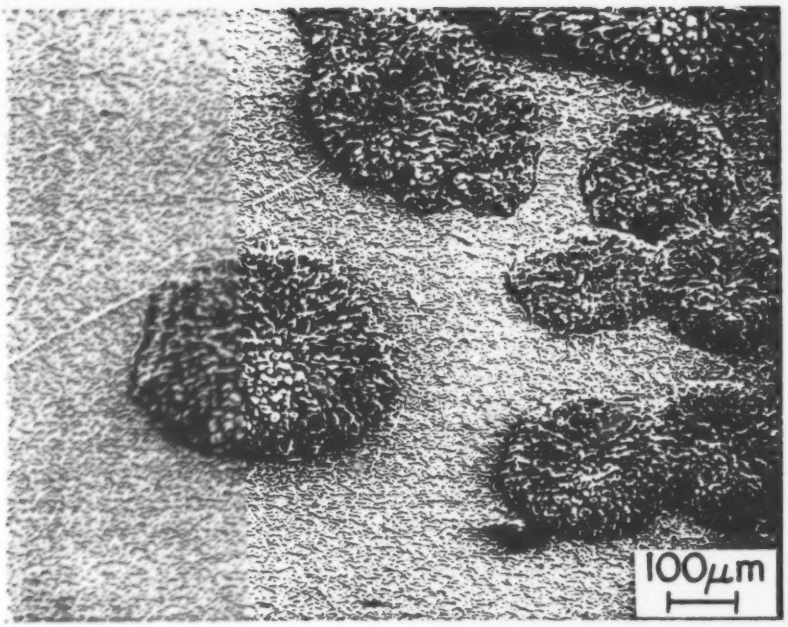

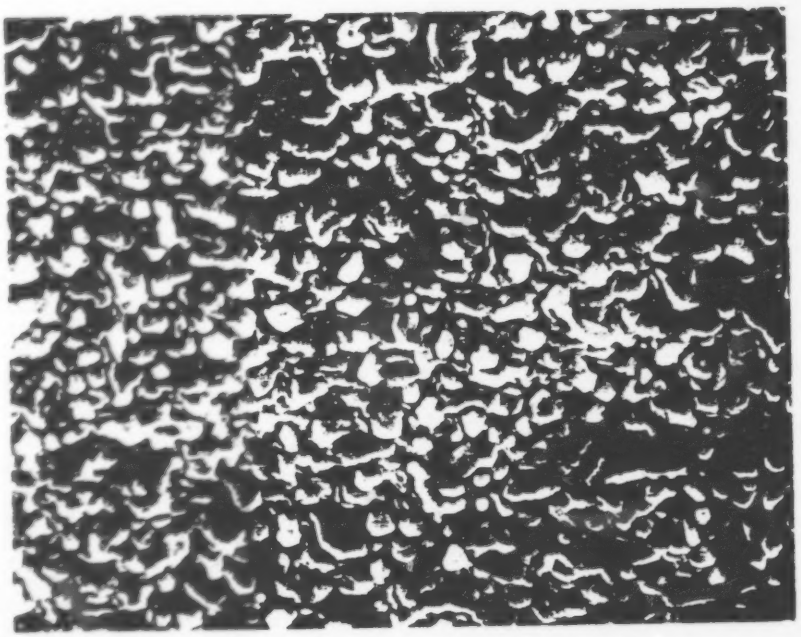

Figure 12

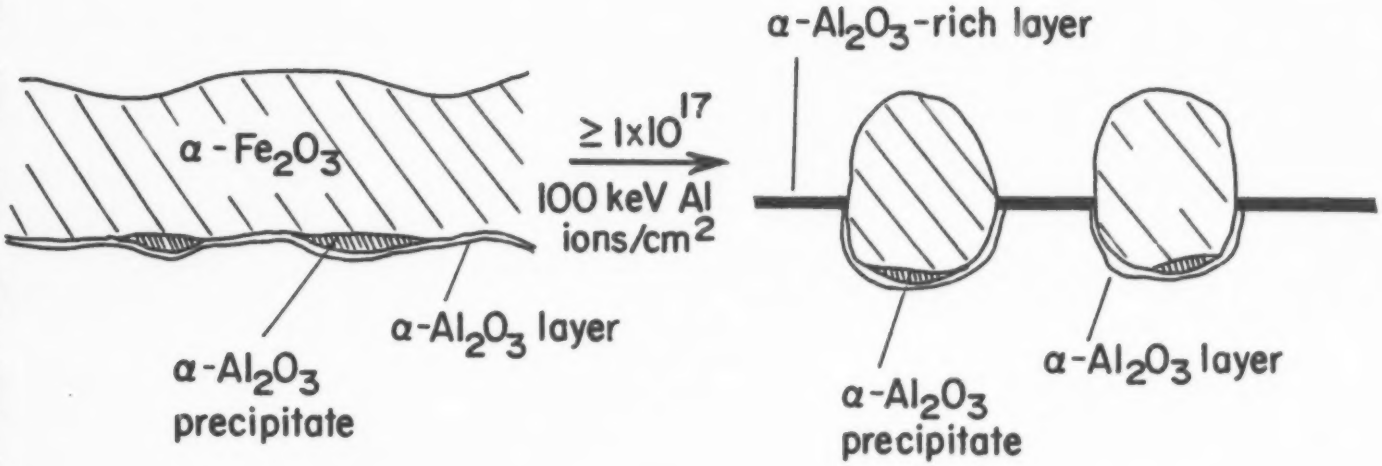
α-Al2O3-rich layer
α-Fe2O3
≥ 1x10^17
100 keV Al
ions/cm^2
α-Al2O3 layer
α-Al2O3
precipitate
α-Al2O3 layer
α-Al2O3
precipitate

Figure 13

APPENDIX 1

OXIDATION OF Fe-Al ALLOYS IN OXYGEN AT 1273 AND 1373K

Abstract

A summary is presented of investigations carried out on the oxidation properties of several Fe-Al alloys containing from 5 to 15 a% Al in 1 atm of oxygen at 1273 and 1373K. The oxidation kinetics can be represented by two parabolic reaction rate constants for early and long exposures, the rate constant at long times being at least 10^3 smaller than at early exposures. The scale morphologies were similar to those at 973K, oxidation resistance increasing as the morphologies changed from precipitates/ magnetite/hematite; alumina/magnetite/hematite; alumina/hematite/nodules; alumina/hematite nodules to alumina films with increasing alloy aluminum content. Alloys containing 12 to 15 a% Al only formed the most highly protective alumina films, the alloy composition apparently being more significant than temperature in the range 1173-1373K.

Results and Discussion

The results of the oxidation kinetics at 1273 and 1373K for the alloys containing from 2.5 wt% (5.0 a%) to 8.0 wt% (15.3 a%) are presented by plots corresponding to parabolic co-ordinates in Fig. 1 and 2. There is an initial rapid stage of parabolic kinetics followed by a final period of much slower parabolic kinetics in most cases measured especially as the Al alloy content is increased. These results are summarized in Table 1.

Table 1. Parabolic oxidation rate constants at early and final stages of oxidation at 1273 and 1373K.

	Temperature=1273K		Temperature=1373K
Al wt% (a%)	k_p^1 ($kg^2m^{-4}s^{-1}$)	k_p^{2+} ($kg^2m^{-4}s^{-1}$)	$k_p^{\odot}$ ($kg^2m^{-4}s^{-1}$)
2.5 (5.0)	$(4.6\text{-}11.0)\times10^{-8}$	1.74×10^{-11}	1.0×10^{-9}
2.77(5.5)	-	-	$(1.46\text{-}1.66)\times10^{-9}$
3.0(6.0)	-	-	1.125×10^{-9}
3.5 (7.0)	9.76×10^{-8}	2.7×10^{-11}	4.36×10^{-11}
4.1 (8.2)	9.7×10^{-8}	1.1×10^{-11}	4.59×10^{-11}
actual (4.123)			
6.0 (11.7)	2.25×10^{-8}	1.1×10^{-11}	n.m.
actual (6.14)			
8.0 (15.3)	n.m.*		n.m.

* n.m. = not measureable

\+ transition from growth according to k_p^1 to that governed by k_p^2 occurred at: 5 1/2 hr. for Fe-2Al

5 hr. for Fe-3.5Al

3 hr. for Fe-4.5Al

1 1/2 hr. for Fe-6Al

$\odot$ essentially mono-parabolic growth kinetics at 1373K.

The scale morphologies, which correspond to those at 1173K and previoulsy described in Sections I and II of this report, are shown as a function of alloy Al content (wt%) in Fig. 3. It is seen that the fully protective Al_2O_3 film is only obtained with alloys containing greater than 7 wt% Al (14 a%). These results should be compared to those given in Fig. 79 (section I, p. 111). It can be noted from this comparison that Al content is more significant than temperature in determining scale morphologies and structures over the temperature range 1173 to 1373K.

Despite these macroscopic morphological features, the parabolic oxidation rate constants at early exposure periods are approximately two orders of magnitude lower at 1373 than at 1273K as shown in Fig. 4. This unusual behavior is probably associated with the grain size of oxide in the scales. Short-circuit diffusion of reactants across the scales occur. Thus, the parabolic rate constant is of a form

$$x^2 = \left[2\Omega \int_{a_o^{(i)}}^{a_o^{(o)}} D_{eff} \, d \ln a_o \right] t$$

where a_o represents an activity at interfacial layer boundaries and D_{eff} is the effective diffusion coefficient. This diffusivity, in turn, can be expressed as

$$D_{eff} = D_L(1 - f) + D_B f$$

where D_L amd D_B are lattice and boundary diffusivities, respectively, and f is the fraction of diffusion sites at oxide grain boundaries. At the higher temperature of 1373 K, the oxide grain size is much larger by the influence of increased oxide grain growth at this temperature. Hence, the

measured parabolic rate constant is much smaller due to a much smaller degree of reactant grain boundary diffusion.

Figure Illustrations (Appendix)

Figure 1. Oxidation kinetics at 1273 K and 1 atm oxygen represented in parabolic coordinates.

Figure 2. Oxidation kinetics at 1373 K and 1 atm oxygen represented in parabolic coordinates.

Figure 3. Scale morphologies as a function of Aℓ alloy content in wt % at 1273 and 1373 K.

Figure 4. Parabolic oxidation rate constants as a function of Aℓ alloy content in wt % at 1273 and 1373 K.

WWS.1/JH

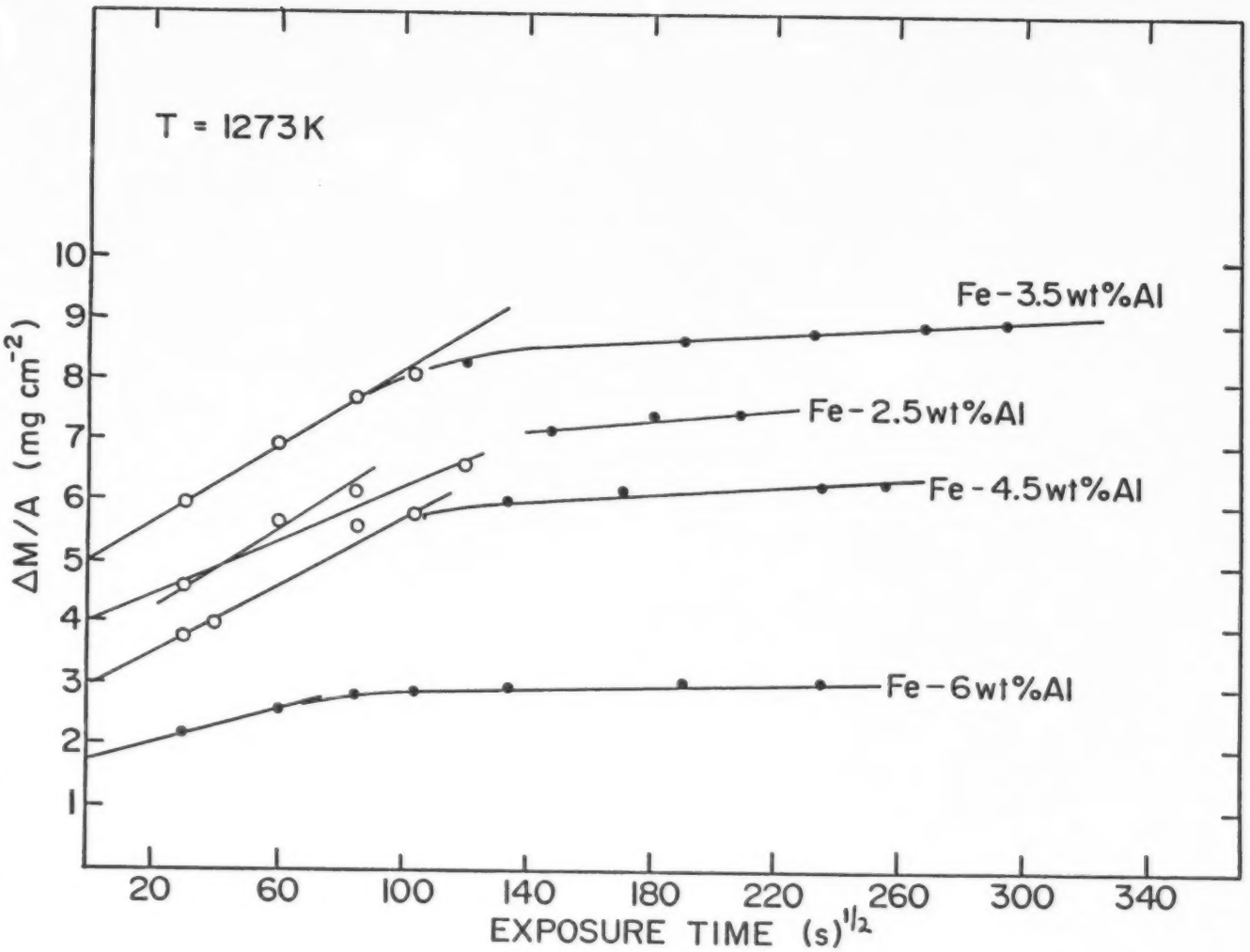

Figure 1 (Appendix)

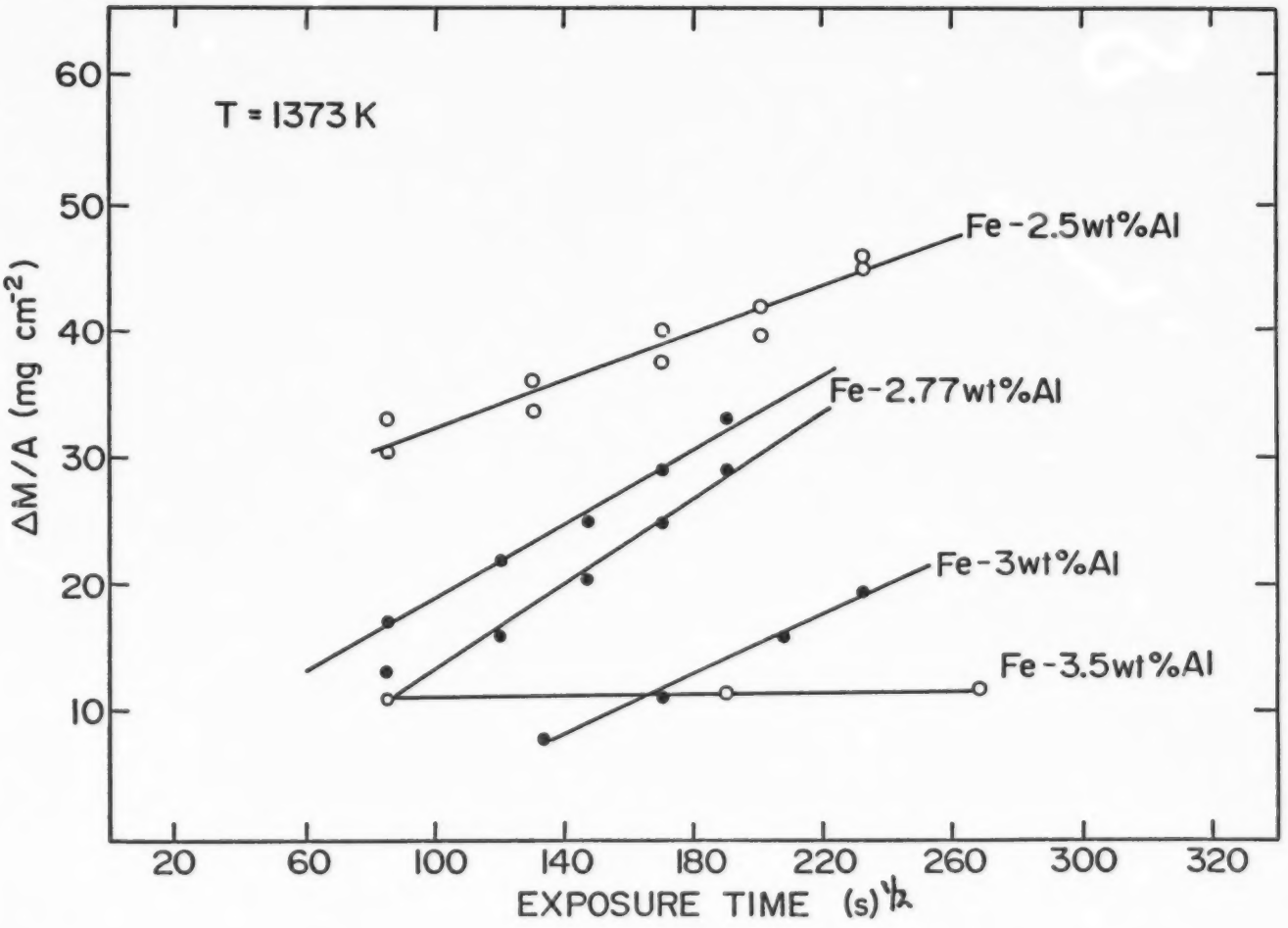

Figure 2 (Appendix)

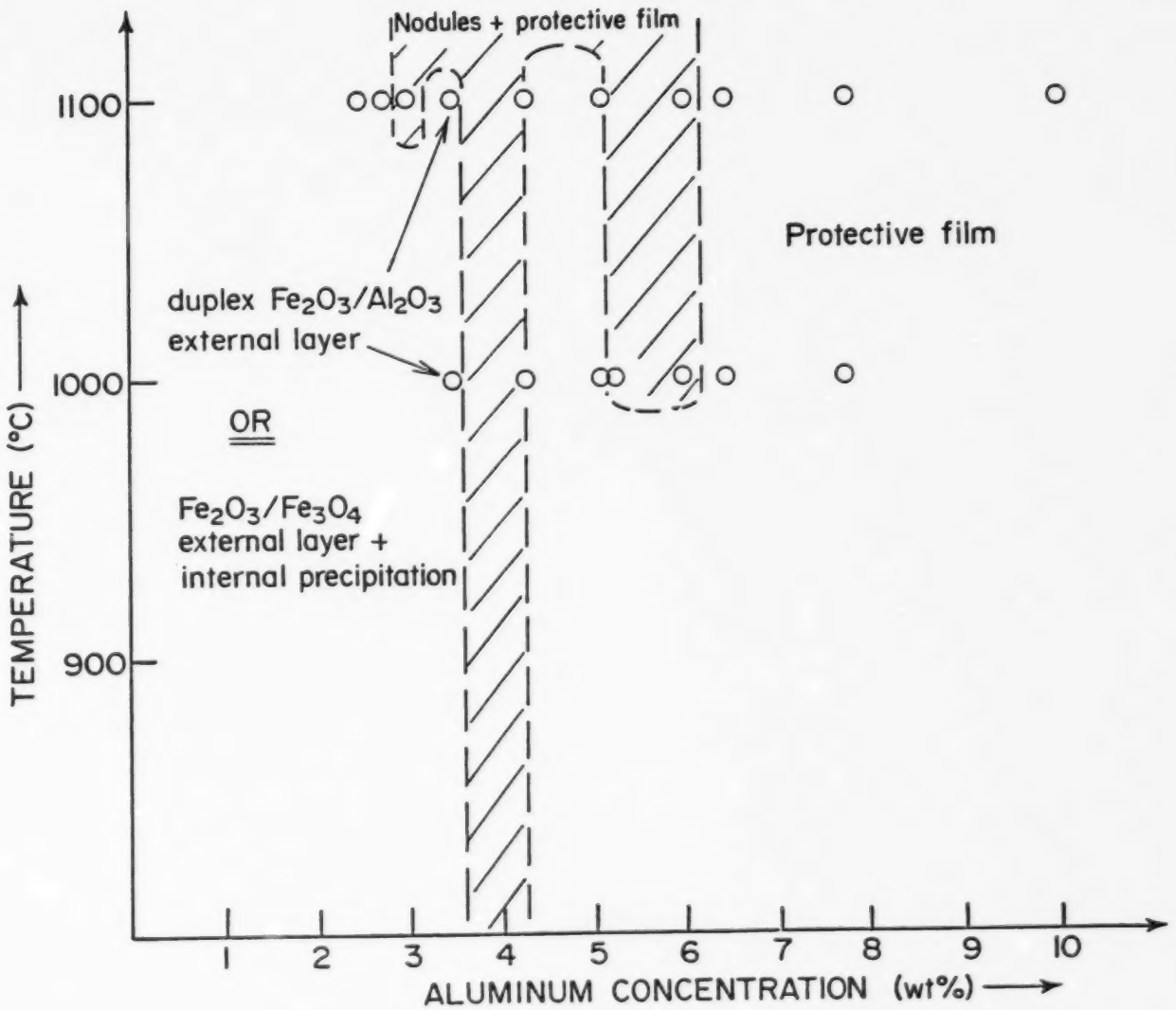

Appendix 3 (Appendix)

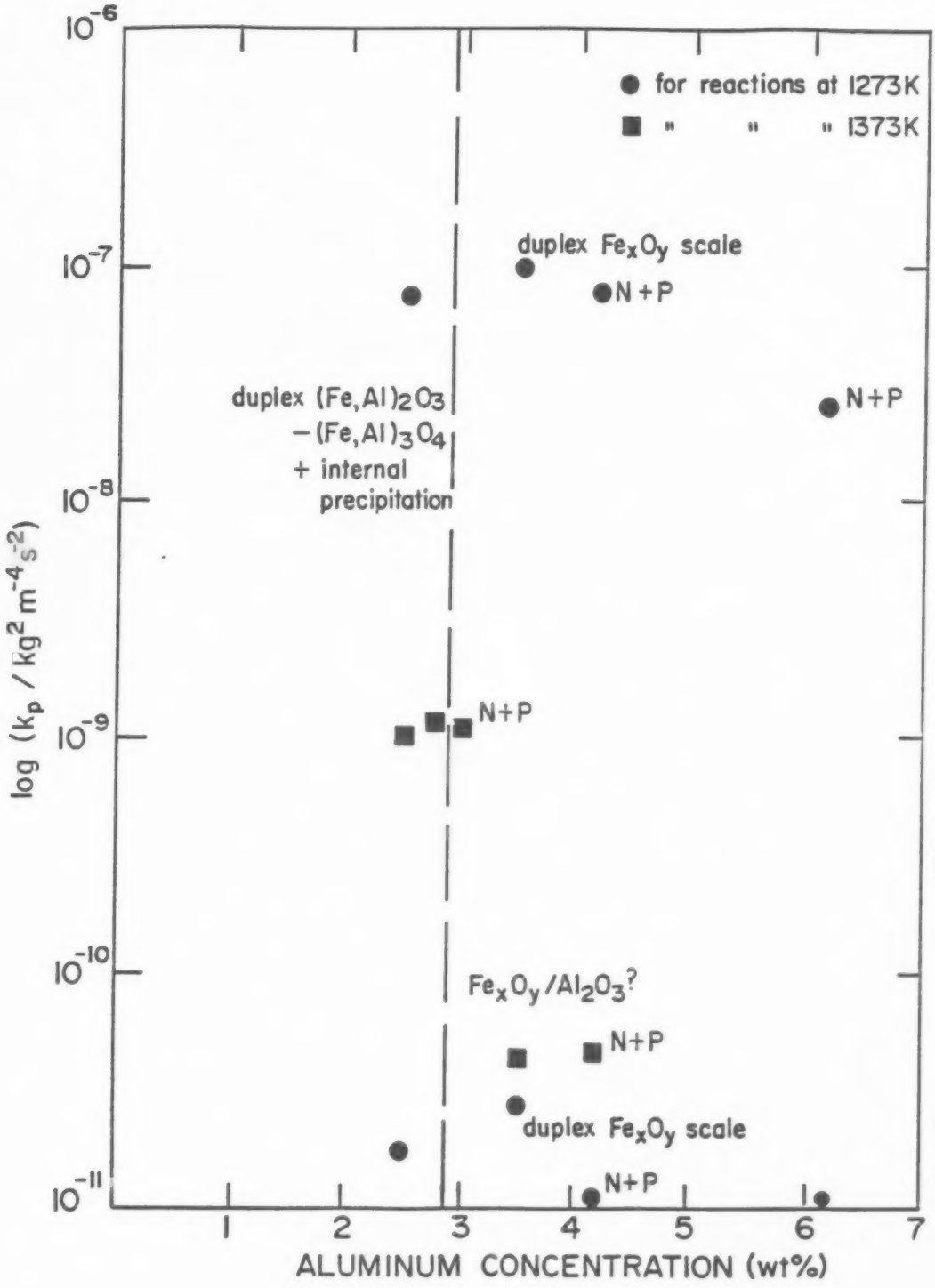

Figure 4 (Appendix)